

# Measurement of the Top Quark Mass by Application of the Dalitz-Goldstein Method to Dilepton Events

A dissertation

submitted by

Kristo Michael Karr

in partial fulfillment of the requirements

for the degree of

Doctor of Philosophy

in

Physics

TUFTS UNIVERSITY

May 1999

Advisor: Professor Krzysztof Sliwa

© 1999

Kristo Michael Karr

ALL RIGHTS RESERVED

This dissertation is dedicated to the memory of my colleagues and friends Tim Bernard and David Albert. Their courage, intelligence and sense of humor in the face of overwhelming odds was truly moving.

# Measurement of the Top Quark Mass by Application of the Dalitz-Goldstein Method to Dilepton Events

by Kristo Michael Karr

Advisor: Professor Krzysztof Sliwa

## Abstract

This dissertation presents a measurement of the top quark mass by application of the Dalitz-Goldstein method to dilepton  $t\bar{t}$  events. The events were produced by the Tevatron Collider at Fermi National Accelerator Laboratory (Fermilab) via  $p\bar{p}$  collisions with  $\sqrt{s} = 1.8$  TeV. The dilepton event sample was extracted from 109 pb<sup>-1</sup> of data collected by the Collider Detector at Fermilab (CDF) from August 1992 to July 1995. The sample contains a total of 9 candidate events, 2.4 of which are expected from background. Included in the dilepton final state are two neutrinos, which elude detection. This analysis constrains the problem by assuming an initial value for the top quark mass and solving for the neutrino momenta via a geometrical construction developed by D.H. Dalitz and G. Goldstein. The top quark mass is sampled over a wide range of possible values and the most likely mass consistent with the data is chosen via a likelihood function. An important distinguishing feature of this mass fitting technique is its lack of dependence on missing transverse energy, a kinematic variable that is poorly measured by experiment. This analysis determines the top quark mass to be  $M_{top} = 157.1 \pm 10.9(stat.) \pm_{3.7}^{4.3}(syst.)$  GeV/c<sup>2</sup>.

# Acknowledgements

First and foremost I would like to thank my advisor and friend Professor Krzysztof Sliwa for suggesting this challenging but rewarding research project and for sharing his wealth of knowledge and experience to make the completion of this analysis possible. His genuine enthusiasm and dedication to the field of experimental particle physics have been continuous sources of inspiration for me. Secondly, I wish to thank Professor Tony Mann for enabling me to obtain valuable hardware experience through employment on projects related to the Soudan Underground Laboratory and the ATLAS detector at CERN. Thirdly, I would like to thank Professor Jack Schneps for officially approving my research assistantship at Tufts. I also wish to thank the rest of the Tufts high energy physics teaching staff, including Professors Austin Napier, Gary Goldstein, Rick Milburn, Bill Oliver and Thomas Kafka, for furthering my knowledge of the field through courses, lectures and friendly conversation. Outside of high energy physics I value education received from Professors Larry Ford, Tanmay Vachaspati, David Weaver and the late Professor Howard Sample. I wish to thank Larry McMaster and the rest of the Tufts high energy physics machine shop staff for teaching me something practical and trusting an absent-minded professor with some of their machines. Special thanks to secretaries Waltye Greene, Jackie DiMichele and Rita Fleischer for gracefully and efficiently smoothing out the various administrative problems that inevitably befall an off-campus graduate student.

It has been a pleasure becoming acquainted with all my fellow graduate students in the Tufts high energy physics department. I wish to thank my colleague Henry Tom for being an invaluable partner in the building of prototype drift tubes for the ATLAS project and a good friend ever since. I would like to thank my colleague Dan Wall for always sharing his knowledge about physics related matters, including some valuable tips about LaTeX that were needed to construct this document. I also wish to thank my office partner in the CDF trailers, David Dagenhart, for several worthwhile exchanges of ideas and for answering any questions I have had about UNIX, C++ and Objectivity. Thanks are also due to William Leeson for introducing me to PAW and other essential physics tools when I was still a young pup in the world of high energy physics. I would like to acknowledge all the Tufts physics graduate students outside of high energy physics that I have had the pleasure of meeting, including my

friend Rohit Pappu who was the first to encourage me to migrate from VMS and Fortran to UNIX and C++.

At Fermilab I wish to thank all the members of the CDF Top Group for their inciteful questions and helpful suggestions during the blessing process of this analysis. I would especially like to thank Top Group co-convener Luc Demortier for constructive and unbiased criticism of this analysis that was essential for getting it blessed. I also wish to thank Mark Kruse for both directly and indirectly providing information about event selection efficiencies and background events necessary for the completion of chapter 4 of this document. Thanks are also due to Rob Roser for inviting me to present blessed top mass results at the April 1998 APS meeting. I wish to give special thanks to my colleague Simona Rolli for encouraging me to participate in the Run II database management system proposal and for always answering any questions I have had about Objectivity and other physics related matters. To all of the people at CDF that I have had the pleasure of meeting in one capacity or another I value our acquaintanceship and only regret not having taken the time to get to know some of you better.

On a personal note, I would like to thank Kelly and Claudia for continuing to be my best friends and Hana for continuing to be my favorite godchild. Special thanks to other related family and friends, especially Haruko and Don for always treating me as one of their own. I wish to thank my sister Taina for her continued love and support despite our spatial separation of thousands of miles. Last but certainly not least I would like to express deep gratitude to my parents, without whose love, support and encouragement this dissertation would not be possible.

# Table of Contents

<b>Abstract</b>	<b>iv</b>
<b>Acknowledgements</b>	<b>v</b>
<b>List of Tables</b>	<b>x</b>
<b>List of Figures</b>	<b>xiv</b>
<b>1 Introduction</b>	<b>2</b>
1.1 Constituents of Matter and Interactions . . . . .	3
1.1.1 Leptons and Quarks . . . . .	4
1.1.2 Gauge Bosons . . . . .	6
1.1.3 The Standard Model . . . . .	9
1.2 The Top Quark . . . . .	16
1.2.1 Production and Decay . . . . .	16
1.2.2 History of Discovery . . . . .	19
<b>2 Experimental Apparatus</b>	<b>24</b>
2.1 Particle Acceleration . . . . .	24
2.2 CDF Detector . . . . .	26
2.2.1 Tracking Chambers . . . . .	26
2.2.2 Calorimeters . . . . .	29
2.2.3 Muon Detectors . . . . .	31
2.2.4 Luminosity Measurement . . . . .	33
2.3 CDF Triggers . . . . .	34
<b>3 Jet Energy Corrections</b>	<b>37</b>
3.1 Jet Reconstruction Algorithm . . . . .	37
3.2 Standard Jet Energy Corrections . . . . .	37
3.3 Jet Energy Corrections for Dilepton Events . . . . .	40
<b>4 Dilepton Event Selection</b>	<b>44</b>
4.1 Electron Selection Cuts . . . . .	44

4.2	Muon Selection Cuts . . . . .	46
4.3	$b$ -Tagging Algorithms . . . . .	48
4.4	Event Selection Cuts . . . . .	52
4.5	Event Selection Efficiencies . . . . .	54
4.6	Background Events in the Dilepton Channel . . . . .	57
4.6.1	$W^+W^-$ . . . . .	58
4.6.2	Drell-Yan . . . . .	59
4.6.3	$Z^0 \rightarrow \tau^+\tau^-$ . . . . .	60
4.6.4	$b\bar{b}$ . . . . .	61
4.6.5	Fake leptons . . . . .	62
4.6.6	Mismeasured Muon Tracks . . . . .	63
4.6.7	$W^\pm Z^0$ and $Z^0 Z^0$ . . . . .	63
4.6.8	Other Backgrounds . . . . .	64
4.6.9	Summary of the Background Sources . . . . .	66
4.7	Dilepton Event Data Sample . . . . .	66
<b>5</b>	<b>Top Quark Mass Determination</b>	<b>68</b>
5.1	The Initial Problem . . . . .	68
5.2	The Dalitz-Goldstein Method . . . . .	69
5.2.1	Choice of Constraints . . . . .	69
5.2.2	Geometrical Construction . . . . .	70
5.2.3	Likelihood Technique . . . . .	71
5.3	Data Sample . . . . .	75
5.4	Joint Likelihood Method . . . . .	77
5.5	Preliminary Monte Carlo Studies . . . . .	80
5.5.1	Monte Carlo Event Samples . . . . .	81
5.5.2	Relative Likelihood Factors . . . . .	82
5.5.3	Studies Using Jet-Parton Matching . . . . .	82
5.5.4	Mapping Function . . . . .	86
5.5.5	Effect of Background Events . . . . .	90
5.6	Application to Run 1 Data . . . . .	93
5.7	Statistical Errors . . . . .	95
5.8	Systematic Errors . . . . .	102



5.8.1	Jet Energy Scale . . . . .	103
5.8.2	Final and Initial State Radiation . . . . .	105
5.8.3	Monte Carlo Generators . . . . .	108
5.8.4	Parameterization of Mapping Function . . . . .	108
5.8.5	Structure Functions for Event Generation . . . . .	108
5.8.6	Structure Functions for Fitter . . . . .	109
5.8.7	Background Sources . . . . .	109
5.8.8	Parameterization of Background Induced Mass Shift . . . . .	111
5.8.9	Top Quark Polarization . . . . .	112
5.8.10	Total Systematic Error . . . . .	112
<b>6</b>	<b>Conclusions</b>	<b>114</b>
6.1	Final Results . . . . .	114
6.2	Checking the Method . . . . .	114
6.2.1	Blind Test . . . . .	114
6.2.2	Application to Lepton+Jets Events . . . . .	115
6.2.3	Other Cross Checks . . . . .	119
6.3	Comparison to Other Methods . . . . .	119
6.3.1	Kinematical Distributions . . . . .	122
6.3.2	Invariant Mass of Charged Lepton and $b$ Quark . . . . .	123
6.3.3	Neutrino Weighting Method . . . . .	124
6.3.4	Modified MINUIT Fitter . . . . .	127
6.3.5	Distinguishing Features of the Dalitz-Goldstein Method . . . . .	129
	<b>Appendix A. CDF Coordinate System</b>	<b>131</b>
	<b>Appendix B. CDF Kinematic Variables</b>	<b>133</b>
	<b>Appendix C. Uncertainty on the Mean</b>	<b>135</b>
	<b>Bibliography</b>	<b>136</b>

# List of Tables

1.1	Standard Model lepton generations. . . . .	4
1.2	Standard Model quark generations. . . . .	6
1.3	Decay modes and branching ratios for a $t\bar{t}$ pair. . . . .	17
2.1	Properties of the calorimetry components used by the Run 1 CDF detector. . . . .	31
3.1	Fitted DLJSCO parameters for a top quark mass of 170 GeV/c <sup>2</sup> . . . .	42
3.2	Mean and R.M.S. of $R$ for a top quark mass of 170 GeV/c <sup>2</sup> . . . . .	42
3.3	Fitted parameters of mass dependent quadratic functions utilized by DLJSCO. . . . .	43
4.1	Electron selection requirements for the CDF dilepton event analysis. .	47
4.2	Muon selection requirements for the CDF dilepton event analysis. . . .	48
4.3	Efficiencies for the Run 1B dilepton event selection cuts. . . . .	57
4.4	Expected background for the dilepton event sample of Run 1. . . . .	66
5.1	Variation of pull distribution width with number of data events. . . .	105
5.2	Jet energy scale uncertainties for $M_t = 160$ GeV/c <sup>2</sup> . . . . .	107
5.3	Mass shift due to background fluctuations. . . . .	111
5.4	List of Systematic Errors ( $M_t = 160$ GeV/c <sup>2</sup> and $H_T$ cut applied). . .	113
6.1	Top quark mass results using different mapping functions. . . . .	115
6.2	Results of the fits to the double-tagged lepton+jets events. . . . .	118

# List of Figures

1.1	Feynman diagram showing $t\bar{t}$ pair production via $q\bar{q}$ annihilation and the possible Standard Model decay channels for the $t\bar{t}$ pair. . . . .	19
2.1	Fermilab's Run 1 particle accelerator (looking south). . . . .	26
2.2	A cross-sectional view of one quadrant of the Run 1 CDF detector. . .	27
2.3	Schematic of an SVX module. . . . .	28
2.4	Cross-sectional view of the Central Tracking Chamber. . . . .	30
2.5	The $\phi - \eta$ segmentation of 1 octant of the CDF calorimetry. . . . .	32
2.6	A track passing through the 4 layers of a muon drift chamber. . . . .	33
4.1	Schematic of a secondary vertex from $b$ quark decay. . . . .	50
5.1	Three superimposed versions of the function $P(X_{t\bar{t}})$ . . . . .	72
5.2	Combination likelihood distributions for data event 41540_127085. . .	76
5.3	Combination likelihood distributions for data event 45047_104393. . .	77
5.4	Combination likelihood distributions for data event 63700_272140. . .	78
5.5	Combination likelihood distributions for data event 57621_45230. . . .	79
5.6	Combination likelihood distributions for data event 66046_380045. . .	80
5.7	Combination likelihood distributions for data event 69808_639398. . .	81
5.8	Combination likelihood distributions for data event 67581_129896. . .	82
5.9	Best combination likelihood distributions for each data event. . . . .	83
5.10	Joint likelihood distributions obtained from the data sample with (a) no constant value added to the zero entry bins and (b) a small constant value added to the zero entry bins. Gaussian fits to the distributions are also displayed, along with their mean and sigma values. . . . .	84
5.11	Reconstructed top quark mass vs. HERWIG Monte Carlo top quark mass for (a) "correct" jet-lepton combinations, (b) "flipped" jet-lepton combinations and (c) "wrong" jet-lepton combinations, using lepton kinematics taken directly from Monte Carlo. . . . .	85
5.12	Distributions of reconstructed $M_t$ obtained from pseudo-experiments. .	87
5.13	The mapping function and its corridor of errors. . . . .	88

5.14	Reconstructed top quark mass vs. HERWIG Monte Carlo top quark mass for (a) "correct" jet-lepton combinations, (b) "flipped" jet-lepton combinations and (c) "wrong" jet-lepton combinations, using lepton kinematics determined by the top mass fitter. . . . .	89
5.15	Shifts in reconstructed top mass when 1 out of 8 pseudo-experiment events used to form each joint likelihood distribution is a $W^+W^-$ event. From left to right the plots refer to HERWIG Monte Carlo top quark masses of 130, 160 and 220 GeV/c <sup>2</sup> , respectively. Gaussian fits to these histograms are also shown, along with their means and sigmas. . . . .	91
5.16	Parameterization of the mean mass shifts for Monte Carlo top quark masses of 130, 140, 150, 160, 170, 180, 190 and 220 GeV/c <sup>2</sup> , when 1 out of 8 pseudo-experiment events used to form each joint likelihood distribution is a $W^+W^-$ event. The left-hand plot uses the means of Gaussian fits to the mass shift distributions. . . . .	92
5.17	Shifts in reconstructed top mass when 2 out of 9 pseudo-experiment events used to form each joint likelihood distribution are $W^+W^-$ events. From left to right the plots refer to HERWIG Monte Carlo top quark masses of 130, 160 and 220 GeV/c <sup>2</sup> , respectively. Gaussian fits to these histograms are also shown, along with their means and sigmas. . . . .	93
5.18	Parameterization of the mean mass shifts for MC Monte Carlo top quark masses of 130, 140, 150, 160, 170, 180, 190 and 220 GeV/c <sup>2</sup> , when 2 out of 9 pseudo-experiment events are $W^+W^-$ events. The left-hand plot uses the means of Gaussian fits to the mass shift distributions. . . . .	94
5.19	Joint Likelihood distribution for Run 1 dilepton data events when the $H_T$ cut has been applied. . . . .	95
5.20	The mapping function derived from HERWIG Monte Carlo pseudo-experiments and its intersection with the mean mass of the joint likelihood distribution constructed from data. The $\pm 1 \sigma$ lines of the joint likelihood distribution are also shown. . . . .	96

5.21	R.M.S. values of joint likelihood distributions that were constructed from 7-event pseudo-experiments generated by HERWIG Monte Carlo using top quark masses of (a) 140 (b) 150 (c) 160 and (d) 170 GeV/c <sup>2</sup> . Gaussian fits to these histograms, along with their means and sigmas, are also displayed. . . . .	97
5.22	Linear parameterization of the mean R.M.S. values of joint likelihood distributions for pseudo-experiments generated by HERWIG Monte Carlo over the top quark mass range: $130 < M_t^{MC} < 220$ GeV/c <sup>2</sup> . . . .	98
5.23	Using the mapping function derived from HERWIG Monte Carlo events to correct the statistical error. . . . .	99
5.24	Application of the complete mass fitting technique, including mapping function corrections, to a set of 8-event pseudo-experiments generated by HERWIG Monte Carlo using a top quark mass of 160 GeV/c <sup>2</sup> . . .	100
5.25	Application of the complete mass fitting technique, including mapping function corrections, to a set of 4-event pseudo-experiments generated by HERWIG Monte Carlo using a top quark mass of 160 GeV/c <sup>2</sup> . . .	101
5.26	Application of the complete mass fitting technique, including mapping function corrections, to a set of 7-event pseudo-experiments generated by HERWIG Monte Carlo using a top quark mass of 160 GeV/c <sup>2</sup> . . .	102
5.27	Application of the complete mass fitting technique, including mapping function corrections, to a set of 10-event pseudo-experiments generated by HERWIG Monte Carlo using a top quark mass of 160 GeV/c <sup>2</sup> . . .	103
5.28	Application of the complete mass fitting technique, including mapping function corrections, to a set of 16-event pseudo-experiments generated by HERWIG Monte Carlo using a top quark mass of 160 GeV/c <sup>2</sup> . . .	104
5.29	Mass shift due to jet energy uncertainty as a function of top mass. . .	106
5.30	Best combination likelihood distributions for pseudo-experiments using two different types of structure functions in the mass fitter. MRSD0 structure functions were used for the distributions in the left-hand column. The right-hand column shows the same pseudo-experiments when Duke-Owens structure functions were used in the fitter. . . . .	110

6.1	Distribution of top quark masses reconstructed from the CDF blind sample using a mapping function derived from HERWIG Monte Carlo events. . . . .	116
6.2	Distribution of top quark masses reconstructed from the CDF blind sample using a mapping function derived from PYTHIA Monte Carlo events. . . . .	117
6.3	Application of the complete mass fitting technique, including mapping function corrections, to a set of 8-event pseudo-experiments generated by HERWIG Monte Carlo using a top quark mass of 150 GeV/c <sup>2</sup> . . .	120
6.4	Application of the complete mass fitting technique, including mapping function corrections, to a set of 8-event pseudo-experiments generated by HERWIG Monte Carlo using a top quark mass of 170 GeV/c <sup>2</sup> . . .	121
6.5	Reconstructed top quark mass distribution R.M.S. vs. average joint likelihood distribution R.M.S. for 8-event pseudo-experiments generated by Herwig Monte Carlo using a top quark mass of 160 GeV/c <sup>2</sup> . .	122

# Measurement of the Top Quark Mass by Application of the Dalitz-Goldstein Method to Dilepton Events

# Chapter 1

## Introduction

This dissertation describes a measurement of the top quark mass by application of the Dalitz-Goldstein mass fitting technique to dilepton channel data events. Chapter 1 gives a brief description of the most simple and successful theoretical model that incorporates the elementary building blocks of matter and their associated forces of interaction. The top quark's importance in this model, its production mechanism, its decay modes and its history of discovery are also presented. Chapter 2 describes the experimental apparatus used to produce and detect the data events used by this analysis. Chapter 3 discusses standard algorithms designed to reconstruct and correct the kinematics of jets in the data events. Chapter 4 outlines a standard procedure to extract dilepton events from the reconstructed data events. The efficiency for this procedure is also presented. Potential remaining sources of signal contamination are described and the expected levels of these background events in the final data set are quantified. The main analysis is presented in chapter 5. The Dalitz-Goldstein method, the likelihood technique, the use of Monte Carlo simulations, the treatment of background events, and the calculation of statistical and systematic errors are fully described. In chapter 6 the final results are summarized and some consistency checks of the method are presented. In addition, four other dilepton channel mass fitting techniques are briefly described and their results are presented. The dissertation concludes by summarizing the distinguishing features of the Dalitz-Goldstein method.

All measurable quantities presented in this document will be expressed via the system of "natural" units, which are the most convenient units for quantifying typical dimensions encountered in the study of particle physics. In this system all measurements are expressed in units of GeV,  $c$  and  $\hbar \equiv h/2\pi$ , where  $c$  is the speed of light in vacuum and  $h$  is Planck's constant. Therefore, unlike the system of MKS units, which describes measurable quantities in units of length, mass and time, the system of natural units expresses measurements in units of energy, velocity and angular momentum. Since  $c = \hbar = 1$  in natural units, these symbols will not appear in any of the formulae presented in this dissertation. However, they will be used whenever measurements are quantified.



## 1.1 Constituents of Matter and Interactions

According to the Standard Model, which is presently the most popular and experimentally tested theory of particle physics, all matter is composed of two families of fermions (i.e. particles with half-integer spin) called leptons and quarks. These fermions are the smallest known constituents of matter. The electron is an example of a lepton, while protons and neutrons are composite particles consisting of two different types of quarks.

Leptons and quarks interact with each other via the exchange of bosons (i.e. particles of integer spin) called gauge bosons. At sufficiently low exchange energies these interactions have four distinct manifestations: the strong, electromagnetic, weak and gravitational forces. The strong force is attractive and short range. It is responsible for the binding of protons and neutrons to form atomic nuclei. The electromagnetic force between two particles is directly proportional to the product of their electric charges and is inversely proportional to the square of their spatial separation. It is attractive (repulsive) if the particles have opposite (the same) signs of electric charge. This force is responsible for the binding of electrons to nuclei to form atoms. The electromagnetic force is weaker than the strong force by approximately two orders of magnitude<sup>[1]</sup>, which explains why protons bind to form nuclei despite the electromagnetic forces of repulsion between them. The weak force is short range and approximately five orders of magnitude smaller than the strong force. It is responsible for such processes as neutron decay and the expected decay modes of the top quark (see section 1.2.1). The gravitational force between two particles is directly proportional to the product of their masses and inversely proportional to the square of their spatial separation. Unlike the electromagnetic force, gravity is purely attractive. Nomenclature is deceiving, as the gravitational force is weaker than the so-called weak force by approximately 37 orders of magnitude. While its cumulative effects become significant for bodies with astronomical mass like our earth, gravity can be ignored for interactions between high energy subatomic particles.

This section gives a brief description of leptons, quarks and gauge bosons and concludes by showing how they are accommodated by the Standard Model. In all discussions below it will be assumed that for every type of particle there exists an "antiparticle", which has the same mass as its associated particle but whose quantum

numbers (e.g. electric charge) are of opposite sign. When a particle and its associated antiparticle collide they annihilate each other by creating a gauge boson.

### 1.1.1 Leptons and Quarks

Leptons have spin  $\frac{1}{2}\hbar$  and can be categorized into two groups: The charged leptons ( $l$ ) and the neutrinos ( $\nu$ ). Charged leptons have electric charge  $-e$ , where  $e \approx 0.303 (\hbar c)^{1/2}$ . These leptons can experience both electromagnetic and weak forces. The electron ( $e^-$ ) is the lightest charged lepton, with a mass of  $m_e = 5.11 \times 10^{-4} \text{ GeV}/c^2$ . The next heaviest charged lepton is the muon ( $\mu^-$ ), whose mass is  $m_\mu = 0.105 \text{ GeV}/c^2$ . One additional charged lepton called the tau lepton ( $\tau^-$ ) has been discovered, with a mass of  $m_\tau = 1.78 \text{ GeV}/c^2$ . Unlike the electron, the muon and the tau lepton are unstable and quickly decay into other particles. Neutrinos are electrically neutral particles that are massless within the accuracy of almost all current measurements (results of recent searches for finite neutrino mass can found in references [2] and [3]). Neutrinos do not participate in processes that involve the strong or the electromagnetic force. They do participate in weak processes, and due to some experimentally observed conservation laws in these processes, neutrinos must exist in three types: the electron neutrino ( $\nu_e$ ), the muon neutrino ( $\nu_\mu$ ) and the tau lepton neutrino ( $\nu_\tau$ ), each type being associated with one of the charged leptons. Therefore, the leptons are naturally grouped into the three "generations" shown in table 1.1. The antileptons are represented symbolically by  $e^+$  (usually called the "positron"),  $\mu^+$ ,  $\tau^+$ ,  $\bar{\nu}_e$ ,  $\bar{\nu}_\mu$  and  $\bar{\nu}_\tau$ .

Generation:	I	II	III	Electric Charge
	$e^-$	$\mu^-$	$\tau^-$	$-e$
	$\nu_e$	$\nu_\mu$	$\nu_\tau$	0

Table 1.1: Standard Model lepton generations.

Like leptons, quarks ( $q$ ) have spin  $\frac{1}{2}\hbar$ . The Standard Model postulates that quarks exist in six different "flavors" called up ( $u$ ), down ( $d$ ), strange ( $s$ ), charm ( $c$ ), bottom ( $b$ ) and top ( $t$ ). These flavors are listed in order of increasing mass, with the masses of the first five flavors ranging between 0.02 and 4.5  $\text{GeV}/c^2$  (see reference [4] for details about the measurements of these masses). While the exact determination of the top

quark mass is the subject of this dissertation, a lower limit of  $131 \text{ GeV}/c^2$  was already placed on it in 1994 (see section 1.2.2) making it at least 29 times larger than the next heaviest quark mass. The antiquarks ( $\bar{q}$ ) exist in six "antiflavors" represented symbolically by  $\bar{u}$ ,  $\bar{d}$ ,  $\bar{s}$ ,  $\bar{c}$ ,  $\bar{b}$  and  $\bar{t}$ . Quarks are the building blocks of particles called hadrons, of which there are two types: baryons and mesons. They are distinguished by the combination of quarks (called "valence" quarks in this context) that give them their identity. Baryons are bound states of three quarks and are therefore fermions. Some examples are the proton, which consists of two  $u$  quarks and a  $d$  quark, and the neutron, which consists of a  $u$  quark and two  $d$  quarks. Mesons are bound states of a quark and an antiquark and are therefore bosons. An example of a meson is the  $\pi^+$  meson, which consists of a  $d$  quark and a  $\bar{d}$  quark. Since the proton and the  $\pi^+$  meson have electric charge  $+e$  and the neutron is electrically neutral, the quark charges must be fractions of  $e$ . The  $u$ ,  $c$  and  $t$  quarks have electric charge  $+\frac{2}{3}e$  while the  $d$ ,  $s$  and  $b$  quarks have charge  $-\frac{1}{3}e$ . All signs are reversed for the associated antiquarks. The  $c$ ,  $s$ ,  $b$  and  $t$  quarks are highly unstable and quickly decay into other particles. Therefore, all stable hadrons consist entirely of  $u$  and  $d$  quarks. Particles containing the other quarks must be created in the lab.

In order to fit all observed hadrons into the quark scheme, while still satisfying Fermi statistics for fermions and excluding states that have never been observed, each flavor of quark is postulated to possess a quantum number called "color" that can have three different states: red ( $R$ ), green ( $G$ ) and blue ( $B$ ). Similarly, antiquarks can have the color quantum numbers: antired ( $\bar{R}$ ), antigreen ( $\bar{G}$ ) and antiblue ( $\bar{B}$ ). These quantum numbers are defined so that a  $RGB$  quark combination, a  $\bar{R}\bar{G}\bar{B}$  quark combination or a combination of any color quark with its corresponding anticolor quark leads to a so-called "colorless" particle. All observed hadrons are required to be colorless so that each quark in a baryon must have a different color and each meson must consist of color-anticolor quark combinations. This requirement is consistent with experimental results and accommodates the fact that single quarks have never been observed in nature.

In analogy to leptons, the quark flavors are arranged into the three generations shown in table 1.2. The motivation for this scheme will become clear after the discussion of weak forces and the CKM matrix in section 1.1.2.

Generation:	I	II	III	Electric Charge
	$u$	$c$	$t$	$+(2/3)e$
	$d$	$s$	$b$	$-(1/3)e$

Table 1.2: Standard Model quark generations.

### 1.1.2 Gauge Bosons

According to quantum field theory, all observed forces are the result of the emission and reabsorption of particles called gauge bosons by the fundamental constituents of matter. Since leptons and quarks have half-integer spin the gauge bosons must have integer spin to conserve angular momentum.

The electromagnetic force is experienced by electrically charged particles and is mediated by a massless gauge boson with spin  $\hbar$ , called the photon ( $\gamma$ ). When an electrically charged particle emits a photon it recoils to conserve momentum. Since the energy of the particle must also be conserved, the photon can only live within a finite time interval allowed by the Heisenberg uncertainty principle. For this reason, all gauge bosons are virtual. The photon will subsequently be reabsorbed by another charged particle, causing this particle to recoil too. The net effect is the observed electromagnetic repulsion (or attraction) between two charged particles. The electromagnetic force can be experienced by the charged leptons and all six flavors of quarks. The complete theory of subatomic electromagnetic interactions is referred to as quantum electrodynamics (QED).

Hadrons experience the strong force because their constituent quarks possess color. In analogy to electric charge, which creates an electric field, "color charge" creates a "color field". However, when two quarks interact strongly they actually exchange color. This process is mediated by the exchange of massless gauge bosons with spin  $\hbar$  called gluons ( $g$ ). To conserve color gluons must have color too, but in specific combinations of a color and an anticolor. For example, a  $G$  quark can change into a  $R$  quark by exchanging a  $R\bar{G}$  gluon with a  $R$  quark which itself will turn into a  $G$  quark. There are eight types of gluons, each type corresponding to a different possible color-anticolor combination. Since gluons possess color they can interact with other gluons. There is no analogy to this phenomenon in electromagnetic interactions, since photons are electrically neutral.

Unlike the electromagnetic force, which decreases with increased separation between the interacting particles, the color force actually increases with increased separation. This property confines the quarks to composite colorless objects and explains why free quarks are never observed in nature. For instance, when a quark and an antiquark separate, the potential energy between them eventually becomes large enough to produce a new  $q\bar{q}$  pair. This process continues until the energy for producing such pairs is depleted and there exists two separate beams, or "jets", of low internal energy  $q\bar{q}$  pairs moving in the same respective directions as the original  $q\bar{q}$  pair. It is the hadrons formed from these colorless  $q\bar{q}$  pairs, not the quarks themselves, that are detected experimentally. The original quark and antiquark are said to have "hadronized" into two "jets".

The complete theory of color interactions is referred to as quantum chromodynamics (QCD). According to QCD, the valence quarks of a hadron radiate a so-called "sea" of gluons and virtual  $q\bar{q}$  pairs that are in a state of continuous creation and annihilation. Therefore, quarks and gluons are often referred to collectively as "partons" since they each form part of a hadron.

The weak force can be experienced by all leptons and quarks and is mediated by the exchange of massive gauge bosons with spin  $\hbar$  called weak bosons. Upon emission of certain types of weak bosons, a lepton (quark) can transform into another type of lepton (quark). These transformations always result in an electric charge difference of  $e$  between the particle states before and after weak boson emission. Therefore, a "charge-lowering" ("charge-raising") transformation must be accompanied by the emission of a weak boson of charge  $+e$  ( $-e$ ). These two bosons, which form a particle-antiparticle pair, are called the  $W^+$  and  $W^-$  bosons. The arrangement of leptons into the three generations shown in Table 1.1 is motivated by the experimental observation that leptons only transform within their own generations (a law that is expected to be broken if neutrinos have finite mass). For quarks, inter-generational charge-raising and charge-lowering transformations are allowed. However, transformations are much more likely to occur within generations than across generations. These probabilities are summarized nicely by the Cabibbo-Kobayashi-Maskawa (CKM) matrix, which has the form<sup>[5]</sup>:

$$V = \begin{pmatrix} |V_{ud}| = 0.9751 \pm 0.0006 & |V_{us}| = 0.2215 \pm 0.0025 & |V_{ub}| = 0.0035 \pm 0.0015 \\ |V_{cd}| = 0.221 \pm 0.003 & |V_{cs}| = 0.9743 \pm 0.0007 & |V_{cb}| = 0.041 \pm 0.005 \\ |V_{td}| = 0.009 \pm 0.005 & |V_{ts}| = 0.040 \pm 0.006 & |V_{tb}| = 0.9991 \pm 0.0002 \end{pmatrix}$$

For example, this matrix shows that an up quark is  $|V_{ud}|^2/|V_{us}|^2 \approx 20$  times more likely to transform into a down quark than into a strange quark upon emission of a  $W^+$  boson. In addition to the charge-raising and charge-lowering weak interactions (which will be referred to collectively as "charge-changing" weak interactions), there is a third type of weak interaction that is mediated by an electrically neutral gauge boson called the  $Z^0$  boson. Experiments suggest that particle transformation is not possible in this type of weak process. In fact, the CKM matrix was designed to forbid all quark flavor-changing neutral currents.

Using the Klein-Gordon equation it can be shown that the range of a force is inversely proportional to the mass of its associated gauge boson. The mass of the  $W^\pm$  bosons is  $M_W = 80 \text{ GeV}/c^2$  and the mass of the  $Z^0$  boson is  $M_Z = 91 \text{ GeV}/c^2$ , thus accounting for the weak force's short range. The Standard Model postulates that the observed disparity in strengths between the electromagnetic and weak forces for low energy interactions is primarily due to the large masses of the weak bosons, so that for gauge boson energies much greater than the weak boson rest energies the two forces may merge into a single force called the electroweak interaction.

Experiments show that only left-handed<sup>[6]</sup> fermions exchange  $W$  bosons, which implies that at very high energies only negative (positive) helicity fermions (antifermions) decay via the charge-changing weak interaction. It follows that these interactions are not invariant under either the parity operation,  $P$  (also known as space inversion), or the charge conjugation operation,  $C$  (which changes a particle into its antiparticle). However, most charge-changing weak interactions are invariant under the combination of  $P$  and  $C$  operations. Subtle violations of  $CP$  invariance have been observed in some types of weak interactions, namely neutral kaon decays. To allow for such violations the dimensions of the CKM matrix must be at least  $3 \times 3$ . This was one of the original reasons for postulating a third generation of quarks, which includes the top quark.

The gravitational force is presumed to be mediated by gauge bosons with spin  $2\hbar$ , called gravitons. However, the effects of these gauge bosons are negligible for high energy subatomic particles.

### 1.1.3 The Standard Model

The Standard Model is a particle physics theory which postulates that all matter is composed of quarks and leptons and that the fundamental forces of nature are mediated by gauge bosons. To unify the electromagnetic and weak forces and account for all observed fermion and gauge boson masses, while still keeping the theory renormalizable (i.e free from divergences), the Standard Model effectively introduces a new hypothetical particle. The main features of the model are presented here.

In quantum field theory, interactions involving fermions and gauge bosons may be represented by functions of space-time called Lagrangian densities. The Lagrangian density,  $\mathcal{L}$ , for a given process is defined so that the equation of motion for any fermion or gauge boson participating in that process is given by:

$$\frac{\partial}{\partial x_\mu} \left( \frac{\partial \mathcal{L}}{\partial(\partial\psi/\partial x_\mu)} \right) - \frac{\partial \mathcal{L}}{\partial \psi} = 0 \quad (1.1)$$

where  $\psi$  is the wave function (field) of the given fermion (gauge boson). Many useful physical quantities can be efficiently calculated from the Lagrangian density, including decay rates, branching ratios and particle masses.

According to Noether's theorem, for every type of continuous transformation that leaves a given physical system's equations of motion unchanged there exists a conserved quantity. For example, requiring all physics experiments to be invariant under translations in space leads to the conservation of linear momentum. Equation 1.1 implies that a sufficient condition for a system's equations of motion to be invariant under a given transformation is that its Lagrangian density remain unchanged. For example, the QED Lagrangian density for a charged fermion of mass  $m$  in a photon field,  $A_\mu$ , is:

$$\mathcal{L} = \bar{\psi}(i\gamma^\mu \partial_\mu - m)\psi - e\bar{\psi}\gamma^\mu Q\psi A_\mu - \frac{1}{4}F_{\mu\nu}F^{\mu\nu} \quad (1.2)$$

where  $\psi$  is the fermion's wave function,  $F_{\mu\nu}$  is the electromagnetic field strength tensor and  $Q$  is the charge operator, whose eigenvalue is the electric charge (divided by  $e$ ) of the given fermion. The first term of  $\mathcal{L}$  leads to Dirac's equation for a free fermion of mass  $m$  and the remaining two terms lead to Maxwell's equation for an electromagnetic field,  $A_\mu$ , in the presence of a four-vector current,  $j^\mu = e\bar{\psi}\gamma^\mu Q\psi$ . The second term of  $\mathcal{L}$  is also interpreted as the interaction or "coupling" between the

fermion and the photon field, where  $e$  is defined as the "coupling strength" of the electromagnetic interaction in this context. An interesting aspect of equation 1.2 is that it can be derived by requiring that the Dirac equation Lagrangian density be invariant under a "gauge" (i.e. phase) transformation of the fermion wave function given by:

$$\psi \rightarrow e^{i\alpha(x)Q}\psi \quad (1.3)$$

where  $\alpha(x)$  is any function of space-time. Equation 1.3 is called a "local" (because  $\alpha$  depends on space-time)  $U(1)_Q$  gauge transformation and the charge operator,  $Q$ , is called the generator of this transformation. Invariance of  $\mathcal{L}$  under this transformation effectively "generates" the photon field by requiring the presence of the coupling term in equation 1.2. It is believed that the fields of all gauge bosons can be generated by requiring some form of local gauge invariance.

The Standard Model's Lagrangian density for electroweak interactions is motivated by the experimental observation that these interactions are invariant under two particular types of local gauge symmetry groups called weak isospin,  $SU(2)_L$ , and weak hypercharge,  $U(1)_Y$ . The subscript  $L$  reflects the fact that only left-handed leptons and quarks experience the charge-changing weak force. Under  $SU(2)_L \times U(1)_Y$  transformations the particle wave functions transform as:

$$\psi_L \rightarrow e^{i\vec{\alpha}(x) \cdot \vec{T} + i\beta(x) \frac{Y}{2}} \psi_L \quad (1.4)$$

$$\psi_R \rightarrow e^{i\beta(x) \frac{Y}{2}} \psi_R \quad (1.5)$$

where  $\vec{\alpha}(x)$  and  $\beta(x)$  are arbitrary functions of  $x$ ,  $\vec{T} \equiv \hat{x}T^1 + \hat{y}T^2 + \hat{z}T^3$  is the generator of rotations in weak isospin space, and  $Y \equiv 2(Q - T^3)$  is the weak hypercharge operator. The components of  $\vec{T}$  are the Pauli spin matrices, multiplied by  $\frac{1}{2}$ . By convention, the basis of the  $SU(2)_L$  representation is chosen as the eigenvectors of the third component of  $\vec{T}$ . These are the two component column vectors,  $\begin{pmatrix} 1 \\ 0 \end{pmatrix}$  and  $\begin{pmatrix} 0 \\ 1 \end{pmatrix}$ , with eigenvalues,  $T^3 = +\frac{1}{2}$  and  $T^3 = -\frac{1}{2}$ , respectively.  $\psi_L$  is a doublet in weak isospin space whose components are the left-handed components of the wave functions of any two lepton or quark states that can transform into each other via the charge-changing weak force. By convention, these doublets are constructed so



that the top-most component (i.e. the component with  $T^3 = +\frac{1}{2}$ ) has the most positive electric charge. To allow for inter-generational quark transformations the  $T^3 = -\frac{1}{2}$  components of  $\psi_L$  consist of linear combinations of the  $d$ ,  $s$ , and  $b$  quark wave functions, with coefficients determined by the CKM matrix.  $\psi_R$  is a weak isospin singlet with  $T^3 = 0$  and can be the right-handed component of any lepton or quark wave function.

To yield the expected equations of motion for the fermion wave functions and the gauge boson fields while still remaining invariant to  $SU(2)_L \times U(1)_Y$  gauge transformations, the electroweak Lagrangian density must include the terms:

$$\bar{\psi}_L \gamma^\mu (i\partial_\mu - g\vec{T} \cdot \vec{W}_\mu - g' \frac{Y}{2} B_\mu) \psi_L + \bar{\psi}_R \gamma^\mu (i\partial_\mu - g' \frac{Y}{2} B_\mu) \psi_R - \frac{1}{4} \vec{W}_{\mu\nu} \cdot \vec{W}^{\mu\nu} - \frac{1}{4} B_{\mu\nu} B^{\mu\nu} \quad (1.6)$$

where  $(\vec{W}_\mu \equiv \hat{x}W_\mu^1 + \hat{y}W_\mu^2 + \hat{z}W_\mu^3)$  and  $B_\mu$  are the weak isospin and weak hypercharge vector fields, respectively,  $g$  and  $g'$  are their respective coupling strengths (in analogy to  $e$  in electromagnetic interactions) and the terms involving  $W_{\mu\nu}$  and  $B_{\mu\nu}$  are kinetic energy terms (analogous to the term containing  $F_{\mu\nu}$  in equation 1.2). Now,  $W_\mu^1$  and  $W_\mu^2$  can be expressed in terms of the charged weak boson fields,  $W_\mu^\pm$ . Furthermore,  $W_\mu^3$  and  $B_\mu$  are related to the electromagnetic field,  $A_\mu$ , and the neutral weak boson field,  $Z_\mu$ , by the rotation:

$$A_\mu = \cos\theta_W B_\mu + \sin\theta_W W_\mu^3 \quad (1.7)$$

$$Z_\mu = -\sin\theta_W B_\mu + \cos\theta_W W_\mu^3 \quad (1.8)$$

where  $\theta_W$  is the Weinberg angle (experimentally  $\sin^2\theta_W \approx 0.23$ ). Therefore, equation 1.6 is almost completely analogous to the Lagrangian density for pure electromagnetic interactions given by equation 1.2. It only lacks required terms proportional to the finite masses of the leptons and the weak bosons. Unfortunately, simply adding mass terms like  $-m\bar{\psi}_L\psi_L$  to the Lagrangian density will both destroy its  $SU(2)_L \times U(1)_Y$  invariance and lead to divergences in the theory that cannot be renormalized.

To generate the required mass terms, the Standard Model introduces an isospin doublet,  $\phi$ , of complex scalar fields. The  $T^3 = +\frac{1}{2}$  component of  $\phi$  has electric charge

$Q = 1$  and its  $T^3 = -\frac{1}{2}$  component is neutral, so that  $\phi$  has weak hypercharge  $Y = 1$ . This new field is postulated to have a potential energy,  $V(\phi)$ , of the form:

$$V(\phi) = \mu^2 \phi^\dagger \phi + \lambda (\phi^\dagger \phi)^2 \quad (1.9)$$

where  $\mu$  and  $\lambda$  are arbitrary constants defined such that  $\mu^2 < 0$  and  $\lambda > 0$ . The minimum value of  $V(\phi)$  will be satisfied by an  $SU(2)_L \times U(1)_Y$  invariant manifold of points given by:

$$\phi^\dagger \phi = -\frac{\mu^2}{2\lambda} \quad (1.10)$$

The Standard Model generates the weak boson masses by including the terms:

$$|(i\partial_\mu - g\vec{T} \cdot \vec{W}_\mu - g' \frac{Y}{2} B_\mu)\phi|^2 - V(\phi) \quad (1.11)$$

in the electroweak Lagrangian density and then perturbatively expanding  $\phi$  about one of the points for which  $V(\phi)$  is a minimum. To assure that the photon field remains massless, this point is chosen so that the charged component of  $\phi$  is zero. Its neutral component,  $v/\sqrt{2}$ , is chosen to be real. By choosing a particular expansion point in the  $SU(2)_L \times U(1)_Y$  invariant manifold of points, the  $SU(2)_L \times U(1)_Y$  symmetry is effectively "broken". Now, since  $\phi$  consists of four independent fields, a perturbative expansion of  $\phi$  about a given point will generally introduce four new fields: one with finite mass and three with zero mass called "massless Goldstone bosons". However, it is possible to make a local  $SU(2)_L$  phase transformation of  $\phi$  which eliminates the massless Goldstone bosons and effectively introduces one new real scalar field to the theory called the Higgs field,  $h(x)$ . Its associated particle, which has zero spin, is called the Higgs boson.

Conveniently, this same symmetry breaking mechanism may be used to generate the lepton and quark masses by including additional terms in the Lagrangian density. For example, the term that generates the  $u$  and  $d$  quark masses is:

$$-G_d(\overline{\psi^u}, \overline{\psi^d})_L \phi \psi_R^d - G_u(\overline{\psi^u}, \overline{\psi^d})_L \phi_c \psi_R^u + \text{hermitian conjugate} \quad (1.12)$$

where  $\psi^u$  and  $\psi^d$  are the respective wave functions of the  $u$  and  $d$  quark,  $\phi_c \equiv 2iT^2 \phi^*$ , and  $G_d$  and  $G_u$  are arbitrary parameters introduced into the theory to yield the

experimentally observed masses of the quarks. The electroweak Lagrangian density will contain similar terms for the other quarks and massive leptons.

Hence, with equations 1.6, 1.11 and 1.12, the complete Standard Model electroweak Lagrangian density can be constructed. After expanding  $\phi$ , the masses of the various particles, including that of the hypothesized Higgs boson, can be extracted from terms that are quadratic in a single type of fermion wave function or gauge boson field. The Standard Model predicts the weak boson masses exactly but it only predicts the fermion masses up to the arbitrary constants  $G_u$ ,  $G_d$ , etc and the Higgs boson mass ( $M_H$ ) up to the arbitrary constant  $\lambda$ . There will be other terms that contain combinations of different wave functions and fields. The coefficients of these couplings can be used to calculate the decay rates of various electroweak processes. For instance, the partial width for the Higgs boson to decay into a fermion with wave function,  $f$ , and its associated antifermion is obtained from the expansion term with field dependence,  $h\bar{f}f$ . The coefficient of this term is proportional to  $m_f/M_W$  where  $m_f$  is the fermion's mass. Therefore, the Higgs boson couples only weakly to most leptons and quarks. An exception to this rule is the Higgs coupling to the top quark since this quark has a mass that is comparable and, in fact, larger than that of the  $W^\pm$  bosons.

In quantum chromodynamics, the three different color states of the quarks form a triplet representation of a symmetry group called  $SU(3)_C$ , which contains eight independent non-commuting generators,  $T_a$ . The eight gluon fields,  $G_\mu^a$ , are generated by requiring the Dirac equation Lagrangian densities of the three different quark color states,  $q_j$ , to be invariant under  $SU(3)_C$  transformations. The Lagrangian density then takes the form:

$$\mathcal{L} = \bar{q}_j(i\gamma^\mu\partial_\mu - m)q_j - g_s(\bar{q}_j\gamma^\mu T_a q_j)G_\mu^a - \frac{1}{4}G_{\mu\nu}^a G_a^{\mu\nu} \quad (1.13)$$

where the first term is the sum of the Dirac equation Lagrangian densities for the three color states, the second term represents interaction terms summed over the three color states and the eight gluon fields ( $g_s$  being the QCD coupling strength) and the third term is summed over kinetic energy terms for the gluon fields (the tensors,  $G_{\mu\nu}^a$ , being analogous to  $F_{\mu\nu}$  of QED). In analogy to QED, no symmetry breaking mechanism is needed here since the gluon gauge bosons are massless.

Although the gravitational force is elegantly described by the theory of general relativity, it cannot be incorporated into the Standard Model in terms of gauge boson exchange because gravity has never been successfully quantized. However, it is hoped that a theory exists which combines the gravitational force with other forces in such a way that quantization is possible.

Hence, the Standard Model describes the strong, electromagnetic and weak interactions in terms of a  $SU(3)_C \times SU(2)_L \times U(1)_Y$  gauge invariant Lagrangian density with three different coupling strengths:  $g_s$ ,  $g$  and  $g'$ . Many of the predictions made by the Standard Model have been successfully verified by experiment. An example is the fine structure constant,  $\alpha \equiv e^2/(4\pi\hbar c)$ , which is an asymptotic measure of the electromagnetic coupling strength and can be used to calculate all other physical quantities in QED, via perturbation theory. Theoretically,  $\alpha$  is defined as the electrostatic repulsion energy of two electrons with spatial separation,  $\hbar/mc$ , divided by the electron rest energy. Experiments have yielded:  $\alpha^{-1} = 137.0359895(61)$ , which is in good agreement with theory. In the electroweak sector, the Standard Model requires the weak boson masses to satisfy:

$$M_W = \frac{1}{2} \left( \frac{e}{\sin \theta_W} \right) v \quad (1.14)$$

$$M_Z = \frac{M_W}{\cos \theta_W} \quad (1.15)$$

Using empirically observed numbers for  $v$  and  $\theta_W$ , equations 1.14 and 1.15 yield  $M_W = 77.5 \text{ GeV}/c^2$  and  $M_Z = 88.4 \text{ GeV}/c^2$ , respectively. The weak bosons were discovered by CERN in 1983 and their most recently listed experimentally measured masses are,  $M_W = 80.33 \pm 0.15 \text{ GeV}/c^2$  and  $M_Z = 91.187 \pm 0.0007 \text{ GeV}/c^2$ , in good agreement with theory. The Standard Model also requires:

$$\rho \equiv \frac{M_W^2}{M_Z^2 \cos^2 \theta_W} = 1 \quad (1.16)$$

where  $\rho$  is a measure of the relative strength of the neutral and charge-changing weak interactions. Experimentally,  $\rho$  has been determined to be unity within an accuracy of at least two decimal places. The Standard Model also makes several experimentally verified predictions about electroweak decay rates, including the partial widths for

the possible decay channels of the weak bosons. In short, the Standard Model's predictions are in impressive agreement with all experiments designed to test it thus far.

Despite its strong agreement with empirical observations the Standard Model is generally not regarded as the final answer. The reason for dissatisfaction with the theory is that it includes several incomplete and ad hoc features. First, it assigns three different unrelated coupling strengths to the strong, electromagnetic and weak forces. Consequently, it is believed that the  $SU(3)_C \times SU(2)_L \times U(1)_Y$  model must be a subset of a larger gauge theory called the grand unified theory (GUT) that can be described by a single coupling strength. Second, the Standard Model does not incorporate gravity. For this reason, it is hoped that at high enough energies all four forces can be unified into a single force. Third, the Standard Model does not explain why the constituents of matter are divided into quarks and leptons, each with three different generations. There are several models called supersymmetry (SUSY) theories which attempt to predict these relationships. Fourth, the Standard Model's symmetry breaking mechanism introduces a new particle (the Higgs boson) whose mass can only be measured up to an arbitrary constant. In fact, other symmetry breaking theories generate multiple Higgs bosons. Finally, the Standard Model has a total of nineteen completely arbitrary parameters which include the nine non-zero fermion masses, the three coupling strengths ( $g_s$ ,  $g$ , and  $g'$ ), the two Higgs parameters ( $M_H$  and  $\lambda$ ), four CKM matrix parameters and an additional QCD parameter. If neutrinos are proven to have mass even more arbitrary parameters will enter the theory. Therefore, the Standard Model is generally regarded as a very good low energy approximation to a much larger undiscovered theory that successfully unifies all the laws of physics, much like Newton's laws of physics are a macroscopic approximation of the laws of quantum mechanics and special relativity. More detailed information about the Standard Model and related theories can be found in references [7], [8], [9], [10] and [11].

## 1.2 The Top Quark

The top quark is a spin  $\frac{1}{2}\hbar$  fermion with electric charge  $+\frac{2}{3}e$ . According to the Standard Model, this quark is the  $T_3 = \frac{1}{2}$  component of a third generation of weak isospin quark doublets (see table 1.2). Since the discovery of the  $T_3 = -\frac{1}{2}$  component of this doublet (i.e. the bottom quark) the Standard Model has required the existence of the top quark for two main reasons: First, it is needed to complete the construction of the  $3\times 3$  CKM matrix so that flavor-changing neutral currents are suppressed and CP violating processes like neutral kaon decays are allowed. Second, it is needed to make the electroweak theory renormalizable by contributing terms that will cancel unwanted contributions from the bottom quark. Knowledge of the top quark mass ( $m_t$ ) is important since it is one of the nineteen independent parameters of the Standard Model. For instance,  $m_t$  is needed to determine the top quark's coupling to the Standard Model Higgs boson. It is also required for theoretical calculations of the top quark's total decay width, which can be compared with future experimental results as another test of the Standard Model. Perhaps most importantly,  $m_t$  is needed as a parameter in global fits of electroweak precision measurements designed to predict other Standard Model parameters, most notably  $M_H$ . This section describes the top quark's production and decay mechanisms and its history of discovery.

### 1.2.1 Production and Decay

The top quark events used by this analysis were produced by colliding protons ( $p$ ) with antiprotons ( $\bar{p}$ ) at center-of-mass energies of  $\sqrt{s} = 1.8$  TeV. These  $p\bar{p}$  collisions normally result in low energy exchange scattering between the  $p$  and  $\bar{p}$  constituent partons. Top quark production is only possible in rare instances when the interacting partons from a  $p\bar{p}$  pair undergo large momentum transfer. For  $\sqrt{s} = 1.8$  TeV and  $m_t > 100$  GeV/ $c^2$ , the top quark is predominantly produced in  $t\bar{t}$  pairs, from a virtual gluon which itself is produced by  $q\bar{q}$  annihilation or gluon-gluon ( $gg$ ) fusion. For  $m_t > 150$  GeV/ $c^2$ ,  $q\bar{q}$  annihilation is expected to be responsible for more than 80% of  $t\bar{t}$  production. The  $t\bar{t}$  production cross section ( $\sigma_{t\bar{t}}$ ) is another important measurable attribute of the top quark, as its deviation from Standard Model predictions would signify unexpected production mechanisms and decay modes of the  $t\bar{t}$  pair. (See section 4.5 for a definition of  $\sigma_{t\bar{t}}$  in terms of experimental observables in the dilepton channel.)

The total top quark decay width increases with  $m_t$ , and for top quark masses above the lower limit of 131 GeV/c<sup>2</sup> the  $t\bar{t}$  pair is expected to decay via the charge-changing weak interaction before forming a meson bound state. According to the CKM matrix, the  $t$  ( $\bar{t}$ ) quark will decay almost exclusively into a  $b$  ( $\bar{b}$ ) quark and a  $W^+$  ( $W^-$ ) boson. The  $b$  and  $\bar{b}$  quarks hadronize into jets while each of the  $W$  bosons decay into either a lepton and its associated neutrino ("leptonic" decay) or a  $q\bar{q}$  pair allowed by the CKM matrix that subsequently hadronizes into two jets ("hadronic" decay). All possible decay modes and associated branching ratios for a  $t\bar{t}$  pair are shown in table 1.3, where the symbol  $q\bar{q}'$  signifies any quark-antiquark pair (not including  $t$  or  $\bar{t}$ ) that is allowed by the CKM matrix. The  $t\bar{t}$  decay modes are customarily grouped into three major categories called the all-hadronic, lepton+jets and dilepton decay channels. This classification is also displayed in table 1.3.

Decay Mode	Branching Ratio	Decay Channel
$t\bar{t} \rightarrow (q\bar{q}')b(q\bar{q}'\bar{b})$	36/81	All-hadronic
$t\bar{t} \rightarrow (q\bar{q}')b(e^-\bar{\nu}_e b)$ or $(e^+\nu_e b)(q\bar{q}'\bar{b})$	12/81	Lepton+jets
$t\bar{t} \rightarrow (q\bar{q}')b(\mu^-\bar{\nu}_\mu \bar{b})$ or $(\mu^+\nu_\mu b)(q\bar{q}'\bar{b})$	12/81	
$t\bar{t} \rightarrow (q\bar{q}')b(\tau^-\bar{\nu}_\tau \bar{b})$ or $(\tau^+\nu_\tau b)(q\bar{q}'\bar{b})$	12/81	
$t\bar{t} \rightarrow (e^+\nu_e b)(\mu^-\bar{\nu}_\mu b)$ or $(\mu^+\nu_\mu b)(e^-\bar{\nu}_e b)$	2/81	Dilepton
$t\bar{t} \rightarrow (e^+\nu_e b)(\tau^-\bar{\nu}_\tau \bar{b})$ or $(\tau^+\nu_\tau b)(e^-\bar{\nu}_e \bar{b})$	2/81	
$t\bar{t} \rightarrow (\mu^+\nu_\mu b)(\tau^-\bar{\nu}_\tau \bar{b})$ or $(\tau^+\nu_\tau b)(\mu^-\bar{\nu}_\mu \bar{b})$	2/81	
$t\bar{t} \rightarrow (e^+\nu_e b)(e^-\bar{\nu}_e \bar{b})$	1/81	
$t\bar{t} \rightarrow (\mu^+\nu_\mu b)(\mu^-\bar{\nu}_\mu \bar{b})$	1/81	
$t\bar{t} \rightarrow (\tau^+\nu_\tau b)(\tau^-\bar{\nu}_\tau \bar{b})$	1/81	

Table 1.3: Decay modes and branching ratios for a  $t\bar{t}$  pair.

In the all-hadronic channel both  $W$  bosons decay hadronically so that the final state will consist of six energetic jets. This channel has a large branching ratio ( $\approx 44\%$ ). After correcting for mismeasurement of jet energies by the detector (see sections 3.2) the kinematics of the six jets in the final state can be used to reconstruct the top quark mass by identifying the jets from  $b$  quark hadronization (see section 4.3) and requiring that the  $t$  and  $\bar{t}$  quark masses be equal. This channel has the disadvantage of being heavily contaminated by higher order QCD multijet production processes.

In the lepton+jets channel one  $W$  boson decays hadronically while the other decays leptonically. The branching ratio for this process is also approximately 44%. However, decays involving the extremely short lived  $\tau$  leptons are not included in standard searches so that the effective branching ratio for this channel is approximately 30%. A lepton+jets event must include an energetic charged lepton, which makes it distinguishable from much of the multijet background events that obscure the all-hadronic events. However, lepton+jets events are still contaminated by a smaller class of QCD multijet events that include the direct production of a leptonically decaying  $W$  boson. This background is reduced by requiring the identification of at least one jet from  $b$  quark hadronization. The final state of the lepton+jets channel must include a neutrino which, being uncharged, escapes detection. Therefore, only one mass from the  $t\bar{t}$  pair can be fully reconstructed from the final state kinematics.

In the dilepton channel both  $W$  bosons decay leptonically. Events involving  $\tau$  leptons are not included in standard searches so that the effective branching ratio for this channel is only 5%. The dilepton channel has the additional disadvantage of containing two undetected neutrinos, which makes top quark mass reconstruction from raw data impossible. However, its final state also includes two highly energetic charged leptons which makes it much more distinguishable from the QCD multijet background events that plague the other two channels. Figure 1.1 shows a Feynman diagram of  $t\bar{t}$  pair production, via  $q\bar{q}$  annihilation, followed by all possible  $t\bar{t}$  decay modes. The analysis presented in this dissertation uses top quark data events taken exclusively from the dilepton decay channel.

In accordance with QCD, the quarks and gluons involved in the top quark's production and decay processes can spontaneously radiate gluons. This radiation is divided into two categories called initial state radiation (ISR) and final state radiation (FSR). ISR is defined to occur anytime before the  $t\bar{t}$  pair decays, while FSR is defined as radiation from the  $t\bar{t}$  decay products. Both FSR and ISR lead to the formation of additional jets in the final state. The number of these extra jets depends partly on how jets are defined by the analysis (see section 3.1). Consequently, ISR and FSR are a significant source of errors in the measurement of jet energies. Uncertainty about the effects of ISR and FSR on  $t\bar{t}$  final state kinematics must be included as a systematic error in the determination of the top quark mass (see section 5.8.2).



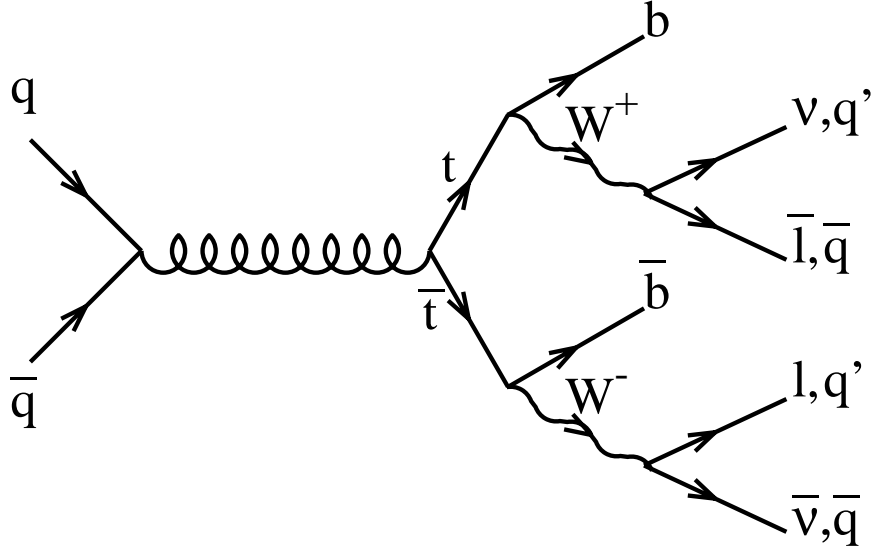


Figure 1.1: Feynman diagram showing  $t\bar{t}$  pair production via  $q\bar{q}$  annihilation and the possible Standard Model decay channels for the  $t\bar{t}$  pair.

### 1.2.2 History of Discovery

Fermilab's discovery of the bottom quark in 1977 and subsequent measurements of its weak isospin quantum number<sup>[12]</sup> helped trigger a series of vigorous searches for the top quark. From the late 1970's to the early 1990's these searches served primarily to set lower limits on the top quark mass. By the late 1980's, experiments performed at  $e^+e^-$  colliders like Tristan, SLC and LEP had placed a lower limit of close to  $50 \text{ GeV}/c^2$  on  $m_t$ . Parallel searches for the top quark by the UA1 and UA2 experiments at CERN's  $\bar{S}p\bar{p}S$   $p\bar{p}$  collider ( $\sqrt{s} = 630 \text{ GeV}$ ) resulted in a lower limit on  $m_t$  of approximately  $70 \text{ GeV}/c^2$ . In 1992 the CDF collaboration at Fermilab's Tevatron  $p\bar{p}$  collider determined a lower limit of  $91 \text{ GeV}/c^2$  on  $m_t$  at the 95% confidence level<sup>[13][14]</sup>. This result confirmed that the top quark is heavy enough to decay into a  $b$  quark and a  $W$  boson. The lower limit on  $m_t$  was increased to  $131 \text{ GeV}/c^2$  in 1994 by Fermilab's D0 collaboration<sup>[15]</sup>.

In April of 1994 the first direct evidence of the top quark's existence was presented by CDF<sup>[16]</sup>, using a data sample consisting of  $19.3 \text{ pb}^{-1}$  of integrated luminosity. A total of 52 candidate lepton+jets events with 3 or more jets were identified. To reduce contamination from  $W + jets$  background events, each lepton+jets event was required

to contain at least one jet identified by a  $b$ -tagging algorithm (see section 4.3). The final lepton+jets sample contained 10 events, 6 of which had a  $b$  quark identified by the SVX  $b$ -tagging algorithm and 7 of which had a  $b$  quark identified by the SLT  $b$ -tagging algorithm. The estimated backgrounds for these two samples were  $2.3 \pm 0.3$  and  $3.1 \pm 0.3$  events, respectively. A total of 2 candidate dilepton events were discovered, with an estimated background of  $0.56^{+0.25}_{-0.13}$  events. By performing a maximum likelihood fit on the 7 lepton+jets events with more than 3 jets, the top quark mass was estimated to be  $m_t = 174 \pm 10(stat.)^{+13}_{-12}(syst.)$  GeV/ $c^2$ . Using the total number of candidate  $t\bar{t}$  events, the estimated number of background events and the known efficiency of the detector, the  $t\bar{t}$  production cross section was determined to be  $\sigma_{t\bar{t}} = 13.9^{+6.1}_{-4.8}$  pb. The difference between the total number of candidate  $t\bar{t}$  events and the total number of expected background events was inconsistent with background fluctuations by 2.8 standard deviations ( $\sigma$ ). This "significance" was not regarded as sufficient confirmation of the top quark's existence. However, in December of 1994 CDF presented results of an analysis<sup>[17]</sup> which provided further evidence that the data was more consistent with  $t\bar{t}$  production than with direct QCD  $W + jets$  production. The study used a 14 event subsample of the original 52 lepton+jets event sample, containing jet kinematics highly uncharacteristic of QCD  $W + jets$  production. Assuming a top quark mass of 170 GeV/ $c^2$ , 8 of these 14 events were found to be more consistent with  $t\bar{t}$  production than with direct QCD  $W + jets$  production. The probability that these events were due to an upward fluctuation in the expected background was determined to be 0.8%.

The D0 collaboration observed a total of 9 candidate  $t\bar{t}$  events in  $13.5 \pm 1.6$  pb $^{-1}$  of data collected during the same period of Tevatron operation used by CDF to obtain its preliminary results. D0 presented their initial findings<sup>[18]</sup> in November of 1994. Of the observed events, 1 was a candidate dilepton event and the remaining 8 were candidate lepton+jets events. Of the lepton+jets events, 4 contained a jet associated with  $b$  quark decay. The expected number of background events for the combined  $t\bar{t}$  sample was  $3.8 \pm 0.9$  events. Assuming a top quark mass of 180 GeV/ $c^2$  (160 GeV/ $c^2$ ), a  $t\bar{t}$  production cross section of  $8.2 \pm 5.1$  pb ( $9.2 \pm 5.7$  pb) was calculated. The significance of this data sample was determined to be  $1.9 \sigma$ , which was also considered too small to fully verify the top quark's existence.

In February of 1995, after having collected an additional  $48 \text{ pb}^{-1}$  of data, the CDF collaboration presented an updated report<sup>[19]</sup> on its search for the top quark. The number of lepton+jets candidate events containing 3 or more jets and least one  $b$ -tag had increased to 37. In this sample, 21 events contained a total of 27 SVX-tagged jets and 22 events contained a total of 23 SLT-tagged jets. Of these events, 6 contained jets identified by both  $b$ -tagging algorithms. The numbers of  $b$ -tags expected from background were  $6.7 \pm 2.1$  and  $15.4 \pm 2.0$  for the SVX-tagged and SLT-tagged samples, respectively. The dilepton event sample increased to 6 events, with an estimated background of  $1.3 \pm 0.3$  events. The entire data sample yielded a significance of  $4.8 \sigma$ , thus providing strong confirmation of the top quark's existence. Using the number of SVX-tagged events, the  $t\bar{t}$  production cross section was calculated to be  $\sigma_{t\bar{t}} = 6.8^{+3.6}_{-2.4}$  pb. A subsample of 19 lepton+jets candidate events with an estimated background contribution of  $6.9^{+2.5}_{-1.9}$  events was used to calculate the top quark mass, with the result:  $m_t = 176 \pm 8(\text{stat.}) \pm 10(\text{syst.}) \text{ GeV}/c^2$ .

After collecting  $50 \text{ pb}^{-1}$  of data the D0 collaboration observed a total of 17  $t\bar{t}$  candidate events. In February of 1995, D0 also presented an analysis of its improved data set<sup>[20]</sup>. This data sample consisted of 14 lepton+jets events and 3 dilepton events. Of the lepton+jets events, 6 contained  $b$ -tagged jets. The total expected background for the entire data sample was  $3.8 \pm 0.6$  events. The significance of the signal was calculated to be  $4.6 \sigma$  thus providing additional convincing evidence of the top quark's existence. With this improved data set, D0 calculated the  $t\bar{t}$  production cross section to be  $\sigma_{t\bar{t}} = 6.4 \pm 2.2$  pb and the top quark mass to be  $m_t = 199^{+19}_{-21}(\text{stat.}) \pm 22(\text{syst.}) \text{ GeV}/c^2$ .

The data collected by the CDF collaboration during the period of Tevatron operation known as Run 1 (from August 1992 to July 1995) had a total integrated luminosity of  $109 \pm 7 \text{ pb}^{-1}$ . A total of 83 candidate lepton+jets events with 4 or more jets were obtained from the Run 1 data sample. After application of a standard  $\chi^2$  cut 76 of the events remained. These events were divided into four groups: Those containing two SVX-tagged jets (5 events), those containing a single SVX-tagged jet (15 events), those containing SLT-tagged jets but no SVX-tagged jets (14 events) and those containing no  $b$ -tagged jets (42 events). The expected backgrounds for these four categories were  $5 \pm 3\%$ ,  $13 \pm 5\%$ ,  $40 \pm 9\%$  and  $56 \pm 15\%$ , respectively and the top

quark masses calculated for these categories were  $m_t = 170.1 \pm 9.3 \text{ GeV}/c^2$ ,  $178.0 \pm 7.9 \text{ GeV}/c^2$ ,  $142_{-14}^{+33} \text{ GeV}/c^2$  and  $181.0 \pm 9.0 \text{ GeV}/c^2$ , respectively. By combining these measurements, a top quark mass of  $m_t = 175.9 \pm 4.8(stat.) \pm 4.9(syst.) \text{ GeV}/c^2$  was measured in the lepton+jets channel and presented by CDF in September of 1997<sup>[21]</sup>.

CDF observed a total of 9 candidate dilepton events in the Run 1 data sample. Of these events,  $2.4 \pm 0.5$  were expected to be background. Two different techniques were used to calculate the top quark mass from these events. One technique estimated  $m_t$  by comparing kinematical distributions from the data to the same distributions for  $t\bar{t}$  events generated by Monte Carlo simulations. The result for this technique was:  $m_t = 159 \pm 23(stat.) \pm 11(syst.) \text{ GeV}/c^2$ . The other technique worked in the rest frame of the  $W$  boson and determined  $m_t$  by measuring the total invariant mass of the  $b$  quark and the charged lepton from  $W$  decay. The result for this method was:  $m_t = 163 \pm 20(stat.) \pm 9(syst.) \text{ GeV}/c^2$ . These two techniques are briefly described in section 6.3. The masses obtained by these methods were combined to yield a top quark mass of  $m_t = 161 \pm 17(stat.) \pm 10(syst.) \text{ GeV}/c^2$ , which was published by CDF in September of 1997<sup>[22]</sup>. Due to its large errors, this result was recently replaced by the value  $m_t = 167.4 \pm 10.3(stat.) \pm 4.8(syst.) \text{ GeV}/c^2$  which was obtained by a technique called the "neutrino weighting method". The details of this new measurement were submitted for publication in January of 1999<sup>[23]</sup> and a brief description of the technique is presented in section 6.3.3. Two other analyses with errors comparable to those obtained from the neutrino weighting method have recently been accepted by CDF. One of them (briefly described in section 6.3.4) applied a lepton+jets mass fitting technique that was appropriately modified for dilepton events. The other one used the Dalitz-Goldstein mass fitting technique and is the main subject of this dissertation.

In March of 1997 CDF presented a measurement of  $m_t$  using candidate all-hadronic events from the Run 1 data sample<sup>[24]</sup>. An application of some standard kinematic requirements yielded 187 candidate all-hadronic events, with an estimated background of  $164.8 \pm 1.2(param.) \pm 10.7(syst.)$  events. The sample contained a total of 222  $b$ -tagged jets. Before calculation of  $m_t$ , the final sample was reduced to 136 events by requiring each event to have at least 6 or more jets, at least one of which was  $b$ -tagged. This analysis calculated a top quark mass of  $m_t = 186 \pm 10(stat.) \pm 12(syst.) \text{ GeV}/c^2$ .

To calculate the  $t\bar{t}$  production cross section from Run 1 lepton+jets data, the CDF collaboration used a data set containing 34 SVX-tagged events with a total of 42 SVX-tagged jets and 40 SLT-tagged events with a total of 44 SLT-tagged jets. There was an overlap of 11 events between the SVX-tagged and SLT-tagged samples. Assuming a top quark mass of  $m_t = 175 \text{ GeV}/c^2$ , production cross sections of  $6.2^{+2.1}_{-1.7}$  pb and  $9.2^{+4.3}_{-3.6}$  pb were measured for the SVX-tagged sample and the SLT-tagged sample, respectively. The production cross section was also measured from the entire Run 1 dilepton event sample, with the result:  $\sigma_{t\bar{t}} = 8.2^{+4.4}_{-3.4}$  pb. For the Run 1 all-hadronic event sample a cross section of  $9.6^{+4.4}_{-3.6}$  pb was calculated from the 187 events that contain at least one SVX-tagged jet. A separate calculation using events with at least two SVX-tagged jets (a total of 157 events) yielded a cross section of  $11.5^{+7.7}_{-7.0}$  pb. In October of 1997 CDF announced a  $t\bar{t}$  production cross section of  $\sigma_{t\bar{t}} = 7.6^{+1.8}_{-1.5}$  pb when the results from all three channels are combined<sup>[25]</sup>.

During Run 1 the D0 collaboration collected of total  $125 \text{ pb}^{-1}$  of data. After application of standard kinematic cuts there remained a total of 77 candidate lepton+jets events, 5 of which contained soft muons identified with  $b$  quark decay. The expected background for this sample was approximately 65%. Based on these events, D0 announced a top quark mass of  $m_t = 173.3 \pm 5.6(\text{stat.}) \pm 6.2(\text{syst.}) \text{ GeV}/c^2$  in March of 1997<sup>[26]</sup>. The total Run 1 data sample also yielded 6 candidate dilepton events, with a background contribution of 23%. Application of a maximum likelihood technique on this data<sup>[28]</sup> yielded a top quark mass of  $m_t = 168.4 \pm 12.3(\text{stat.}) \pm 3.7(\text{syst.}) \text{ GeV}/c^2$ . By combining the results found from the lepton+jets and the dilepton channels a top quark mass of  $m_t = 172.0 \pm 7.5 \text{ GeV}/c^2$  was obtained. Using the entire Run 1 data set and assuming a top quark mass of  $m_t = 173.3 \text{ GeV}/c^2$ , a  $t\bar{t}$  production cross section of  $\sigma_{t\bar{t}} = 5.5 \pm 1.8 \text{ pb}$  was calculated<sup>[27]</sup>. The latest D0 results for measurement of  $m_t$  in the lepton+jets channel and the dilepton channel have recently been submitted for publication and can be found in references [29] and [30], respectively. The  $t\bar{t}$  production cross section has also been updated<sup>[31]</sup> and submitted for publication.

## Chapter 2

# Experimental Apparatus

The experimental apparatus required to create and detect the top quark events used by this analysis is presented. First the  $p\bar{p}$  collision process needed for the creation of  $t\bar{t}$  pairs is outlined. Then the detectors used by the CDF collaboration to record data event kinematics are described. Finally, details about the collaboration's on-line system of data selection are presented. Note that since the collection of the data used by this analysis, the experimental apparatus has been modified significantly in preparation for the next period of data collection which is scheduled to begin in the year 2000. This period (known as Run 2) will be marked by an approximately 100-fold increase in instantaneous luminosity and an estimated 20-fold increase in data collection by the CDF collaboration. Details about the necessary upgrades to the experiment can be found in reference [32].

### 2.1 Particle Acceleration

To generate sufficient energy for the creation of massive particles like the top quark, Fermi National Accelerator Laboratory (Fermilab) collided beams of protons with beams of antiprotons at a total center-of-mass energy of  $\sqrt{s} = 1.8$  TeV. Several stages were used to create, store and accelerate the colliding particles so that this energy could be achieved.

The first stage involved a Cockcroft-Walton electrostatic generator, which would initiate the process by attaching some excess electrons to a collection of hydrogen atoms. The resulting negative ions would then be introduced to a positive voltage where they would be accelerated to an energy of 750 keV before exiting the generator. For the second stage, the negative hydrogen ions from the Cockcroft-Walton would enter a 150 m long linear accelerator called the Linac where their energy would be increased to 400 MeV. Upon exiting the Linac the ions would be converted into protons by passing through a carbon foil that removed their electrons. In the third, stage the protons from the Linac would enter a 75 m radius rapid cycling synchrotron called the Booster. Here the energy of the protons would be raised to 8 GeV and they

would be injected in twelve bunches into a 6.3 km circumference proton synchrotron called the Main Ring (which, in preparation for Run 2, has been replaced by another particle accelerator called the Main Injector<sup>[33]</sup>). In the fourth stage, the proton bunches from the Booster would be recombined into a single bunch and accelerated to an energy of 150 GeV in the Main Ring. For the final stage, the 150 GeV proton bunch would enter another proton synchrotron called the Tevatron, a ring of 1,000 super-conducting magnets located directly below and in the same tunnel as the Main Ring. The Tevatron would then accelerate the proton bunch to an energy of 900 GeV. To achieve full operation, these five stages would be repeated until there were 6 evenly spaced 900 GeV proton bunches circulating in the Tevatron.

To create an antiproton bunch, stages 1 to 3 would be repeated to form a proton bunch in the Main Ring. After the bunch had attained an energy of 120 GeV it would be extracted and transported to a fixed target area. The protons would then be focused on a target where a large number of secondary particles, including antiprotons, would be created. The antiprotons would then be extracted and directed to a Debuncher ring where their momentum would be reduced by the process of stochastic cooling. Following this stage, they would be transferred to an accelerator called the Accumulator ring for temporary storage. When enough antiprotons had been stored they would be reinjected in 8 GeV bunches into the Main Ring, but in a direction opposite to that of the protons. The antiproton bunches would then be recombined into one bunch which would be accelerated to 150 GeV before being injected into the Tevatron where it would reach an energy of 900 GeV. This procedure would be repeated until there were six antiproton bunches in the Tevatron.

When the proton and antiproton bunches had each attained energies of 900 GeV they would be focused for collision in two experimental areas located on the circumference of the Tevatron. These two locations are referred to as the Collider Detector at Fermilab (or the CDF detector) and the D0 detector. This analysis uses data that was collected by the CDF detector during the period of Tevatron operation known as Run 1. This run is divided into two parts called Run 1A and Run 1B. The total integrated luminosity for Run 1A (August 1992 - May 1993) was  $19.3 \text{ pb}^{-1}$  and the total integrated luminosity for Run 1B (January 1994 - July 1995) was  $90.1 \text{ pb}^{-1}$ . An overhead view of Fermilab's Run 1 particle accelerator is shown in figure 2.1.

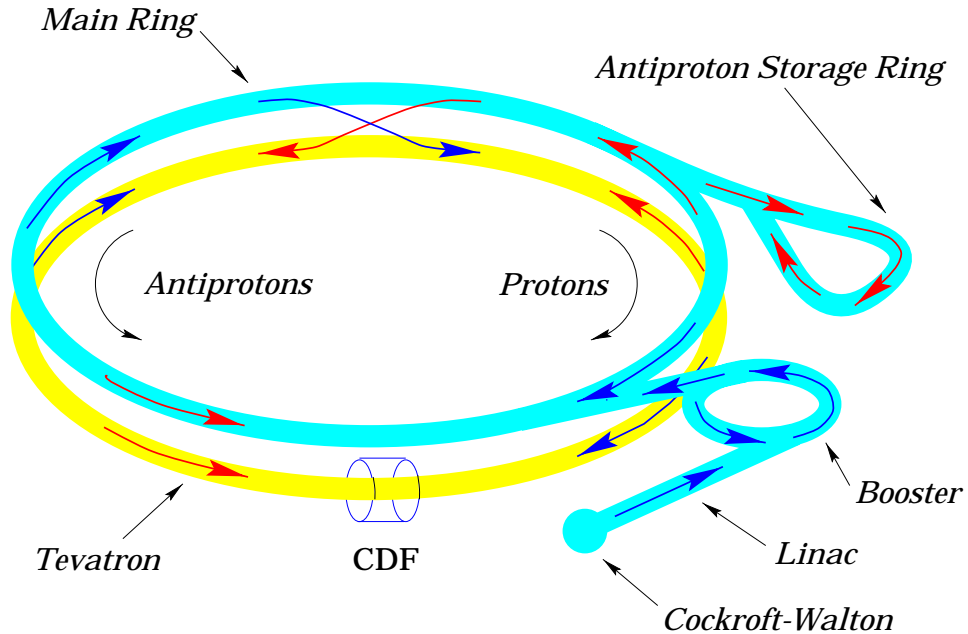


Figure 2.1: Fermilab's Run 1 particle accelerator (looking south).

## 2.2 CDF Detector

The CDF detector used for Run 1<sup>[34]</sup> consisted of a collection of charged-particle tracking chambers, sampling calorimeters, particle absorbers and muon detectors that were designed to cover a large fraction of the solid angle around the nominal interaction region. A description of the detector is presented here. See appendix A for explanation of the standard coordinates ( $x, y, z, r, \phi, \theta$  and  $\eta$ ) used to designate location within the detector. See appendix B for the definitions of some standard CDF kinematic variables ( $P_T$ ,  $E_T$  and  $\vec{\cancel{E}}_T$ ) that are frequently mentioned in this dissertation. General descriptions of basic detector elements discussed in this section (e.g. calorimeters, scintillators and drift chambers) can be found in references [35] and [36]. A cross-sectional view of one quadrant of the Run 1 CDF detector is shown in figure 2.2 (A similar diagram is shown in Appendix A).

### 2.2.1 Tracking Chambers

Concentric to the beam line and centered at  $z = 0$  was a super-conducting solenoid of length 4.8 m and radius 1.5 m that generated a 1.4-T magnetic field. It surrounded three tracking chambers that were used to detect charged particles and measure their momenta.



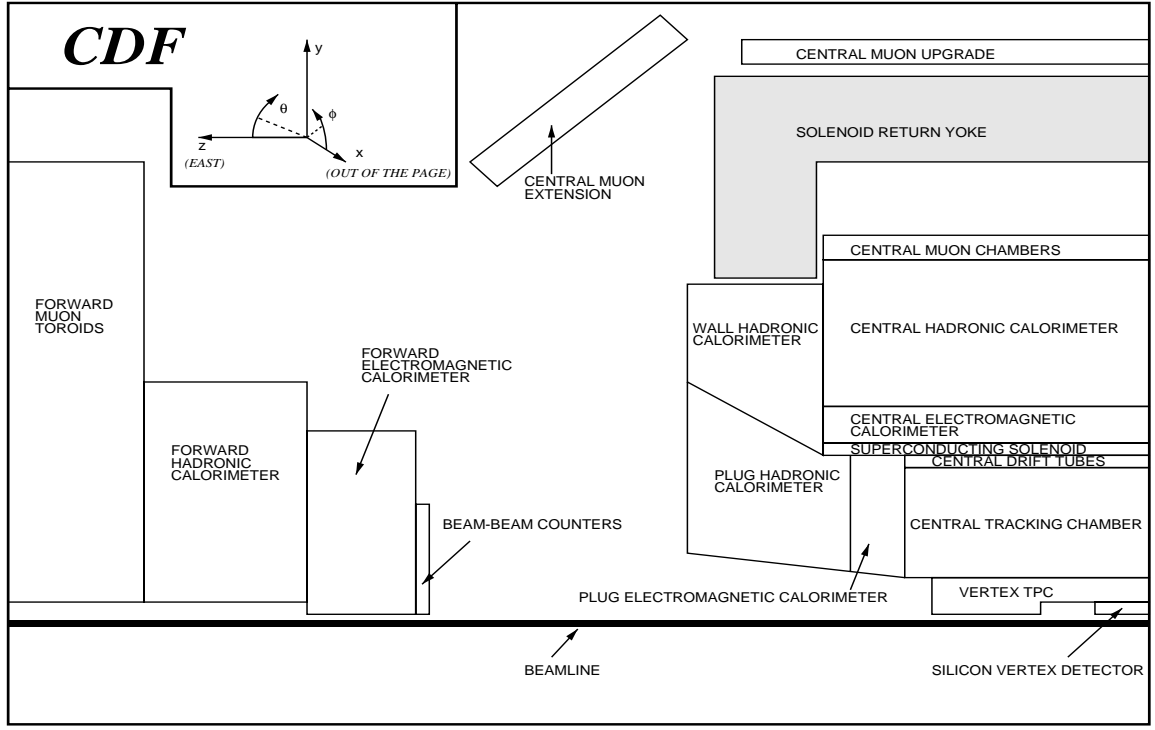


Figure 2.2: A cross-sectional view of one quadrant of the Run 1 CDF detector.

A 1.9 m long evacuated beryllium beampipe surrounded the beam line in the vicinity of the interaction region. Surrounding the beampipe was a four-layer silicon microstrip vertex detector (SVX). The SVX used for Run 1A is described in reference [37]. The SVX was 51 cm long and had a radius of 7.87 cm. Due to the spread of interactions along the beam line (see appendix A) the SVX geometrical acceptance was approximately 60%. The SVX was symmetric about  $z = 0$  and consisted of two identical cylindrical modules each of which were divided into four layers radially and 12 wedges azimuthally. Each radial layer of a given wedge consisted of three silicon microstrip detectors that were parallel to the beam line.  $60 \mu\text{m}$  pitch axial readout strips on the first three radial layers and  $55 \mu\text{m}$  pitch axial readout strips on the outermost radial layer provided precision track reconstruction in the plane transverse to the beam. Each wedge contained 15 readout chips and each readout chip was connected to 128 readout strips (channels) for a total of 46080 channels. According to Run 1A data measurements the SVX single-hit resolution was  $\sigma = 13 \mu\text{m}$  and the impact parameter resolution for high momentum particles was  $\sigma = 17 \mu\text{m}$ <sup>[16]</sup>. During

Run 1A, radiation damage to the readout chips caused a significant degradation of SVX performance. For example, on the innermost layer the average analogue pulse size from a particle divided by the noise level decreased from 9 to 6 over the course of the run <sup>[16]</sup>. Consequently, for Run 1B the SVX was replaced with an upgraded module<sup>[38]</sup> called the SVX'. The SVX' was very similar in design to the SVX, but with the following major improvements: (1) the silicon microstrips were AC coupled to reduce leakage current and noise, (2) the readout chips were made more resistant to radiation and (3) the radius of the innermost radial layer was reduced from 3.00 cm to 2.86 cm to increase the geometrical acceptance. For CDF top quark searches the SVX has provided precision secondary vertex information for the detection of long-lived particles like the bottom quark (see section 4.3). Figure 2.3 shows a schematic of an SVX module.

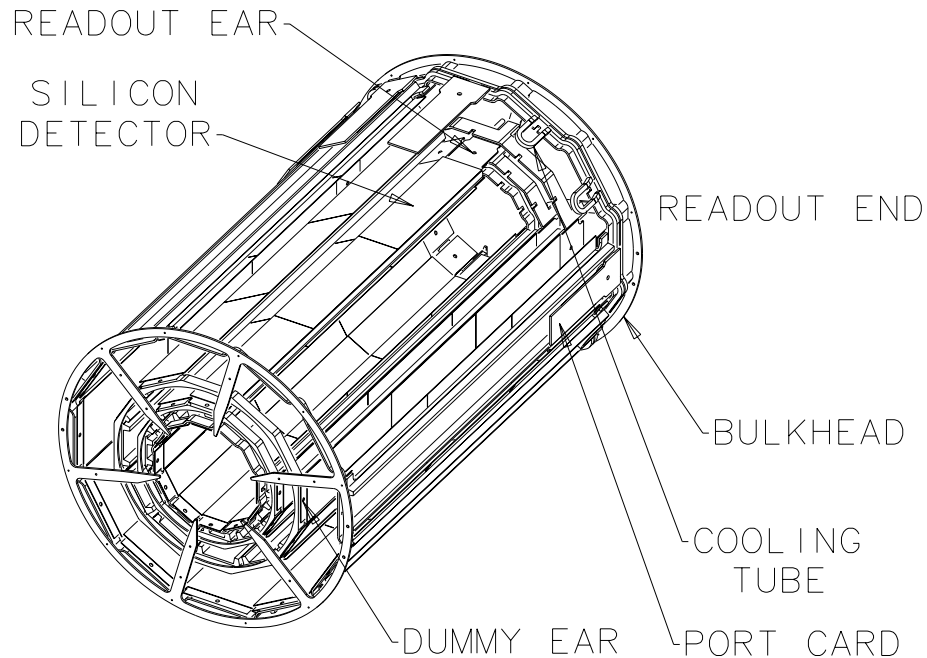


Figure 2.3: Schematic of an SVX module.

Surrounding the SVX was a vertex drift chamber (VTX)<sup>[39]</sup> which was intended to provide tracking information up to a radius of 22 cm in the pseudorapidity range  $|\eta| < 3.25$ . The VTX was segmented into 8 identical modules along the  $z$  direction. The endcaps of each module were divided azimuthally into 8 wedges. Each wedge contained wires that were perpendicular to both the beam line and the center line of the wedge. Wire position and drift times were used to obtain track information in the  $r - z$  view. Tracks that were reconstructed by the VTX were used to measure the  $p\bar{p}$  interaction vertex along the  $z$ -axis with a resolution of 1 mm.

The third tracking chamber layer was the central tracking chamber (CTC)<sup>[40]</sup> which was 3.2 m long and had an outer radius of 1.32 m. It consisted of 84 concentric cylindrical layers of sense wires that used charged-particle tracking to reconstruct the particle track and to determine its momentum. Information in the  $r - \phi$  plane was provided by 5 axial superlayers, each containing 12 layers of sense wires that were parallel to the beam direction. The  $r - z$  information was measured using 4 stereo superlayers, each containing 6 layers of sense wires that were tilted at  $\pm 3^\circ$  relative to the beam direction. The sense wire layers in each superlayer were segmented azimuthally into separate drift cells each containing a single line of sense wires. The cells were tilted at an angle of  $45^\circ$  with respect to the radial direction to compensate for the Lorentz angle of drift electrons caused by the crossing of the solenoidal magnetic field with the drift electric fields of the CTC. The transverse momentum resolution of the CTC was  $\delta P_T/P_T \approx 0.002$ , where  $P_T$  is in units of GeV/c. Combining both SVX and CTC information the transverse momentum resolution was  $\delta P_T/P_T \approx 0.001$ . Figure 2.4 shows a cross-sectional view of the CTC and its 12 layers of sense wires.

### 2.2.2 Calorimeters

The solenoid was surrounded by several layers of calorimetry, which covered the full azimuthal range and a pseudorapidity range of  $|\eta| < 4.2$ . The calorimeters were segmented into towers that projected out from the nominal interaction point ( $z = 0$ ) and whose geometry is most naturally described in terms of the coordinates  $(\phi, \eta)$ . The calorimeters were divided in  $\eta$  into three sections that are referred to as the central, plug and forward regions. Each region had an electromagnetic calorimeter layer followed by an hadronic calorimeter layer. The central region consisted of the

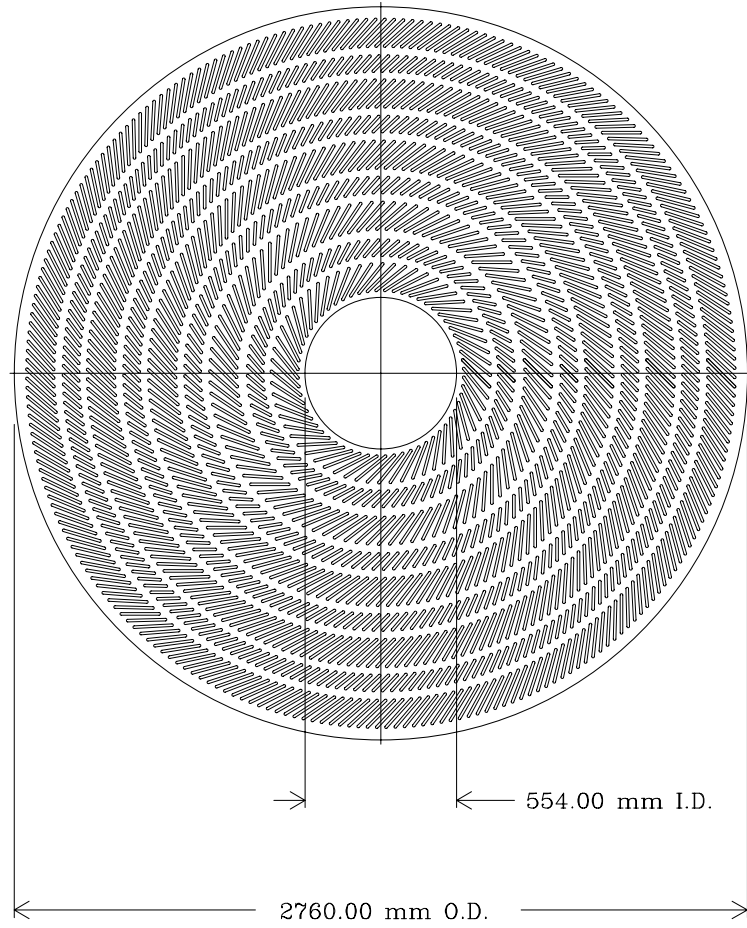


Figure 2.4: Cross-sectional view of the Central Tracking Chamber.

central electromagnetic calorimeter<sup>[41]</sup> (CEM) and a hadronic calorimeter<sup>[42]</sup> that was divided into two parts, the central hadronic calorimeter (CHA) and the wall hadronic calorimeter (WHA). Similarly, The plug and forward regions consisted of the calorimeters (PEM,PHA)<sup>[43]</sup> and (FEM,FHA)<sup>[44]</sup>, respectively. Table 2.1 shows the  $\eta$  range, energy resolution and thickness of the calorimetry components<sup>[16]</sup>. In this table  $X_0$  stands for "radiation length",  $\lambda_0$  stands for "interaction length" and the symbol,  $\oplus$ , implies addition in quadrature.

The central towers were  $15^\circ$  wide in  $\phi$  and 0.1 units wide in  $\eta$ . The CEM (CHA) used alternating layers of lead (steel) absorber and polystyrene (acrylic) scintillator

System	Range	Energy Resolution	Thickness
CEM	$ \eta  < 1.1$	$13.7\%/\sqrt{E_T} \oplus 2\%$	$18 X_0$
PEM	$1.1 <  \eta  < 2.4$	$22\%/\sqrt{E} \oplus 2\%$	$18 - 21 X_0$
FEM	$2.2 <  \eta  < 4.2$	$26\%/\sqrt{E} \oplus 2\%$	$25 X_0$
CHA	$ \eta  < 0.9$	$50\%/\sqrt{E_T} \oplus 3\%$	$4.5 \lambda_0$
WHA	$0.7 <  \eta  < 1.3$	$75\%/\sqrt{E} \oplus 4\%$	$4.5 \lambda_0$
PHA	$1.3 <  \eta  < 2.4$	$106\%/\sqrt{E} \oplus 6\%$	$5.7 \lambda_0$
FHA	$2.4 <  \eta  < 4.2$	$137\%/\sqrt{E} \oplus 3\%$	$7.7 \lambda_0$

Table 2.1: Properties of the calorimetry components used by the Run 1 CDF detector.

with phototube readout. Between the solenoid and the CEM there lay a set of proportional chambers referred to collectively as the central preradiator detector (CPR). The CPR provided  $r - \phi$  information on the early development of electromagnetic showers. In the CEM, at a radial distance of about six radiation lengths away from the CPR, lay a collection of proportional chambers with strip and wire readout called the central electromagnetic strip detector (CES)<sup>[41]</sup>. The CES was located at the approximate radial distance at which electromagnetic showers reach their maximum and it provided both  $z$  and  $r - \phi$  information about electromagnetic shower position.

The towers in the plug and forward regions were  $5^\circ$  wide in  $\phi$  and 0.1 units wide in  $\eta$ . The PEM and FEM (PHA and FHA) consisted of layers of lead (steel) absorber interspersed with gas proportional chambers that used cathode pad readout. For measuring electromagnetic shower position, the PEM used strips that gave  $\phi$  and  $\theta$  information. Figure 2.5 shows the  $\phi - \eta$  segmentation of 1 octant of the CDF calorimetry.

When measuring the event coordinates of an electron (hadronic jet) in the calorimeter the direction of the tower was taken to be a unit vector pointing from the event vertex to the point on the tower center line where electromagnetic (hadronic) shower maximum was calculated to occur.

### 2.2.3 Muon Detectors

Outside of the central hadronic calorimeter were four layers of drift chambers known collectively as the central muon detection system (CMU)<sup>[45]</sup>. The central calorimetry acted as a hadron absorber while allowing muons with  $P_T$  greater than 1.5 GeV/c to

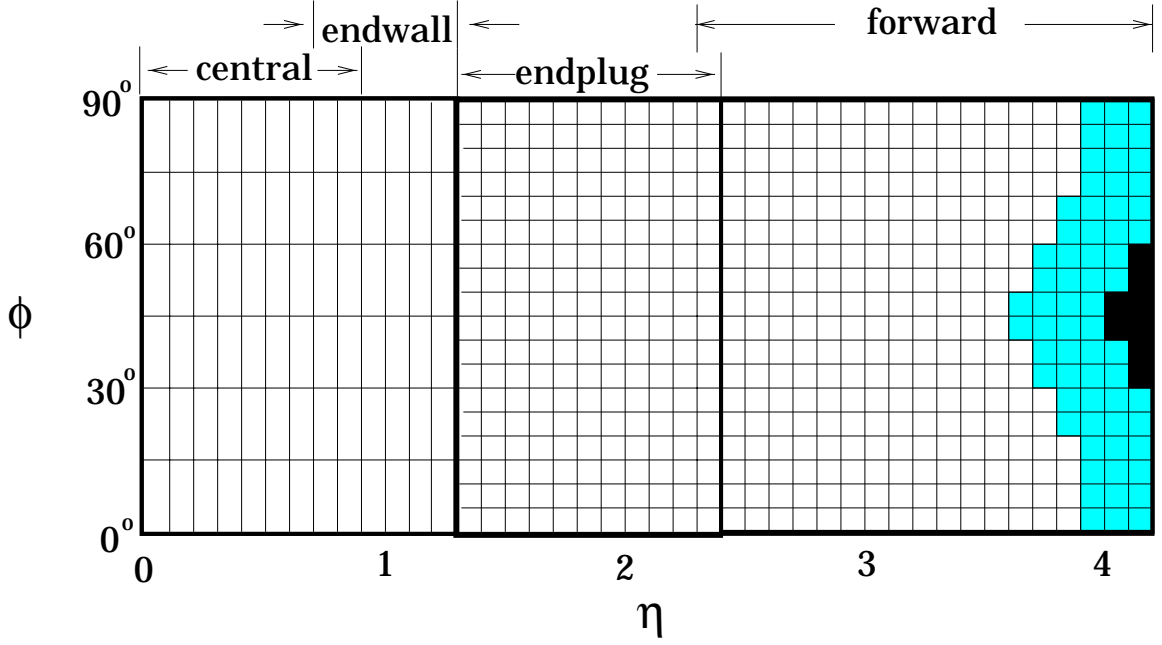


Figure 2.5: The  $\phi - \eta$  segmentation of 1 octant of the CDF calorimetry.

reach the CMU. Beyond the CMU was 0.6 m of hadron absorbing steel followed by four more layers of drift chambers to detect muons. This system was added in 1992 and is known as the central muon upgrade (CMP). In addition, two free-standing conical arches that contained drift chambers for muon detection and scintillators for triggering were placed on both ends of the CDF detector. This system is referred to as the central muon extension (CMX). Together, the CMU and the CMP covered approximately 84% of the solid angle for the region  $|\eta| < 0.6$ . The CMX covered approximately 71% of the solid angle for the region  $0.6 < |\eta| < 1.0$ .

A muon drift chamber layer consisted of several drift cells each of which contained a single axial sense wire that was parallel to the beam line. A track segment in the  $r - \phi$  view was formed by hits on a pair of axial sense wires, from two alternating layers, that intersected the same radial line emanating from the beam axis. To determine which side of the radial line the track segment lay the arrival times of drift electrons to these sense wires were compared to the times for the same drift electrons to arrive at a pair of sense wires, from the other two layers, that intersected a radial line that was slightly offset (by about 2 mm) from the original radial line. The resolution of track measurement in the  $r - \phi$  plane was about  $250 \mu\text{m}$ . Figure 2.6 shows a track

passing through the 4 layers of a muon drift chamber. The  $z$  position of a track segment was determined by comparing pulse heights at each end of sense wires that contained hits. The resolution in the  $z$  direction was 1.2 mm. By measuring the time for the drift electrons to reach the sense wires the azimuthal angle of deflection,  $\alpha$ , due to the solenoidal magnetic field in the CTC was measured. The value of  $\alpha$  was used to calculate the transverse momentum,  $P_T$ , of the muon track. High  $P_T$  particles had large radii of curvature in the CTC, which translated to small values for  $\alpha$ . The  $P_T$  information from the muon detectors was used for inclusive muon triggering (see section 2.3).

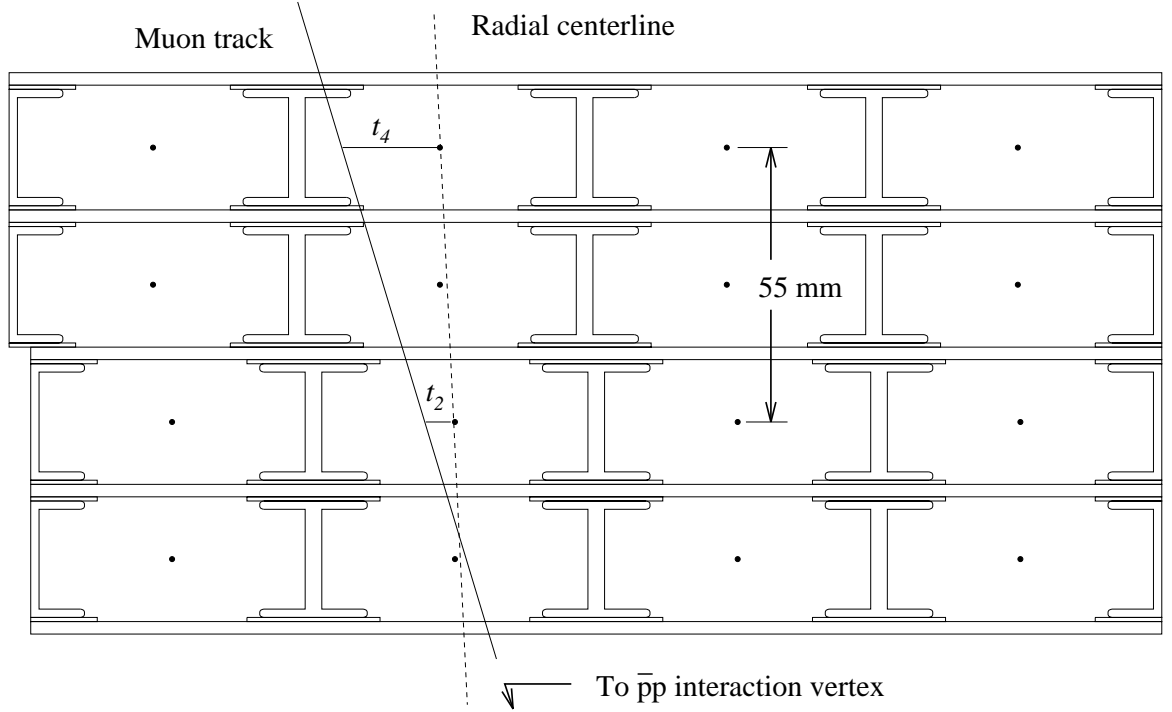


Figure 2.6: A track passing through the 4 layers of a muon drift chamber.

#### 2.2.4 Luminosity Measurement

To measure the luminosity at CDF a plane of scintillation counters with polar angular range  $0.32^\circ \leq \theta \leq 4.47^\circ$  was placed in front of the detector at a distance of 5.8 m from the nominal interaction point ( $z = 0$ ). A similar plane of counters with angular range  $175.53^\circ \leq \theta \leq 179.68^\circ$  was placed behind the detector at the same distance from the

interaction point. These two counters together were referred to as the beam-beam counters (BBC's)<sup>[34]</sup> and they covered the pseudorapidity range  $3.24 < |\eta| < 5.88$ . Whenever hits in both counters were no more than 15 ns apart a minimum-bias trigger was activated. The instantaneous luminosity,  $\mathcal{L}$ , was defined for CDF as the rate of such coincidences in the BBC's divided by the effective cross section of the counters. The effective BBC cross section was measured to be  $\sigma_{\text{BBC}} = 51.2 \pm 1.6$  mb. The average instantaneous luminosity for Run 1A (Run 1B) was  $0.54 \times 10^{31} \text{ cm}^{-2}\text{s}^{-1}$  ( $1.6 \times 10^{31} \text{ cm}^{-2}\text{s}^{-1}$ ) which corresponds to approximately 1 (3) interactions per bunch crossing. Accounting for possible background signals in the BBC's, a total uncertainty of 3.6% (8.0%) was placed on the integrated luminosity,  $\int \mathcal{L} dt$ , for Run 1A (Run 1B). The total integrated luminosity for Run 1 was  $109.4 \pm 7.2 \text{ pb}^{-1}$ <sup>[46]</sup>.

## 2.3 CDF Triggers

Before an event at CDF could be stored on tape for off-line analysis it was required to pass three successive on-line hardware trigger stages<sup>[47],[48]</sup>, commonly referred to as levels 1, 2 and 3. The triggers were designed to: (1) select the most promising events for a given analysis, (2) minimize the amount of events lost during a trigger decision (i.e. minimize dead time) and (3) reduce the final selection rate to a level acceptable for storing data on magnetic tape. The data that was implemented in the search for  $t\bar{t}$  events was collected using inclusive electron and muon triggers. For the purpose of triggering, the electromagnetic and hadronic calorimeter information was each grouped into towers that were  $15^\circ$  wide in  $\phi$  and 0.2 units wide in  $\eta$ . The trigger system made use of a fast two-dimensional hardware track finder, called the central fast tracker (CFT)<sup>[49]</sup>.

The level 1 inclusive electron trigger for Run 1B required a single calorimetry tower with energy above one of the following thresholds: 8 GeV in the CEM, 12 GeV in the CHA, 11 GeV in the PEM, 51 GeV in the PHA, 51 GeV in the FEM or 51 GeV in the FHA. The level 2 trigger system for electrons used energy cluster information from the electromagnetic calorimeters and two-dimensional CTC track information from the CFT. Energy clusters were formed in the CEM (PEM) by searching for seed towers with  $E_T > 9$  GeV (6 GeV) and adding to these seed towers all neighboring towers with  $E_T > 7$  GeV (4 GeV). The energy clusters were required to have an hadronic



to electromagnetic energy ratio ( $E_{\text{had}}/E_{\text{EM}}$ ) of less than 0.125. In the central region the level 2 trigger required an energy cluster in the CEM with total  $E_T > 9$  GeV to be matched with a CTC track with  $P_T > 9.2$  GeV/c as measured by the CFT. The level 2 trigger in the plug region required either an energy cluster in the PEM with  $E_T > 20$  GeV or an energy cluster in the PEM with  $E_T > 15$  GeV along with a missing transverse energy magnitude of  $|\vec{E}_T| > 15$  GeV.

The level 1 inclusive muon trigger<sup>[50]</sup> required one of the following: (1) a track segment in the CMU with  $P_T > 6$  GeV/c that could be associated with hits in the CMP, (2) a track segment in the CMU with  $P_T > 6$  GeV/c that was in coincidence with the hadron calorimeter TDC's or (3) a track segment in the CMX with  $P_T > 10$  GeV/c that was in coincidence with hits on scintillators placed on both sides of the CMX chambers. To prevent triggering on cosmic rays and other particles not associated with the primary interaction the CMX scintillator coincidence was also required to occur in a very narrow time window centered about the interaction time. The level 2 muon trigger required a CFT track in the  $r - \phi$  plane to be matched with a muon chamber track segment with  $P_T > 9.2 \text{ GeV/c}$  that passed the level 1 trigger.

The maximum event rate is equivalent to the bunch crossing rate, which for six proton and six antiproton bunches is approximately 280 kHz. The level 1 triggers reduced this rate to the order of a few kHz. Since the level 1 trigger decisions were made within the  $3.5 \mu\text{s}$  between bunch crossings they incurred no dead time. The level 2 triggers decreased the rate of acceptable events to the order of a few tens of Hz. The level 2 decisions were made within  $20 \mu\text{s}$  and contributed a dead time of the order of a few percent.

The third level of triggering involved an on-line computer farm of commercial processors. Events that passed the level 2 trigger were subjected to on-line software reconstruction algorithms that were written primarily in Fortran and run in an environment similar to that used for off-line analysis. Events selected by level 3 were stored on magnetic tape for off-line processing. For Run 1B The level 3 trigger that was implemented for CEM electrons required a reconstructed energy cluster with  $E_T > 18$  GeV and an associated reconstructed CTC track with  $P_T > 13$  GeV/c. For the dilepton data set some additional requirements were made for central electrons (see reference [46]). Plug electrons were required to have a reconstructed  $E_T > 20$

GeV. For muons the level 3 trigger required the existence of a CTC track with  $P_T > 18$  GeV/c whose extrapolation to the radius of the CMU (CMP,CMX) muon chamber was closer than 5 cm (10 cm) in  $r\Delta\phi$  to a track segment in the chamber. In addition, a minimum ionization requirement for the muon was applied by requiring that the muon track's energy contribution to the CHA be less than 6 GeV. For Run 1A (Run 1B) the level 3 triggers reduced the event acceptance rate to a manageable level of approximately 3-5 Hz (8 Hz).

# Chapter 3

## Jet Energy Corrections

A brief description of the standard CDF off-line jet reconstruction algorithm is presented. Then some standard jet energy corrections developed to account for both detector and physics effects are described. The chapter concludes with a description of some jet energy corrections designed specifically for dilepton  $t\bar{t}$  candidate events.

### 3.1 Jet Reconstruction Algorithm

The standard off-line jet reconstruction algorithm<sup>[51]</sup> used by CDF begins by forming preclusters consisting of contiguous towers with  $E_T > 1.0$  GeV, the highest  $E_T$  towers being near the center of each precluster. The preclusters are limited in size to  $105^\circ$  in  $\phi$  and 0.7 units in  $\eta$ . This corresponds to a maximum size of  $7 \times 7$  ( $21 \times 7$ ) towers in the central (plug and forward) regions. Clusters are formed by finding the  $E_T$  weighted centroids of the preclusters and forming cones in the  $\phi - \eta$  plane of fixed radius  $R = \sqrt{(\Delta\phi)^2 + (\Delta\eta)^2}$  around the centroids. All towers with  $E_T > 100$  MeV whose centroids are inside a given cone are included in the associated cluster. Then the  $E_T$  weighted centroids of these new clusters are calculated and the procedure continues until the tower assignment to all of the clusters remains constant. Further redistribution of towers is necessary to prevent overlap between clusters. Dijet event studies have shown that the optimal choice of cone size is in the range  $0.4 < R < 1.0$ . Presently, the most common choice of jet clustering cone size for most CDF analyses is  $R = 0.4$ . The top quark mass measurement described in this dissertation was repeated using a cone size of  $R = 0.7$ , without a dramatic change in results. Unless stated otherwise, a cone size of 0.4 will be implied for all results presented in this document.

### 3.2 Standard Jet Energy Corrections

The jet energies measured directly by the CDF calorimetry were incorrect<sup>[51]</sup> for several reasons which included: (1) non-linear calorimeter response to low momentum charged particles, (2) tracks of low momentum charged particles being deflected out-

side of the the jet clustering cone by the solenoidal magnetic field, (3) diminished calorimeter response in the non-fiducial regions of the detector, (4) excess energy from partons not associated with the hard scattering process ("underlying event" energy), (5) energy lost outside of the jet clustering cone ("out-of-cone" energy) due to jet fragmentation<sup>[52]</sup> and gluon radiation effects and (6) small amounts of energy deposited in the calorimeter by minimum ionizing particles like muons.

To correct for the non-linear response of the fiducial region of the central calorimeter ( $0.2 < |\eta| < 0.7$ ) a Monte Carlo program was used to generate pairs of partons in several bins of approximately flat  $P_T$  range. Additional programs then performed fragmentation (tuned with test beam data) on these partons, reconstructed the resulting dijets using the standard jet clustering algorithm and simulated the CDF detector measurement of these jets. For each event an "underlying event" was included and the dijet system was given a transverse momentum boost to simulate soft gluon radiation effects. Partons were associated with jets by comparing their directions. The  $P_T$  sum of all fragmentation daughter particles from a given parton that fell inside the cone of the parton's associated jet cluster was divided by the jet cluster's transverse momentum,  $P_T^{\text{Jet}}$ . For each bin the average value of this ratio,  $\langle P_T^{\text{Parton}}/P_T^{\text{Jet}} \rangle$ , was determined and the corrected jet energy,  $P_T^{\text{Parton}}$ , was calculated using:

$$P_T^{\text{Parton}} = \left\langle \frac{P_T^{\text{Parton}}}{P_T^{\text{Jet}}} \right\rangle \cdot P_T^{\text{Jet}} \quad (3.1)$$

A plot of  $P_T^{\text{Parton}}$  vs.  $P_T^{\text{Jet}}$  was made and from this curve a quadratic spline fit was used to determine the average corrected jet energy as a function of  $P_T^{\text{Jet}}$ . This correction for the non-linear response of the central calorimetry is referred to as the "absolute" jet energy correction<sup>[51],[53]</sup>.

Jet energies in the plug and forward regions and in the non-fiducial regions of the central calorimeter were corrected back to the fiducial region ( $0.2 < |\eta| < 0.7$ ) of the central calorimeter where the jet response was quite flat in  $\eta$  and well known in  $P_T$ . The jet energy scale's pseudorapidity dependence was determined in the range ( $-3.5 < \eta < 3.5$ ) by using a dijet data sample containing one jet in the fiducial central region (the "trigger" jet) and one jet outside of this region (the "probe" jet). Since the  $P_T$  of the dijet system was assumed to be zero the transverse momentum of the probe jet,  $P_T^{\text{Probe}}$ , was corrected to balance the transverse momentum of the trigger

jet,  $P_T^{\text{Trigger}}$ . For given values of  $\eta$  and  $P_T^{\text{Probe}}$  the scaling factor took the form:

$$\beta = \frac{P_T^{\text{Trigger}}}{P_T^{\text{Probe}}} \quad (3.2)$$

An average jet energy correction factor was determined by fitting the  $\beta$  dependence on  $\eta$  to a smooth curve and generating several such curves by varying  $P_T$ . Since this energy correction depends on the central calorimeter response it is referred to as the "relative" jet energy correction<sup>[53]</sup>.

Using minimum bias data and the known non-linear jet response of the central calorimeter an estimate of the excess energy due to underlying events was obtained. This energy was independent of  $P_T^{\text{Jet}}$  and was generally quite small compared to  $P_T^{\text{Jet}}$ . For a jet clustering cone size of 0.7 the average  $P_T$  from underlying events has been estimated<sup>[53]</sup> to be about 1 GeV/c.

A jet's out-of-cone energy loss,  $P_T^{\text{OOC}}$ , is defined simply as the  $P_T$  sum of all daughter particles of the jet's associated parton minus the  $P_T$  sum of those daughter particles inside of the jet's clustering cone. From the same dijet Monte Carlo data that was used to determine the absolute jet energy scale it was found that  $P_T^{\text{OOC}}$  varies slowly with  $P_T^{\text{Jet}}$  and has the form:

$$P_T^{\text{OOC}} = \alpha \left( 1 - \beta e^{-\gamma P_T^{\text{Jet}}} \right) \quad (3.3)$$

where the values of  $\alpha$ ,  $\beta$  and  $\gamma$  depend on the jet clustering cone size.  $P_T^{\text{OOC}}$  is generally quite small compared to  $P_T^{\text{Jet}}$  and its dependence on  $P_T^{\text{Jet}}$  is expected to vary for different jet production processes. Consequently, jet energies are not always corrected for  $P_T^{\text{OOC}}$  but rather its effects are included in the overall jet energy uncertainty after other corrections have been made<sup>[53]</sup>.

It has been estimated<sup>[16]</sup> that these jet energy corrections increase the measured jet energies by about 30%. The corrected jet energies are still uncertain by an estimated 10% due to detector effects and soft gluon radiation contributions<sup>[16],[54]</sup>. This estimate could be reduced by doing  $E_T$  balancing studies on di-jet events in which one jet's energy is fully contained in the fiducial central region where the jet energy scale is well understood<sup>[16]</sup>.

This jet energy correction package is commonly referred to as QDJSCO<sup>[55]</sup> by the CDF Collaboration. The latest version of QDJSCO was released in 1996 and is

also referred to as JTC96s. Unless otherwise stated, absolute, relative, underlying event and out-of-cone corrections have been applied to all jet kinematics used in this dissertation.

### 3.3 Jet Energy Corrections for Dilepton Events

Studies have shown<sup>[56]</sup> that the jet energy corrections of the QDJSCO package are insufficient when applied to  $t\bar{t}$  events. There are several reasons for this inadequacy: (1) QDJSCO does not correct for the energy carried by neutrinos from  $b$  quarks that decay semi-leptonically; (2) The QDJSCO corrections are too insensitive to the  $P_T$  spectrum of the jets at the parton level. The jet  $P_T$  spectrum used to derive the QDJSCO corrections was divided into 4 GeV/c bins. To maintain high statistics, roughly the same numbers of jets were included in each bin, thus ignoring the actual cross section for producing jets of a given  $P_T$ ; (3) The events used to derive the QDJSCO corrections were generated using an ISAJET<sup>[57]</sup> based jet fragmentation model, which differs significantly from the fragmentation model used by HERWIG<sup>[58]</sup>. For example, the underlying event  $P_T$  spectrum of ISAJET is noticeably larger than that of HERWIG; (4) QDJSCO corrections were determined from di-jet Monte Carlo events. This is notable because the jet multiplicity of  $t\bar{t}$  events is generally greater than two so that the effects of underlying events and jet cross-talk are greater for  $t\bar{t}$  events than for di-jet events; (5) The QDJSCO corrections have no dependence on top quark mass while studies show<sup>[59]</sup> that the discrepancy between jet energy and associated parton energy is clearly mass dependent.

Large samples of HERWIG dilepton events with QFL detector simulation<sup>[60],[61]</sup> were generated with input top quark masses of 140, 160, 170, 180, 200, 220 and 240 GeV/c<sup>2</sup> to determine an improved set of jet energy corrections specifically tailored to  $t\bar{t}$  events in the dilepton decay channel<sup>[59]</sup>. A jet clustering cone size of 0.4 was used and only events for which the  $b$  and  $\bar{b}$  quarks had energy greater than 5 GeV/c<sup>2</sup> were considered. The following procedure was applied for a given top quark mass:

1. Only events and jets that passed the standard CDF dilepton event selection cuts (see chapter 4) were used.
2. The  $b$  and  $\bar{b}$  quarks were matched to their associated jets. This was done by considering all jets within a distance of 0.4 in the  $\phi - \eta$  plane from the  $b$  (or  $\bar{b}$ ) quark.

The QDJSCO corrections were applied to all of these jets. The jet whose  $P_T$  was closest to that of the  $b$  (or  $\bar{b}$ ) quark was identified as that quark's associated jet.

3. The ratio  $R = P_T^H/P_T^Q$  was calculated, where  $P_T^H$  is the transverse momentum of the  $b$  quark and  $P_T^Q$  is the transverse momentum of its associated jet after being corrected by QDJSCO.

4. The spectrum of  $P_T^Q$  values was divided into bins of width 4 GeV/c and a histogram of  $R$  values was created for each bin.

5. A plot consisting of the mean value of  $R$  versus the central value of  $P_T^Q$  for each bin was constructed. A similar plot containing the root-mean-squared (R.M.S.) of  $R$  versus the central value of  $P_T^Q$  for each bin was also created.

6. The means and R.M.S.'s of the  $R$  values for each bin were used to perform a quadratic fit. The resulting curve represents the new jet energy corrections as a function of  $P_T$  for the given input top quark mass. A similar curve of the errors (R.M.S. values) on the new corrections as a function of  $P_T$  for the given top quark mass was also created.

7. This procedure was repeated for the entire generated range of input top quark masses to derive the dependence of the corrections on top quark mass.

8. Corrections were derived for four different types of  $b$  quark decay: (i) No semileptonic decay (generic  $b$  jets). (ii) Semi-leptonic decay into an electron and associated neutrinos. (iii) Semi-leptonic decay into a muon and associated neutrinos for which the muon  $P_T$  has been added back into the  $b$  jet  $P_T$ . (iv) Semi-leptonic decay into a muon for which the muon  $P_T$  has not been added back into the  $b$  jet  $P_T$ .

This set of corrections is commonly referred to as DLJSCO. A similar set of corrections was generated for lepton+jets  $t\bar{t}$  events (LLJSCO) and multi-jet (i.e. all-hadronic)  $t\bar{t}$  events (MJJSCO).

The DLJSCO corrections generally decrease with increasing  $P_T^Q$  for a given top quark mass. The functions used to fit the plots of average  $R$  and error on  $R$  as functions of  $P_T^Q$  are all of the form:  $Y = \exp(p1 + p2 \cdot P_T^Q) + p3$ . The fitted parameters ( $p1$ ,  $p2$  and  $p3$ ) for a top quark mass of 170 GeV/c<sup>2</sup> are shown in Table 3.1. The mean and R.M.S. values of  $R$  when histogrammed for the complete range of  $P_T$  are presented in table 3.2 for a top quark mass of 170 GeV/c<sup>2</sup>.

		generic	decay to $e$	decay to $\mu$ (with $\mu P_T$ )	decay to $\mu$ (no $\mu P_T$ )
mean	$p1$	0.1933	-0.0035	0.2956	0.3002
	$p2$	-0.04772	-0.02858	-0.03083	-0.02869
	$p3$	0.9119	0.9045	0.8845	0.9886
R.M.S.	$p1$	-0.2388	-0.4796	-0.7650	-0.7455
	$p2$	-0.05150	-0.04378	-0.04255	-0.02542
	$p3$	0.1511	0.1886	0.2326	0.2134

Table 3.1: Fitted DLJSCO parameters for a top quark mass of 170 GeV/c<sup>2</sup>.

		generic	decay to $e$	decay to $\mu$ (with $\mu P_T$ )	decay to $\mu$ (no $\mu P_T$ )
Mean of R		$1.020 \pm 0.002$	$1.103 \pm 0.004$	$1.066 \pm 0.005$	$1.311 \pm 0.006$
R.M.S. of R		0.262	0.302	0.324	0.416

Table 3.2: Mean and R.M.S. of  $R$  for a top quark mass of 170 GeV/c<sup>2</sup>.

The DLJSCO corrections were derived for several different top quark masses and then compared to those determined for a top quark mass of 170 GeV/c<sup>2</sup>. The corrections for masses of 160 and 180 GeV/c<sup>2</sup> are very close to those for 170 GeV/c<sup>2</sup>. The corrections generally increase with decreasing top quark mass. For example, for generic  $b$  jets the correction for a top quark mass of 140 GeV/c<sup>2</sup> is larger than the correction for a mass of 170 GeV/c<sup>2</sup> by 10% at a jet  $P_T$  of 30 GeV/c and by 3% at jet  $P_T$  greater than 70 GeV/c. Conversely, the correction for a top quark mass of 200 GeV/c<sup>2</sup> is smaller than that for a mass of 170 GeV/c<sup>2</sup> by 10% at a jet  $P_T$  of 35 GeV/c and by 4% for jet  $P_T$  above 70 GeV/c<sup>[59]</sup>. The correction coefficients ( $p1$ ,  $p2$  and  $p3$ ) were parameterized as a function of top quark mass using the form:  $A + B \cdot M_{top} + C \cdot M_{top}^2$ . The fitted parameters,  $A$ ,  $B$  and  $C$  are shown in table 3.3

The DLJSCO jet energy corrections were applied to all jets used in the top quark mass reconstruction analysis described by this dissertation. In constructing the likelihood function for the mass fitting technique (see chapter 5), the DLJSCO errors on the jet energy corrections were also utilized. The DLJSCO corrections were always applied after the QDJSCO corrections, as prescribed by reference [59].



			generic	decay to $e$	decay to $\mu$ (with $\mu P_T$ )	decay to $\mu$ (no $\mu P_T$ )
Mean	p1	A	2.5656	-1.5739	1.2473	1.1586
		B	-0.21134E-01	0.16639E-01	-0.13525E-01	-0.73227E-02
		C	0.41358E-04	-0.43525E-04	0.41447E-04	0.14023E-04
Mean	p2	A	-0.21592	-0.13455	-0.28122E-01	-0.93260E-01
		B	0.15291E-02	0.89153E-03	-0.47843E-04	0.48458E-03
		C	-0.31429E-05	-0.17451E-05	0.28538E-06	-0.68163E-06
Mean	p3	A	-0.25150	-0.16415	-0.62096	-0.52455
		B	0.11114E-02	0.15266E-02	0.36893E-02	0.52650E-02
		C	-0.81020E-06	-0.35517E-05	-0.49025E-05	-0.13000E-04
R.M.S.	p1	A	-0.69123	-3.0134	2.1430	-0.31307
		B	0.64655E-02	0.30507E-01	-0.29356E-01	-0.75232E-02
		C	-0.23219E-04	-0.88930E-04	0.71412E-04	0.27957E-04
R.M.S.	p2	A	-0.20864	-0.26122E-01	-0.39242	-0.29732E-01
		B	0.13328E-02	-0.51891E-03	0.32427E-02	-0.23425E-04
		C	-0.23149E-05	0.23952E-05	-0.69628E-05	0.47705E-06
R.M.S.	p3	A	0.28476E-01	-0.45316	0.25929	-0.59588
		B	0.16519E-02	0.76261E-02	0.35942E-03	0.91860E-02
		C	-0.56402E-05	-0.22374E-04	-0.31827E-05	-0.27349E-04

Table 3.3: Fitted parameters of mass dependent quadratic functions utilized by DLJSCO.

# Chapter 4

## Dilepton Event Selection

The standard kinematic cuts used by the CDF collaboration to extract dilepton event candidates from the Run 1 data sample are presented here. The efficiency of this procedure is quantified and the types of background events expected to remain after application of the cuts are discussed. The chapter concludes by summarizing the complete CDF Run 1 dilepton event sample along with its expected levels of background contributions.

### 4.1 Electron Selection Cuts

The standard CDF dilepton event search looks for electron-like objects in the central region ( $|\eta| \leq 1.0$ ) and in the parts of the plug region where both calorimeter and tracking information is available ( $1.20 < |\eta| < 1.35$ ). Detector location cuts<sup>[46]</sup> are applied to reject electrons that are close to calorimeter boundaries where energy measurements are unreliable. These fiducial cuts reduce the solid angle coverage for the central (plug) electrons by 16% (11%).

In searching for central electron candidates, energy clusters are formed in the CEM which consist of a seed tower with  $E_T > 3$  GeV and the two towers closest in pseudorapidity to the seed tower. A central electron candidate is required to have a CTC track extrapolating to one of these CEM clusters. Electron-like objects resulting from the conversion of photons into  $e^-e^+$  pairs before reaching the CTC are rejected. An electron is assumed to originate from such a conversion if it does not possess a matching VTX track or if there exists an electron CTC track of opposite sign such that (1) the two tracks are closely aligned in the  $r - z$  view ( $\Delta(\cot\theta) < 0.06$ ), (2) the closest approach of the two tracks in the  $r - \phi$  view is less than 0.3 cm and (3) the estimated radius of the conversion is less than 50 cm.

In addition to the cuts on fiducial region and photon conversion, cuts are made on the following kinematic variables to distinguish the central electrons from charged hadrons:

- (1)  $E_{\text{had}}/E_{\text{EM}}$ : The ratio of hadronic calorimeter energy to electromagnetic calorimeter energy.
- (2)  $E/P$ : The ratio of calorimeter energy to track momentum.
- (3)  $|\Delta x|$ : The distance in  $r - \phi$  between the position of the extrapolated track and the CES shower position.
- (4)  $|\Delta z|$ : The distance in  $z$  between the position of the extrapolated track and the CES shower position.
- (5)  $L_{\text{shr}}$ : A comparison of the lateral shower profile of the calorimeter cluster with that of test beam electrons. This variable is defined as:

$$L_{\text{shr}} = 0.14 \cdot \sum_i \frac{E_i^{\text{meas}} - E_i^{\text{pred}}}{\sqrt{0.14 \cdot E^2 + (\Delta E_i^{\text{pred}})^2}} \quad (4.1)$$

where the sum is over the towers in the electromagnetic cluster (excluding the seed tower),  $E_i^{\text{meas}}$  is the measured energy in tower  $i$ ,  $E_i^{\text{pred}}$  is the predicted energy (using test beam data) in tower  $i$ ,  $E$  is the total electromagnetic energy of the cluster and  $\Delta E_i^{\text{pred}}$  is the uncertainty in  $E_i^{\text{pred}}$ .

- (6)  $\chi^2_{\text{strip}}$ : A chi-squared comparison of the electron's CES shower profile in the strip view with those of test beam electrons.
- (7)  $z$ -vertex match: The distance in  $z$  between the electron's CTC track when extrapolated to the beam line and the nearest event vertex (i.e. the event vertex associated with the electron).
- (8)  $z$ -vertex location: The distance in  $z$  from the origin of the event vertex associated with the electron.
- (9)  $I_{\text{cal}}$ : The calorimeter isolation is defined as the  $E_T$  sum, excluding the electron  $E_T$ , in all calorimeter towers that fall inside a cone of radius  $R = \sqrt{(\Delta\phi)^2 + (\Delta\eta)^2} = 0.4$  centered on the electron cluster, divided by the electron cluster  $E_T$ .
- (10)  $I_{\text{trk}}$ : The track isolation is defined as the  $P_T$  sum of all CTC tracks, except that of the electron, that fall within a cone of radius  $R = 0.4$  centered on the electron's CTC track, divided by the  $P_T$  of the electron track.

PEM electron clusters are required to lie in a fiducial region of the detector. In addition, cuts are made on the following kinematical variables to discriminate against charged hadrons in the plug region.

- (1)  $E_{\text{had}}/E_{\text{EM}}$
- (2)  $f_{\text{VTX}}$ : The VTX occupancy is defined as the number of hits in the VTX that point to the PEM cluster divided by the number of hits predicted.
- (3)  $\chi^2_{\text{trans}}$ : A chi-squared comparison of the electron's transverse profile in the PEM with those of test beam electrons.
- (4)  $\chi^2_{\text{depth}}$ : A chi-squared comparison of the electron's depth profile in the PEM with those of test beam electrons.
- (5) Track Match: A PEM electron is required to have a CTC track that passes through at least 3 axial superlayers of the CTC.
- (6)  $I_{\text{cal}}$

The electron search employs both a "tight" and a "loose" set of selection cuts. Plug electrons are always considered loose in standard CDF analyses of Run 1 data. Table 4.1 shows the complete set of electron selection cuts for dilepton events. From a data sample of  $Z^0 \rightarrow e^-e^+$  events the selection efficiency for tight (loose) CEM electrons in the fiducial regions has been determined<sup>[16]</sup> to be  $82.0 \pm 1.0\%$  ( $89.0 \pm 1.0\%$ ). Similarly, the PEM electron selection efficiency is approximately  $85 \pm 3\%$ , excluding a 25.0% loss due to the isolation cut. It should be noted that plug electrons are no longer used in most CDF dilepton analyses, which results in only a 4% loss in dilepton event acceptance (see section 4.5). However, plug electrons were utilized for the analysis described by this dissertation.

## 4.2 Muon Selection Cuts

The dilepton search classifies muons into two categories: Central (CMUO) muons and Central minimum ionizing (CMIO) muons. A CMUO muon is required to have a track segment in the CMU, CMP or CMX that matches a track in the CTC. This limits the CMUO search to the detector region  $|\eta| \leq 1.0$ . CMIO muons are identified as those particles which do not have track segments in the muon chambers but which have a CTC track that is matched to a calorimeter cluster that is consistent with a minimum ionizing particle. This extends the muon search to the region  $|\eta| \leq 1.2$  and to non-fiducial regions of the central muon detection system. Since CMIO muons do not produce track segments in the muon chambers they were not used as triggers.

The following kinematical variables are used to distinguish muons from charged hadrons and cosmic rays:

Variable	Tight CEM cuts	Loose CEM cuts	PEM cuts
$E_{\text{had}}/E_{\text{EM}}$	$< 0.05$	$< 0.055 + 0.045 \cdot E/100$	$< 0.05$
$E/P$	$< 1.8$	$< 4.0$	-
$L_{\text{shr}}$	$< 0.2$	$< 0.2$	-
$ \Delta x $	$< 1.5 \text{ cm}$	$< 1.5 \text{ cm}$	-
$ \Delta z $	$< 3.0 \text{ cm}$	$< 3.0 \text{ cm}$	-
$\chi^2_{\text{strip}}$	$< 10.0$	-	-
$z\text{-vertex match}$	$< 5.0 \text{ cm}$	-	-
$z\text{-vertex location}$	$< 60.0 \text{ cm}$	$< 60.0 \text{ cm}$	-
$f_{\text{VTX}}$	-	-	$> 0.5$
$\chi^2_{\text{trans}}$	-	-	$< 3.0$
$\chi^2_{\text{depth}}$	-	-	$< 15.0$
$I_{\text{cal}}$	-	-	$< 0.1$
Track match	-	-	applied
Conversion cuts	applied	applied	-
Fiducial cuts	applied	applied	applied

Table 4.1: Electron selection requirements for the CDF dilepton event analysis.

- (1)  $E_{\text{EM}}$ : Electromagnetic calorimeter energy.
- (2)  $E_{\text{had}}$ : Hadronic calorimeter energy.
- (3)  $E_{\text{EM}} + E_{\text{had}}$  energy: Sum of the electromagnetic and hadronic calorimeter energies.
- (4) Impact Parameter: The closest approach of the extrapolated CTC track to the beam line.
- (5)  $z\text{-vertex match}$ .
- (6)  $z\text{-vertex location}$ .
- (7)  $|\Delta x_{\text{CMU}}|$ : Distance in  $r - \phi$  between the extrapolated track and the track segment in the CMU.
- (8)  $|\Delta x_{\text{CMP}}|$ : Distance in  $r - \phi$  between the extrapolated track and the track segment in the CMP.
- (9)  $|\Delta x_{\text{CMX}}|$ : Distance in  $r - \phi$  between the extrapolated track and the track segment in the CMX.
- (10)  $I_{\text{cal}}$
- (11)  $I_{\text{trk}}$
- (12) Superlayer number: The CTC track of a CMIO muon is required to pass through at least 6 superlayers. At least 3 of these tracks must be axial and at least 2 of them must be stereo.

As is done for the electrons, both "tight" and "loose" cuts are applied to the muons. CMIO muons are always considered "loose" in the standard analyses. Table 4.2 shows the complete set of muon selection cuts for dilepton events. Some additional fiducial cuts are necessary for the CMIO muons. When no isolation cuts are applied the selection efficiency has been determined to be  $93.0 \pm 1.0\%$  for both CMUO and CMIO muons<sup>[16]</sup>. The isolation cut decreases the selection efficiency for CMIO muons by about 18.0%.

Variable	Tight CMUO cuts	Loose CMUO cuts	CMIO cuts
$E_{\text{EM}}$	$< 2.0 \text{ GeV}$	$< 2.0 \text{ GeV}$	$< 2.0 \text{ GeV}$
$E_{\text{had}}$	$< 6.0 \text{ GeV}$	$< 6.0 \text{ GeV}$	$< 6.0 \text{ GeV}$
$E_{\text{EM}} + E_{\text{had}}$	$> 0.1 \text{ GeV}$	$> 0.1 \text{ GeV}$	$> 0.1 \text{ GeV}$
Impact Parameter	$< 0.3 \text{ cm}$	$< 0.3 \text{ cm}$	$< 0.3 \text{ cm}$
$z$ -vertex match	$< 5.0 \text{ cm}$	$< 5.0 \text{ cm}$	$< 5.0 \text{ cm}$
$z$ -vertex location	$< 60.0 \text{ cm}$	$< 60.0 \text{ cm}$	$< 60.0 \text{ cm}$
$ \Delta x_{\text{CMU}} $	$< 2.0 \text{ cm}$	$< 2.0 \text{ cm}$	$< 2.0 \text{ cm}$
$ \Delta x_{\text{CMP}} $	$< 5.0 \text{ cm}$	$< 5.0 \text{ cm}$	$< 5.0 \text{ cm}$
$ \Delta x_{\text{CMX}} $	$< 5.0 \text{ cm}$	$< 5.0 \text{ cm}$	$< 5.0 \text{ cm}$
$I_{\text{cal}}$	-	-	$< 0.1$
$I_{\text{trk}}$	-	-	$< 0.1$
Superlayer cut	-	-	applied
Fiducial cuts	-	-	applied

Table 4.2: Muon selection requirements for the CDF dilepton event analysis.

### 4.3 $b$ -Tagging Algorithms

Several algorithms have been developed by CDF to identify (tag)  $b$  quarks by exploiting their long lifetimes and expected decay signatures. These algorithms were originally developed for top quark searches in the lepton + jets decay channel where  $b$  quark identification is crucial for the separation of signal from backgrounds like  $W + jets$  production. Since the expected background from  $W + jets$  production is small for dilepton events,  $b$ -tagging is not a requirement for standard CDF dilepton event searches. However, it is of interest to apply the  $b$ -tagging algorithms to the dilepton event candidates as a further verification that they represent the expected signal.

The  $b$ -tagging algorithms are divided into two basic categories: the SVX-tag routines and the soft lepton tag (SLT) routines. The SVX taggers utilize secondary vertex information collected by the SVX (see section 2.2.1) to search for jets resulting from  $b$  quark fragmentation. For Run 1A data three different SVX  $b$ -tagging techniques were applied: the jet-vertexing algorithm (JETVTX)<sup>[62]</sup>, the jet-probability algorithm (JPBTAG)<sup>[63]</sup> and the  $d - \phi$ <sup>[64]</sup> algorithm. While all three methods were used to test each other, JETVTX was the algorithm of choice for most Run 1A analyses. For Run 1B analyses a more efficient SVX-tagger called the seed-vertexing (SECVTX)<sup>[65]</sup> algorithm was developed to replace JETVTX. The SLT algorithms search for  $b$  quarks that decay semi-leptonically ( $b \rightarrow l \nu_l X$ ) or through cascade decays ( $b \rightarrow c \rightarrow l \nu_l X$ ), where  $l$  is either an electron or a muon. The leptons from these decays are considered soft because they are generally closely aligned with the  $b$  jet and have much lower  $E_T$  than the lepton candidates from  $W$  boson decay. This section will give a brief description of the SECVTX and SLT  $b$ -tagging methods.

An important kinematical quantity used by the SECVTX algorithm is the impact parameter significance,  $d/\sigma_d$ , where  $d$  is a track's impact parameter and  $\sigma_d$  is the uncertainty in  $d$ . For a positively charged particle, a positive sign (negative sign) is assigned to the particle's impact parameter if the beam line lies outside (inside) of the circle which describes the particle's trajectory in the  $x - y$  plane. This sign convention is reversed for negatively charged particles. The absolute impact parameter significance,  $|d|/\sigma_d$ , tends to be large for long-lived particles, like the  $b$  quark. Another relevant quantity is  $L_{xy}$ , the decay distance in the  $x - y$  plane of a candidate  $b$  quark. The sign of  $L_{xy}$  is defined as the sign of the vector dot product of a unit vector pointing from the primary vertex to the secondary vertex and the vector sum of the momenta of all tracks associated with the  $b$  quark decay. Long-lived particles are expected to have positive  $L_{xy}$  and large absolute decay distance significance,  $|L_{xy}|/\sigma_{L_{xy}}$ , where  $\sigma_{L_{xy}}$  is the error in  $L_{xy}$ . Figure 4.1 shows a diagram of a secondary vertex with its decay distance and impact parameter clearly designated. A fake secondary vertex, which contributes to  $b$ -tag background, is also shown in the figure.

For a given event, the SECVTX algorithm is applied to all jets that lie in the region  $|\eta| < 2$  and have uncorrected  $E_T > 15$  GeV. For a given  $b$  jet candidate the algorithm is executed in two passes. In the first pass the following "loose" selection

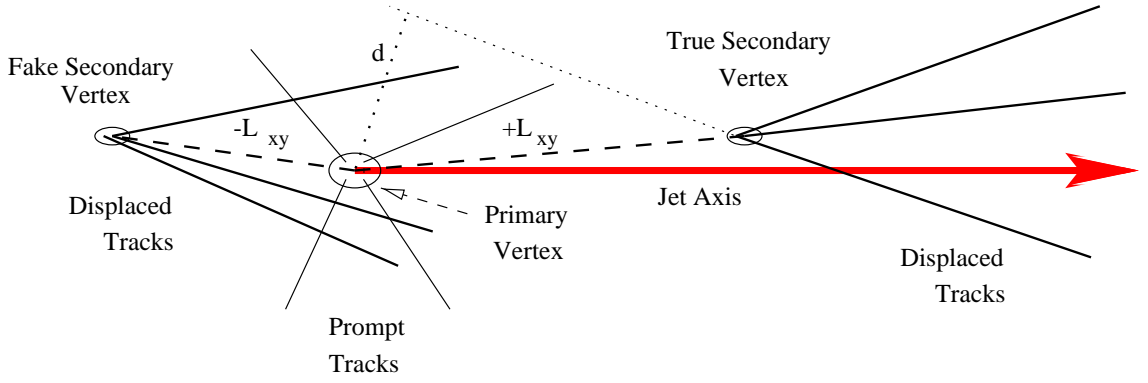


Figure 4.1: Schematic of a secondary vertex from  $b$  quark decay.

cuts are applied to all CTC tracks that lie inside a  $\phi - \eta$  cone of radius 0.4 about the jet: tracks must have  $|d|/\sigma_d > 2.5$  and hits in at least 2 layers of the SVX; tracks with 3 or 4 SVX hits must have  $P_T > 0.5$  GeV/c and be matched to at least one good SVX cluster, where, by definition, a good cluster is associated with only one CTC track and occupies no more than 3 silicon strips; tracks with 2 SVX hits must have  $P_T > 1.5$  GeV/c, have both clusters defined as good and have their hits in either the inner two or the outer two SVX layers. The tracks that pass these cuts are grouped into a hierarchy of four classes. All tracks in classes 1 and 2 have at least 2 good SVX clusters but the tracks of class 1 have  $P_T > 2$  GeV/c while the tracks of class 2 have  $P_T \leq 2$  GeV/c. For  $|d|/\sigma_d < 10.0$  ( $|d|/\sigma_d \geq 10$ ) the tracks in classes 1 and 2 are ranked by  $|d|/\sigma_d$  (number of good SVX clusters). The tracks in classes 3 and 4 are only required to have 1 good SVX cluster and are ranked by  $|d|/\sigma_d$ . Class 3 tracks have  $P_T > 2$  GeV/c and class 4 tracks have  $P_T \leq 2$  GeV/c. The two best tracks in the class hierarchy are constrained to a single vertex called the seed vertex. The seed vertex must always contain at least one track with  $P_T > 2$  GeV/c. The remaining tracks are examined and whenever one of them is found to have an absolute impact parameter significance relative to the seed vertex of more than 3 the track is associated with the vertex. After all tracks have been tested the algorithm is terminated if 1 or more tracks have been added to the seed vertex. Otherwise, a new seed vertex is formed from the next highest ranked pair of tracks and the search for a secondary vertex candidate with 3 or more associated tracks continues. If no such secondary vertex has been found after all pairs of tracks have been used, then



the algorithm attempts a second pass that searches for a secondary vertex candidate that is associated with 2 or more tracks that must pass a tighter set of selection cuts than those used in the first pass of the algorithm.

In the default version ("option 3")<sup>[66]</sup> of the SECVTX algorithm used for Run 1B analyses the "tight" cuts used for the second pass are as follows: Tracks must have  $P_T > 1.5$  GeV/c,  $|d|/\sigma_d > 3.0$  and at least 3 SVX hits; Tracks with 4 SVX hits must have at least one good cluster; Tracks with 3 SVX hits must have at least two good clusters. All tracks that pass these cuts are constrained to a single secondary vertex candidate and if any track contributes a  $\chi^2 > 50$  to this vertex fit then that track is discarded, a new fit is performed with the remaining tracks and the procedure continues until no more tracks are rejected. If no secondary vertex candidate with at least two tracks, at least one of which has  $P_T > 2$  GeV/c, is found in the second pass then the jet is rejected and the algorithm is applied to the next jet. (Note: The second pass of the SECVTX algorithm is very similar to the JETVTX algorithm). If a secondary vertex candidate is found in either pass then  $L_{xy}$  and  $\sigma_{L_{xy}}$  are calculated from the vertex fit and if  $|L_{xy}|/\sigma_{L_{xy}} > 3.0$  and  $|L_{xy}| < 2.5$  cm then the secondary vertex candidate is classified as a  $b$ -tag.

The SLT algorithm starts with inclusive electron and muon data sets that contain no implicit isolation cuts and whose  $P_T$  thresholds are much lower ( $P_T > 2$  GeV/c) than those in the inclusive lepton samples used for the detection of leptons from  $W$  boson decay (see section 2.3). The soft electron search<sup>[67]</sup> uses information from the CPR, CTC and CES. For a given event, all CTC tracks are subjected to cuts on the number of axial and stereo superlayers, impact parameter,  $E_{\text{had}}/E_{\text{EM}}$ ,  $E/P$  and photon conversion. Tracks that survive these cuts are required to be in the fiducial regions of both the CES and the CPR. Their extrapolations to the CES must be closely matched to CES clusters whose shape and energy deposition is consistent with electrons. Track extrapolations to the CPR must match to energy depositions in the CPR that correspond to at least four minimum-ionizing particles. Finally, a track's ionization loss in the CTC must be consistent with that of an electron.

The soft muon search<sup>[68]</sup> looks for CTC tracks that are matched to reconstructed tracks in the CMU and the CMP. CTC tracks with  $P_T > 3$  GeV/c that are in the combined CMU and CMP fiducial volume are required to be closely matched to track

segments in both chambers. Since muons with  $P_T < 3$  GeV/c are generally absorbed by the layers of steel preceding the CMP, CTC tracks with  $2 < P_T < 3$  GeV/c are only required to match with tracks in the CMU, but with tighter cuts. Since soft muons are expected to be non-isolated, no minimum ionizing cuts are placed on their calorimeter energy. Hadrons that are energetic enough to reach the CMU (hadronic punch through) are rejected in the combined CMU and CMP fiducial region by the requirement of CTC track matching to tracks in both chambers. In the region not covered by the CMP, muon candidates with  $P_T > 6$  GeV/c are rejected if their hadronic calorimeter energy deposition is greater than  $6 \text{ GeV} + \sum p$ , where  $\sum p$  is the scalar sum of the momenta of all tracks within a cone of 0.2 about the muon candidate. For Run 1B, CMX muons were added to the SLT search.

Monte Carlo simulations of  $t\bar{t}$  events were generated to determine the efficiency for tagging  $b$  quarks with the SVX-tagger for various masses of the top quark<sup>[66]</sup>. To get the actual efficiencies the Monte Carlo efficiencies had to be multiplied by a scale factor that was determined by comparing the  $b$ -tagging efficiency of an inclusive electron data sample enriched in  $b\bar{b}$  events with that of a Monte Carlo simulation of semi-leptonic  $b$  decays. The scale factor for Run 1B data was  $(95 \pm 5)\%$ . For  $60 \text{ pb}^{-1}$  of data the SVX  $b$ -tagging efficiency was determined to be  $42 \pm 0.05\%$  for  $\geq 3$  jet  $t\bar{t}$  events in a top quark mass range from  $140 \text{ GeV}/c^2$  to  $180 \text{ GeV}/c^2$ . The acceptance for tagging soft leptons in top events was also determined by using Monte Carlo events with CDF detector simulation. The efficiency for detecting an additional electron or muon in  $t\bar{t}$  events with  $\geq 3$  jets was determined to be  $20 \pm 2\%$ <sup>[19]</sup>. Although these  $b$ -tagging efficiencies for the SVX and SLT algorithms were generated for  $\geq 3$  jet  $t\bar{t}$  events they are not expected to differ appreciably for  $\geq 2$  jet  $t\bar{t}$  events since both types of events contain exactly two  $b$  quarks.

## 4.4 Event Selection Cuts

Dilepton  $t\bar{t}$  events are produced by the process (see section 1.2.1):

$$p\bar{p} \rightarrow t\bar{t} + X \rightarrow W^+ b W^- \bar{b} + X \rightarrow l^+ \nu b l^- \bar{\nu} \bar{b} + X$$

As mentioned in section 1.2.1, events in which one or both of the  $W$  bosons decay into  $\tau$  leptons and associated neutrinos are not included in standard CDF dilepton event searches because of the short lifetime of  $\tau$  leptons. An example of a dilepton event analysis that does make use of  $\tau$  leptons can be found in reference [69].

The dominant types of background to the dilepton event signal are:

- (1)  $W^+W^-$  production, where the  $W^+$  and the  $W^-$  bosons decay leptonically.
- (2) Drell-Yan production, which involves the production of photon or a  $Z^0$  boson with the subsequent decay:  $\gamma, Z^0 \rightarrow e^+e^-, \mu^+\mu^-$ .
- (3)  $Z^0 \rightarrow \tau^+\tau^-$ , where the  $\tau^+$  and  $\tau^-$  leptons decay into electrons or muons, along with associated neutrinos.
- (4)  $b\bar{b}$  production, where the  $b$  and  $\bar{b}$  quarks decay leptonically.
- (5) Lepton misidentification; This involves QCD multijet or  $W + jets$  processes that imitate the  $t\bar{t}$  final state because at least one jet is mistakenly identified as a lepton candidate. These backgrounds are referred to as "fake" dilepton backgrounds.

The five types of background events mentioned here, along with a few other less dominant types, will be described in detail in section 4.6.

To identify dilepton events with good efficiency while significantly reducing backgrounds the following cuts are applied:

- (1) At least two leptons that pass the electron or muon selection cuts listed in sections 4.1 and 4.2 are required. Backgrounds from  $b\bar{b}$  production,  $Z^0 \rightarrow \tau^+\tau^-$  decays and lepton misidentification are efficiently reduced by requiring that each of the two lepton candidates has  $P_T > 20$  GeV/c. To further reduce backgrounds from lepton misidentification and  $b\bar{b}$  production the two lepton candidates must be oppositely charged. In addition, at least one lepton candidate must be "tight" and both the calorimeter isolation and the track isolation of this lepton must be less than 0.1. To reduce  $Z^0$  boson decay backgrounds,  $e^+e^-$  and  $\mu^+\mu^-$  candidate events are rejected if they have a dilepton invariant mass in the range  $75 < M_{l+l^-} < 105$  GeV/c<sup>2</sup>. Algorithms are also applied to remove events with cosmic rays faking muon candidates.
- (2) Missing transverse energy is corrected for both jets and muons (see appendix B). To reduce backgrounds from Drell-Yan events,  $Z^0 \rightarrow \tau^+\tau^-$ ,  $b\bar{b}$  and lepton misidentification the magnitude of the missing transverse energy,  $|\vec{E}_T|$ , is required to be greater than 25 GeV. If  $25 < |\vec{E}_T| < 50$  GeV then a cut is also made on the direction of  $\vec{E}_T$ . Specifically, the azimuthal angle between  $\vec{E}_T$  and the nearest candidate jet is required to be greater than 20°. This cut is designed to reduce high  $\vec{E}_T$  Drell-Yan background, for which jet energy mismeasurement often leads to a  $\vec{E}_T$  that is nearly aligned with the jet itself<sup>[16]</sup>. Similarly the azimuthal angle between  $\vec{E}_T$  and the nearest lepton candidate is required to be greater than 20°. This reduces  $Z^0 \rightarrow \tau^+\tau^-$  backgrounds

for which one of the  $\tau$  leptons decays leptonically into a lepton candidate and two energetic neutrinos.

(3) Since the  $b$  and  $\bar{b}$  quarks stemming from  $t\bar{t}$  decay can be quite energetic for top quark masses exceeding  $120 \text{ GeV}/c^2$ , at least two jets with uncorrected  $E_T > 10 \text{ GeV}$  are required. These jet candidates are restricted to the region  $|\eta| < 2.0$  and must not be closely aligned with any lepton candidate. To further reduce backgrounds from higher order jet processes the  $b$ -tagging algorithms can be applied to the candidate jets.

## 4.5 Event Selection Efficiencies

The fraction of  $t\bar{t}$  events that pass all of the dilepton event selection cuts is referred to as the absolute top acceptance in the dilepton channel,  $\epsilon_{dil}$ . The largest contribution ( $\approx 86\%$ ) to  $\epsilon_{dil}$  comes from the desired signal, where the  $W^\pm$  bosons from a  $t\bar{t}$  pair each decay into an electron or muon and associated neutrinos<sup>[70]</sup>. However,  $\epsilon_{dil}$  contains a contribution ( $\approx 11\%$ ) from  $t\bar{t}$  events for which one of the  $W$  bosons decays into a  $\tau$  lepton which itself decays into an electron or a muon, and a contribution ( $\approx 3\%$ ) from lepton+jets events for which one of the  $b$  quarks decays into a high  $P_T$  electron or muon. Although  $\epsilon_{dil}$  can also contain contributions from  $t\bar{t}$  events where both  $W$  bosons decay into  $\tau$  leptons or where both  $b$  quarks decay into high  $P_T$  electrons or muons these effects are negligible due to the efficiency of the lepton identification cuts of sections 4.1 and 4.2. The dilepton top acceptance is needed to determine the  $t\bar{t}$  production cross-section,  $\sigma_{t\bar{t}}$ , via the equation:

$$\sigma_{t\bar{t}} = \frac{N_{dil}}{\epsilon_{dil} \int \mathcal{L} dt} \quad (4.2)$$

where  $N_{dil}$  is the number of experimentally observed dilepton events and  $\int \mathcal{L} dt$  is the integrated luminosity of the total CDF Run 1 data sample. To determine  $\epsilon_{dil}$  as a function of top quark mass large Monte Carlo samples, typically with  $\sim 80,000$  events per mass, were generated using QFL detector simulation. This section describes the calculation of  $\epsilon_{dil}$ .

The top acceptance in the dilepton channel may be expressed as the product of several efficiencies:  $\epsilon_{dil} = \epsilon_{\text{geom} \cdot P_T} \cdot \epsilon_{\text{trigger}} \cdot \epsilon_{\text{ID}} \cdot \epsilon_{\text{SS}} \cdot \epsilon_{\text{iso}} \cdot \epsilon_{\text{mass}} \cdot \epsilon_{\cancel{E}_T} \cdot \epsilon_{2\text{-jet}}$ . Each efficiency is described below:

- (1)  $\epsilon_{\text{geom}\cdot\text{P}_T}$ : The geometric and kinematical acceptance in the dilepton channel is defined as the ratio of dilepton events to total number of  $t\bar{t}$  events, for which both lepton candidates (i) are in the fiducial region of the detector, (ii) have  $E_T > 20$  GeV ( $P_T > 20$  GeV/c) if they are electrons (muons), (iii) have good CTC tracks, (iv) are not associated with photon conversions and (v) lie within a cone of 0.4 of the generator level leptons to which they are matched.  $\epsilon_{\text{geom}\cdot\text{P}_T}$  is determined by finding the fraction of all generated  $t\bar{t}$  events that pass these cuts and then multiplying this number by the branching ratio,  $\frac{4}{81}$ , for the  $t\bar{t}$  system to decay via the dilepton channel.
- (2)  $\epsilon_{\text{trigger}}$ : The trigger efficiency is the fraction of dilepton events passing the geometrical and kinematical cuts whose lepton candidates pass the trigger cuts described in section 2.3. This efficiency is independent of top quark mass and is almost 100% efficient for inclusive electrons and 94% efficient for inclusive muons.
- (3)  $\epsilon_{\text{ID}}$ : The lepton identification efficiency is the fraction of dilepton events passing the geometric, kinematical and trigger cuts that also pass all of the cuts presented in sections 4.1 and 4.2 except the cuts on fiduciality, track quality and photon conversion, which are covered by  $\epsilon_{\text{geom}\cdot\text{P}_T}$ , and the isolation cuts, which are covered by  $\epsilon_{\text{iso}}$  (defined below). Plug electrons are not included in the Run 1B calculation of  $\epsilon_{\text{ID}}$  but this only amounts to a 4% loss in  $\epsilon_{\text{dil}}$ .
- (4)  $\epsilon_{\text{SS}}$ : The same sign efficiency is the fraction of dilepton events passing the geometric, kinematical, trigger and lepton identification cuts which also satisfy the requirement that the electric charges of the lepton candidates be opposite in sign.
- (5)  $\epsilon_{\text{iso}}$ : The isolation efficiency is the fraction of dilepton events passing the geometric, kinematical, trigger, lepton identification and same sign cuts that also satisfy the isolation cuts described in section 4.4.
- (6)  $\epsilon_{\text{mass}}$ : The  $Z^0$  mass efficiency is the fraction of dilepton events passing the geometric, kinematical, trigger, lepton identification, same sign and isolation cuts that also pass the  $Z^0$  boson mass window cut presented in section 4.4.
- (7)  $\epsilon_{\cancel{E}_T}$ : The missing  $E_T$  efficiency is the fraction of dilepton events passing the geometric, kinematical, trigger, lepton identification, same sign, isolation and  $Z^0$  mass cuts that also pass the missing transverse energy cuts described in section 4.4.
- (8)  $\epsilon_{2\text{-jet}}$ : The 2-jet efficiency is the fraction of dilepton events passing the geometric, kinematical, trigger, lepton identification, same sign, isolation,  $Z^0$  mass and missing  $E_T$  cuts that also contain two jets that pass the jet cuts described in section 4.4.

Unfortunately, the detector simulation does not model every lepton identification variable realistically enough for  $\epsilon_{\text{ID}}$  to represent the true fraction of dilepton events passing the geometric, kinematical and trigger cuts that also pass the lepton identification cuts. To correct for this discrepancy, the lepton identification efficiencies for a Run 1B data sample of  $Z^0 \rightarrow ll$  events with dilepton invariant mass,  $M_{l+l-}$ , in the range  $80 < M_{l+l-} < 100 \text{ GeV}/c^2$  were compared to a sample of Monte Carlo  $Z^0 \rightarrow ll$  events that pass the geometric and kinematical cuts. These efficiencies were calculated separately for the different lepton types (tight central electron, CMIO muon, etc.). Simply using the ratio of  $Z^0$  data efficiency to  $Z^0$  Monte Carlo efficiency was not sufficient to correct  $\epsilon_{\text{ID}}$  because the amount of jet activity in  $t\bar{t}$  events and  $Z^0$  events is different and higher jet activity implies less isolated leptons which implies lower efficiency. To correct for this effect each lepton candidate in the  $t\bar{t}$  Monte Carlo sample was assigned a scale factor that depended on both its type and its isolation. If an event passed all of the dilepton event selection cuts then it was assigned a weight consisting of the product of the two scale factors for the event. Finally,  $\epsilon_{\text{ID}}$  was calculated as the weighted number of events divided by the unweighted number of events that pass all of the dilepton event selection cuts.

Table 4.3<sup>[71]</sup> shows the dependences of the dilepton event selection cut efficiencies and the total dilepton acceptance on top quark mass, as determined by PYTHIA<sup>[72]</sup> V\_5.6 Monte Carlo samples. The efficiencies are defined so that each efficiency in the table is calculated from the events that pass the cuts to the left of it. The only cut efficiencies that change significantly with top quark mass are  $\epsilon_{\text{geom} \cdot P_T}$ ,  $\epsilon_{2\text{-jet}}$  and  $\epsilon_{\text{ID}}$ . As top quark mass increases more energy is available to the leptons so that they can have higher  $P_T$  and be found in the central region with greater frequency. Therefore,  $\epsilon_{\text{geom} \cdot P_T}$  increases with increasing top quark mass. Similarly  $\epsilon_{2\text{-jet}}$  increases with increasing top quark mass since more energy becomes available to the jets. Larger top quark mass also implies a higher rate of leptons stemming from  $b$  quark decay with sufficient energy to pass the geometric and kinematical cuts. However, the other daughter particles from  $b$  quark decay will become more energetic too so that less of the leptons from  $b$  quark decay will pass cuts on variables (e.g.  $E_{\text{had}}/E_{\text{EM}}$ ) designed to distinguish leptons from hadrons. This explains why  $\epsilon_{\text{ID}}$  actually decreases with increasing top quark mass. The total top acceptance in the dilepton channel is observed to almost double over the mass range of  $130 \text{ GeV}/c^2$  to  $220 \text{ GeV}/c^2$ .

$M_{\text{top}}$	$\epsilon_{\text{geom}\cdot\text{P}_T}$	$\epsilon_{\text{trigger}}$	$\epsilon_{\text{ID}}$	$\epsilon_{\text{SS}}$	$\epsilon_{\text{iso}}$	$\epsilon_{\text{mass}}$	$\epsilon_{\cancel{E}_T}$	$\epsilon_{2\text{-jet}}$	$\epsilon_{\text{dil}}$
130	2.03	0.937	0.609	0.988	0.951	0.882	0.784	0.720	$0.534\pm 0.020$
140	2.19	0.937	0.590	0.981	0.954	0.891	0.750	0.759	$0.573\pm 0.020$
150	2.43	0.937	0.560	0.973	0.959	0.878	0.765	0.786	$0.629\pm 0.021$
160	2.58	0.937	0.542	0.968	0.960	0.877	0.787	0.829	$0.704\pm 0.022$
170	2.76	0.937	0.516	0.974	0.949	0.890	0.802	0.853	$0.757\pm 0.023$
175	2.91	0.937	0.512	0.966	0.962	0.866	0.794	0.864	$0.784\pm 0.025$
180	2.99	0.937	0.501	0.974	0.959	0.890	0.796	0.869	$0.807\pm 0.024$
200	3.34	0.937	0.488	0.974	0.954	0.882	0.810	0.865	$0.889\pm 0.025$
210	3.46	0.937	0.460	0.977	0.952	0.889	0.801	0.898	$0.905\pm 0.025$
220	3.69	0.937	0.451	0.971	0.967	0.891	0.797	0.905	$0.961\pm 0.028$

Table 4.3: Efficiencies for the Run 1B dilepton event selection cuts.

Originally,  $\epsilon_{\text{dil}}$  was calculated from PYTHIA V\_5.6 Monte Carlo event samples. The dilepton acceptance for a top quark mass of 175 GeV/c<sup>2</sup> was quoted as  $\epsilon_{\text{dil}} = 0.77 \pm 0.08\%$ .<sup>[70]</sup> Recently, the acceptance has been recalculated using an average of results obtained from samples of PYTHIA V\_5.7 and HERWIG V\_5.6 Monte Carlo events. As a result, the acceptance in the dilepton channel for a top quark mass of 175 GeV/c<sup>2</sup> is now quoted by CDF as  $\epsilon_{\text{dil}} = 0.74 \pm 0.08\%$ .<sup>[73]</sup>

## 4.6 Background Events in the Dilepton Channel

The Standard Model predicts the existence of events that can potentially imitate the dilepton signal. The dominant sources of these background events were listed in section 4.4. In order to pass the jet selection cuts of section 4.4 most of these interactions must be coupled with QCD processes that are of higher order than the tree level production processes involved in top quark dilepton event production. Therefore, the backgrounds should have a lower production cross section than the signal. In addition, these events are expected to be substantially suppressed by the dilepton selection cuts listed in sections 4.1, 4.2 and 4.4. However, as shown in section 4.5, these cuts were also designed to maintain high signal acceptance. This section outlines the methods used to predict the background contributions and to verify that the dilepton cuts yield a high significance,  $S/\sqrt{B}$ , where  $S$  is the number of signal events and  $B$  is the total number of background events. Much of the information presented in this section was obtained from reference [46], where it is described in considerable detail.

#### 4.6.1 $W^+W^-$

This background process is:  $p\bar{p} \rightarrow W^+W^- + 2jets + X \rightarrow l^+\nu l^-\bar{\nu} + 2jets + X$ , where the jets come from a higher order QCD processes. The number,  $N^{W^+W^-}$ , of  $W^+W^-$  events in 109 pb<sup>-1</sup> of data that are expected to pass the dilepton event selection cuts is given by:

$$N^{W^+W^-} = \epsilon^{W^+W^-} \cdot \sigma(p\bar{p} \rightarrow W^+W^-) \cdot BR(W^+W^- \rightarrow l^+\nu l^-\bar{\nu}) \cdot \int \mathcal{L} dt \quad (4.3)$$

where  $\epsilon^{W^+W^-}$  is the efficiency for the dilepton selection cuts to accept  $W^+W^-$  events,  $\sigma(p\bar{p} \rightarrow W^+W^-)$  is the theoretical cross section for  $W^+W^-$  production via  $p\bar{p}$  collisions at 1.8 TeV,  $BR(W^+W^- \rightarrow l^+\nu l^-\bar{\nu}) = 0.05$  is the branching ratio for both of the  $W$  bosons to decay leptonically and  $\int \mathcal{L} dt = 109 \text{ pb}^{-1}$  is the integrated luminosity. From theoretical calculations,  $\sigma(p\bar{p} \rightarrow W^+W^-) = 9.5 \text{ pb}$  with a 30% uncertainty. To determine  $\epsilon^{W^+W^-}$ , large samples of Monte Carlo  $W^+W^-$  events were generated with detector simulation, the dilepton selection cuts were applied and the lepton ID cut efficiency was corrected via the method used in the acceptance calculation of section 4.5.  $N^{W^+W^-}$  was then calculated using  $\epsilon^{W^+W^-}$ . For a 100,000 event sample of ISAJET events with QFL simulation this number was found to be  $N^{W^+W^-} = 0.58 \pm 0.19$  events. However, this number was not taken as the final result because it is believed that ISAJET does not produce the correct fraction of  $W^+W^-$  events that pass the 2 jet cut of the dilepton event selection process. This 2-jet fraction was calculated from a sample of  $Z^0$  events that were generated with ISAJET and detector simulation with the  $Z^0$  mass set equal to 250 GeV/c<sup>2</sup>, the average invariant mass of  $W^+W^-$  pairs. Comparing this 2-jet fraction to the 2-jet fraction of actual  $Z^0$  data suggested that the 2-jet fraction found for ISAJET  $W^+W^-$  events should be scaled up by a factor of 1.61. This conclusion is based on the assumption that the jet activity in  $W^+W^-$  events is very similar to that in  $Z^0$  events. An independent study using VECBOS<sup>[74]</sup> with the HERPRT<sup>[75]</sup> jet fragmentation model found this factor to be 1.44 when the  $Q^2$  scale is set to 250 GeV and 1.83 when the  $Q^2$  scale is set to the average  $P_T$  of the jets. Using the average value ( $1.6 \pm 0.4$ ) of the three versions of the factor, the  $W^+W^-$  background was calculated to be:  $N^{W^+W^-} = 0.36 \pm 0.11$  events.



#### 4.6.2 Drell-Yan

In this background process  $q\bar{q}$  annihilation produces a  $Z^0$  boson or a virtual photon, which subsequently decays into a  $e^-e^+$  or a  $\mu^-\mu^+$  pair. Such events can imitate the  $t\bar{t}$  signal if they contain at least 2 jets from higher order QCD processes and have  $\vec{E}_T$  from the mismeasurement of jets and leptons. Since the intermediate boson in most Drell-Yan events tends to be a  $Z^0$  boson and since this boson is predominantly on the  $Z^0$  mass shell, the cut on the dilepton invariant mass,  $M_{l+l-}$ , mentioned in section 4.4 reduces this background considerably by excluding it from the region where  $75 < M_{l+l-} < 105 \text{ GeV}/c^2$ . A large data sample of  $Z^0$  events was used to calculate the Drell-Yan contamination outside of the  $Z^0$  mass window.

The expected number of Drell-Yan background events,  $N_{\text{bg}}^{\text{DY}}$ , is given by:

$$N_{\text{bg}}^{\text{DY}} = N_Z^{\text{pass}} \frac{\epsilon_{2j}^{\text{lo}} N_{\text{lo}} + \epsilon_{2j}^{\text{hi}} N_{\text{hi}}}{\epsilon_{2j}^Z N_Z} \quad (4.4)$$

where  $N_Z^{\text{pass}}$  is the number of  $Z^0$  events inside the  $Z^0$  mass window that pass the 2-jet and  $\vec{E}_T$  dilepton cuts (see section 4.4) and the remaining part of the equation is a scale factor that relates the total number of  $Z^0$  events inside the window before cuts,  $N_Z$ , to the total number of  $Z^0$  events outside the window before cuts,  $N_{\text{lo}} + N_{\text{hi}}$ . Note:  $N_{\text{lo}}$  ( $N_{\text{hi}}$ ) is defined as the number of events for which  $M_{l+l-} < 75 \text{ GeV}/c^2$  ( $M_{l+l-} > 105 \text{ GeV}/c^2$ ). The extra factors  $\epsilon_{2j}^Z$ ,  $\epsilon_{2j}^{\text{lo}}$  and  $\epsilon_{2j}^{\text{hi}}$  in equation 4.4 are needed because the number of Drell-Yan events with  $\geq 2$  jets varies with  $M_{l+l-}$ . The fraction of Drell-Yan events containing 2 or more jets can be approximated as a linear relation in  $M_{l+l-}$  for each of the three regions defined by the  $Z^0$  mass window cut. Using this linear relation,  $\epsilon_{2j}^Z$  is defined as the fraction of Drell-Yan events inside the  $Z^0$  mass window that corresponds to the average value of  $M_{l+l-}$  in that region. The factors  $\epsilon_{2j}^{\text{lo}}$  and  $\epsilon_{2j}^{\text{hi}}$  are defined in an analogous manner. Using equation 4.4 with the  $Z^0$  data, a preliminary value of  $0.70 \pm 0.20$  events was obtained for  $N^{\text{DY}}$ .

This result is presumed to represent a slight overestimate of the Drell-Yan background since other types of events, most notably  $t\bar{t}$  events, will contribute to  $N_Z^{\text{pass}}$ . The expected numbers of  $e^+e^-$  and  $\mu^+\mu^-$  events from  $t\bar{t}$  decay in the  $Z^0$  data sample that lie within the  $Z^0$  mass window and that pass all of the dilepton event selection cuts are given by:

$$N_{\text{top}}^Z(ee) = (1 - \epsilon_Z) \cdot \int \mathcal{L} dt \cdot \sigma_{t\bar{t}} \cdot \epsilon_{\text{dil}} \cdot R_{ee} \quad (4.5)$$

$$N_{\text{top}}^Z(\mu\mu) = (1 - \epsilon_Z) \cdot \int \mathcal{L} dt \cdot \sigma_{t\bar{t}} \cdot \epsilon_{\text{dil}} \cdot R_{\mu\mu} \quad (4.6)$$

where  $\epsilon_Z$  is the efficiency of the  $Z^0$  mass cuts for  $e^-e^+$  and  $\mu^-\mu^+$  events,  $\int \mathcal{L} dt = 109 \text{ pb}^{-1}$  is the integrated luminosity,  $\sigma_{t\bar{t}}$  is the  $t\bar{t}$  production cross section,  $\epsilon_{\text{dil}}$  is the top acceptance in the dilepton channel (see section 4.5) and  $R_{ee}$  ( $R_{\mu\mu}$ ) is the  $e^-e^+$  ( $\mu^-\mu^+$ ) acceptance relative to  $\epsilon_{\text{dil}}$  before the  $Z^0$  mass cut. Using a top quark mass of  $M_t = 175 \text{ GeV}/c^2$  to calculate  $N_{\text{top}}^Z(ee)$  and  $N_{\text{top}}^Z(\mu\mu)$  and then subtracting these numbers from  $N_Z^{\text{pass}}$  in equation 4.4 results in an improved Drell-Yan background estimate of  $N_{\text{bg}}^{\text{DY}} = 0.61 \pm 0.30$  events.

#### 4.6.3 $Z^0 \rightarrow \tau^+\tau^-$

This background process involves the process:  $q\bar{q} \rightarrow Z^0 \rightarrow \tau^-\tau^+ \rightarrow l^-\bar{\nu}_l\nu_\tau l^+\nu_l\bar{\nu}_\tau$ , where the charged leptons can be electrons or muons. In the presence of higher order QCD jet activity the  $\tau^-\tau^+$  pair will not be back-to-back so that the four neutrinos can contribute significant  $\cancel{E}_T$ . Therefore, events that contain two or more jets can mimic the  $t\bar{t}$  signal.

To eliminate jet activity simulation problems, the Run 1A analysis used real  $Z^0 \rightarrow e^-e^+$  events to study the  $Z^0 \rightarrow \tau^-\tau^+$  background process. In each event the electrons were replaced by taus and these taus were decayed into electrons and muons using the ISAJET Monte Carlo generator with QFL detector simulation. To increase statistics, each event was generated 80 times. Rescaling the Run 1A background result to the total integrated luminosity of Run 1 gives an estimated  $Z^0 \rightarrow \tau^-\tau^+$  contribution to the  $t\bar{t}$  signal of  $N_{\text{bg}}^{Z \rightarrow \tau\tau} = 0.62 \pm 0.11$  events. For Run 1B this background was determined from a sample of 760,000  $Z^0 \rightarrow \tau^-\tau^+$  events that were generated using ISAJET+QFL. The estimated integrated luminosity of this sample is over 30 times larger than that of Run 1. Rescaling the results of this analysis to Run 1 gives an expected background of  $N_{\text{bg}}^{Z \rightarrow \tau\tau} = 0.59 \pm 0.14$  events. Another study using VECBOS Monte Carlo events with HERPRT parton fragmentation and QFL detector simulation gives  $N_{\text{bg}}^{Z \rightarrow \tau\tau} = 0.41 \pm 0.20$  events. All three background estimates are consistent with each other within errors.

#### 4.6.4 $b\bar{b}$

In  $p\bar{p}$  collisions  $b\bar{b}$  pairs can be created from a variety of sources including direct production, gluon splitting and flavor excitation. Such events can imitate the  $t\bar{t}$  signal if they contain at least two additional QCD jets and if the  $b$  and the  $\bar{b}$  quark each fragment into high  $P_T$  leptons. For a  $b$  quark to decay into a high  $P_T$  lepton it must be very energetic, which means that its fragmentation products will be highly collimated. Thus, the high  $P_T$  leptons, being surrounded by other fragmentation products, will tend to fail both the lepton identification and the isolation cuts. In addition, the neutrinos from the fragmentation of the  $b$  and  $\bar{b}$  quarks will tend to be back-to-back so that such events are likely to fail the  $\cancel{E}_T$  cuts. For these reasons, the  $b\bar{b}$  background is expected to be the smallest of the five major backgrounds discussed in this chapter.

To study the  $b\bar{b}$  background<sup>[76]</sup>, the dilepton analysis utilized ISAJET to simulate the  $b\bar{b}$  production process, the CLEO Monte Carlo program<sup>[77],[78]</sup> to model the decay of the  $b$  quarks, and QFL to simulate the CDF detector. Two event samples, totaling  $67.5 \text{ pb}^{-1}$  of integrated luminosity, were created. In the first sample, which consisted of  $16.3 \text{ pb}^{-1}$  of luminosity, events generated by ISAJET+CLEO were only sent through QFL if they possessed at least two leptons, one with  $P_T > 15 \text{ GeV}/c$  and the other with  $P_T > 5 \text{ GeV}/c$ . These same  $P_T$  cuts were applied to a sample of low momentum  $e\mu$  events, 80% of which were estimated to be  $b\bar{b}$  events. The number of Monte Carlo  $b\bar{b}$  events passing the aforementioned lepton cuts (15 and 5 GeV) per integrated luminosity was divided by the number of such events per integrated luminosity in the data sample. This normalization factor was found to be  $1.04 \pm 0.21$ <sup>[16]</sup>. The other Monte Carlo sample, which consisted of  $51.3 \text{ pb}^{-1}$  of integrated luminosity, was required to have two generator level leptons each with  $P_T > 10 \text{ GeV}/c$ . This sample was used to determine the various rejection factors that result from applying the dilepton event selection cuts to  $b\bar{b}$  events. Rescaling the results to an integrated luminosity of  $109 \text{ pb}^{-1}$  and multiplying by the normalization factor, the number of background events due to  $b\bar{b}$  production was estimated to be  $N_{\text{bg}}^{b\bar{b}} = 0.05 \pm 0.03$  events.

#### 4.6.5 Fake leptons

These background events contain at least one hadronic jet that is misidentified as an acceptable lepton. The primary source of this background consists of  $W + \geq 3 \text{ jets}$  events in which the  $W$  boson decays leptonically. Muons can be faked by hadrons that deposit very little energy in the calorimeter but that are detected in the muon chambers. Muons can also be faked by hadrons that decay into muons before reaching the calorimeter. Electrons can be faked by jets that deposit a large fraction of their energy in the electromagnetic calorimeter. Since the probability of a hadron to fake a lepton is very small ( $\sim 10^{-4}$ ) the case of more than one jet faking a lepton is neglected. Two methods were used to obtain an estimate of the fake lepton background.

For the first method the sample of dilepton events for which both leptons have the same-sign was used since the amount of fake lepton background in this sample is expected to be comparable to that in the opposite-sign sample used for analyses. The same-sign sample contains two events, both of type  $e\mu$ , that pass all other dilepton cuts. To obtain an estimate of the fake lepton background, the efficiency of the 2-jet cut for fake lepton events was applied with the same-sign events before using the 2-jet cut on them. For this purpose a jet was defined as "fakable" if it had  $P_T > 20 \text{ GeV}/c$  and  $|\eta| < 1.2$ . The efficiency of the 2-jet cut for fake events was defined as the ratio of the number of  $W + \geq 1 \text{ fakable jet}$  events that pass the 2-jet cut to the total number of  $W + \geq 1 \text{ fakable jet}$  events. These  $W$  boson events were required to have a tight lepton and  $|\vec{E}_T| > 25 \text{ GeV}$ . Using the Run 1 data set, the efficiency of the 2-jet cut was determined to be  $0.12 \pm 0.01$ . Application to the same-sign events gave a fake lepton background estimate of  $N_{\text{bg}}^{\text{fake}}(\text{same} - \text{sign events}) = 0.24 \pm 0.17$  events.

The second method used inclusive jet samples to calculate the probability for a jet to fake a lepton. The fake lepton background was then estimated by applying this probability to the number of "fakable" jets found in  $W + \geq 3 \text{ jets}$  events. Leptons from  $W^\pm$  and  $Z^0$  boson decay were removed from the sample. However, due to lack of knowledge about the exact fraction of  $b$  jets in the sample, leptons stemming from heavy flavor decay were not removed. Therefore, the fake lepton background determined from this method is expected to be an overestimate. Application of the fake probabilities to the  $W + \geq 3 \text{ jets}$  events gave a fake lepton background

estimate of  $N_{\text{bg}}^{\text{fake}}(\text{inclusive jet events}) = 0.37 \pm 0.23$  events. Although  $N_{\text{bg}}^{\text{fake}}(\text{same-sign events})$  and  $N_{\text{bg}}^{\text{fake}}(\text{inclusive jet events})$  are very close, the latter is taken as the final result since it is more conservative.

#### 4.6.6 Mismeasured Muon Tracks

This background can arise from a  $Z^0 \rightarrow \mu^+ \mu^-$  event in which one or more muon tracks have been poorly reconstructed. The measured  $\mu^+ \mu^-$  invariant mass can then lie outside the  $Z^0$  mass window cut. In addition, this event can be given fake  $\vec{\cancel{E}}_T$  since  $\vec{\cancel{E}}_T$  is corrected for muons. If this  $Z^0 \rightarrow \mu^+ \mu^-$  event also contains at least 2 jets from higher order QCD radiation then it is possible for it to pass the dilepton event selection cuts.

These effects of mismeasured muon tracks were discovered during a study of the greater than expected number of dilepton event candidates from Run 1 (before the 2-jet cut) that contain 1 jet. The number of events found was 11 while the number expected from Monte Carlo studies is 5.3. Of the 11 events found, 4 are of the type  $\mu^+ \mu^-$ . Upon closer inspection it was learned that 3 of these events have at least one muon whose reconstructed momentum is much different from its momentum measured straight from the detector. It was shown that this difference is related to track mismeasurement, which itself leads to mismeasurement of both the  $\mu^+ \mu^-$  invariant mass and the event's  $\vec{\cancel{E}}_T$ .

Using large samples of  $Z^0 \rightarrow \mu^+ \mu^-$  and  $Z^0 \rightarrow e^+ e^-$  events from data, the number of background events expected from mismeasured muon tracks before the 2-jet cut was determined to be  $3.0 \pm 3.2$  events. The number of these events that are expected to survive the 2-jet cut is  $0.3 \pm 0.3$  events<sup>[79]</sup>.

#### 4.6.7 $W^\pm Z^0$ and $Z^0 Z^0$

Besides  $W^+ W^-$  production, two other types of vector boson production can potentially mimic the  $t\bar{t}$  signal. These two additional background sources are  $W^\pm Z^0$  and  $Z^0 Z^0$  production.

A  $W^\pm Z^0$  event can pass the dilepton event selection cuts if the  $Z^0$  boson decays into two high  $P_T$  leptons, the  $W$  boson decays hadronically and the jet energies are mismeasured such that the  $\vec{\cancel{E}}_T$  is large. Using a sample of  $Z^0 + \geq 2\text{jet}$  data events, the combined efficiency for passing the  $\vec{\cancel{E}}_T$  cut, the 2-jet cut and the  $Z^0$  mass window

cut was found to be 0.6%. For  $W^+W^-$  events, this efficiency was estimated to be 3.7%. Combining these results with the knowledge that for Run 1 the cross section for  $W^+W^-$  production was 9.5 pb while the cross section for  $W^\pm Z^0$  production was 2.5 pb, it was concluded that  $W^\pm Z^0$  events are about 25 times less likely to pass the dilepton event selection cuts than are  $W^+W^-$  events.

$W^\pm Z^0$  events could also contribute if both vector bosons decay leptonically since there would be a greater efficiency for such events to pass the  $Z^0$  mass window cut. However, the branching ratio for this decay is 3 times higher than for the previously mentioned decay chain. In addition, this decay would have to be coupled with at least 2 higher order QCD jets. This gives a background contribution that is approximately 60 times smaller than that from  $W^+W^-$  production.

A  $Z^0 Z^0$  event can potentially fake a dilepton event if one  $Z^0$  boson decays leptonically, the other one decays hadronically and there is significant  $\cancel{E}_T$  from jet mismeasurement. The branching ratio for this decay is 9 %. The cross section for  $Z^0 Z^0$  production in Run 1 was 1.0 pb. Using this information along with the expected combined efficiency for  $Z^0 Z^0$  events to pass the  $\cancel{E}_T$ , 2-jet and  $Z^0$  mass window cuts leads to an expected background contribution comparable to that from  $W^\pm Z^0$  production.

Based on these results the background due to  $W^\pm Z^0$  and  $Z^0 Z^0$  production is presumed to be very small.

#### 4.6.8 Other Backgrounds

There are a few other potential backgrounds whose contributions are very small or completely negligible. They include radiative  $Z^0$  boson,  $W^\pm b\bar{b}$ ,  $Z^0 b\bar{b}$  and Standard Model Higgs boson production.

Radiative  $Z^0$  boson background events can occur when a  $q\bar{q}$  pair annihilates into a  $Z^0$  boson which radiates a high energy photon before decaying into a  $e^+e^-$  or a  $\mu^+\mu^-$  pair. To be mistaken for a dilepton event the photon must pass the jet cuts and have high enough energy to drive the invariant mass of the lepton pair below the  $Z^0$  mass window. The event must also have an extra QCD jet and it must have sufficient  $\cancel{E}_T$  from jet energy mismeasurement. This background was estimated as follows: First the number of data events containing a photon with  $E_T > 10$  GeV and a dilepton mass below the  $Z^0$  mass window was counted. This number was scaled by the ratio of the number of  $Z^0 + \geq 1 \text{ jet}$  events and the total number of  $Z^0$  events. This result was

then scaled by the ratio of the number of  $Z^0 + \geq 1 \text{ jet} + \cancel{E}_T$  events and the number of  $Z^0 + \geq 1 \text{ jet}$  events. This gave the background estimate. The expected number of background events from radiative  $Z^0$  bosons in the Run 1 data sample is  $0.07 \pm 0.04$  events<sup>[46]</sup>.

$W^\pm b\bar{b}$  production involves the process  $q\bar{q} \rightarrow W^\pm g$ . This process can pass the dilepton cuts if the  $W^\pm$  boson decays leptonically, the gluon splits into a  $b\bar{b}$  pair, one of the  $b$  quarks decays leptonically to a high  $P_T$  lepton and the event contains significant  $\cancel{E}_T$  from mismeasurement of jet energies. This background is expected to be small because  $b\bar{b}$  pairs from gluon splitting are generally highly collimated and have too low energy to produce a lepton that will pass the dilepton cuts. A sample of HERWIG+QFL  $W^\pm b\bar{b}$  Monte Carlo events corresponding to  $10 \text{ fb}^{-1}$  of integrated luminosity was used to estimate the contribution to the dilepton signal from Run 1. The number of background events expected from  $W^\pm b\bar{b}$  events was determined to be  $0.005 \pm 0.004$  events and is regarded as negligible.

The process  $Z^0 b\bar{b}$  is similar to the process  $W^\pm b\bar{b}$  and it can mimic the dilepton signal in an analogous way, but with both leptons coming from the decay of the weak boson in this case. This background is considered negligible because the cross section for  $Z^0 b\bar{b}$  production is 10 times smaller than for  $W^\pm b\bar{b}$  production, which itself is negligible.

At the Tevatron, Standard Model Higgs production can occur via the process  $q\bar{q} \rightarrow W^* \rightarrow W^\pm H^0$  or the process  $q\bar{q} \rightarrow Z^* \rightarrow Z^0 H^0$ . If the Higgs boson mass,  $M_H$ , is less than  $2M_W$  then it will most likely decay to a  $b\bar{b}$  pair. A  $W^\pm H^0$  event can pass the cuts if the  $W^\pm$  boson decays semi-leptonically and if one of the  $b$  quarks decays semi-leptonically into a high  $P_T$  lepton. A  $Z^0 H^0$  event can contribute to the signal if the  $Z^0$  boson decays to a  $e^+e^-$  or a  $\mu^+\mu^-$  pair. However, the chance for the latter type of event to pass the  $Z^0$  mass window cut is extremely small. Using a sample of 26,800 PYTHIA+QFL  $Z^0 H^0 + W^\pm H^0$  Monte Carlo events that were generated with  $M_H = 100 \text{ GeV}/c^2$ , only 3 events passed the dilepton cuts. The number of events expected in Run 1 was determined to be  $0.01 \times (\sigma_{WH} + \sigma_{ZH})$ , where  $\sigma_{WH} + \sigma_{ZH}$  is the sum of the theoretical cross sections for the  $W^\pm H^0$  and  $Z^0 H^0$  production processes and is in units of pb. Assuming this sum to be of the order of a few pb for  $M_H = 100 \text{ GeV}/c^2$ , then the Standard Model Higgs background is negligible.

#### 4.6.9 Summary of the Background Sources

Table 4.4 gives a complete summary of the expected background contributions to the Run 1 data sample of dilepton event candidates. The backgrounds due to radiative  $Z^0$  boson,  $W^\pm Z^0$ ,  $Z^0 Z^0$  and  $W^\pm b\bar{b}$  production have been combined to give a total contribution of  $0.1 \pm 0.1$  events. The total number of expected background events for the dilepton event data sample is  $2.4 \pm 0.5$  events.

Background Type	Expected Number of Events
Drell-Yan	$0.61 \pm 0.30$
$Z^0 \rightarrow \tau^- \tau^+$	$0.59 \pm 0.14$
Fake Leptons	$0.37 \pm 0.23$
$W^+ W^-$	$0.36 \pm 0.11$
Mismeasured Muon Tracks	$0.3 \pm 0.3$
$b\bar{b}$	$0.05 \pm 0.03$
(Radiative $Z^0$ , $W^\pm Z^0$ , $Z^0 Z^0$ , $W^\pm b\bar{b}$ )	$0.1 \pm 0.1$
Total	$2.4 \pm 0.5$

Table 4.4: Expected background for the dilepton event sample of Run 1.

### 4.7 Dilepton Event Data Sample

A description of the complete dilepton event data sample collected by the CDF detector during Run 1 is presented. Before application of the 2-jet cut, 8 events are found with 0 jets while the expected number is  $8 \pm 2$  events. The number of events found with 1 jet is 11 while the expected number of 1 jet events is  $7 \pm 2$ . However, the  $t\bar{t}$  contributions to these two sets of events are expected to be only  $0.03 \pm 0.02$  and  $1.1 \pm 0.5$  events, respectively. Of the 11 events with 1 jet, 4 are  $\mu^+ \mu^-$  events, 3 of which have a muon track whose kinematics after reconstruction is much different from its kinematics straight from the detector. As mentioned in section 4.6.6, these 3 events are consistent with radiative  $Z^0$  boson events. The expected number of events from this background is  $1.4 \pm 1.5$ . Two events pass all of the dilepton event selection cuts except the opposite sign cut on lepton candidates. The expected number of such same-sign events is  $0.24 \pm 0.11$  from  $t\bar{t}$  production and  $0.37 \pm 0.23$  from fake lepton background. A  $\mu^+ \mu^- \gamma$  event which passes all of the dilepton event selection cuts has



been rejected because it fails a recently introduced cut to eliminate background from mismeasured muon tracks due to radiative  $Z^0$  boson background events.

After application of the standard dilepton event selection cuts described in sections 4.1, 4.2 and 4.4, the data sample consists of 9 events. As quoted in section 4.6.9, the expected number of background events for this data sample is  $2.4 \pm 0.5$  events. Four of the nine candidate events have one jet tagged as a  $b$  quark by the SVX. Two of these four jets were also tagged by the SLT-tagger. No jets were tagged by the SLT tagger alone. The expected number of  $b$ -tagged jets in a sample of seven  $t\bar{t}$  events is  $4.3 \pm 0.4$ . If all nine candidate events were from background sources then only  $0.7 \pm 0.2$  jets would be expected to be  $b$ -tagged.

Using an integrated luminosity of  $109 \text{ pb}^{-1}$ , a signal of 9 events, a background of  $2.4 \pm 0.5$  events and a dilepton acceptance of  $0.74 \pm 0.08\%$  (calculated for a top quark mass of  $175 \text{ GeV}/c^2$ ), the dilepton analysis measures the  $t\bar{t}$  production cross section to be  $\sigma_{t\bar{t}} = 8.2^{+4.4}_{-3.4} \text{ pb}$  (see equation 4.2).

When performing top quark mass reconstruction analyses on Run 1 CDF data it is customary to apply a cut on a kinematical quantity called  $H_T$  to further reduce the background while maintaining good efficiency.  $H_T$  is defined as the scalar sum of the  $E_T$ 's of the two leptons ( $P_T$ 's if muons), the  $E_T$ 's of the two highest  $E_T$  jets and the  $|\vec{E}_T|$ . It has been shown that application of the cut  $H_T > 170 \text{ GeV}$  is 95% efficient for a top quark mass of  $175 \text{ GeV}/c^2$ . After this cut the data sample consists of 8 events and the expected background for this reduced sample is  $1.3 \pm 0.3$  events.

# Chapter 5

## Top Quark Mass Determination

The top quark mass fitting technique used by this analysis was developed for dilepton events by R.H. Dalitz and G. Goldstein<sup>[80]</sup>. It can also be used for lepton+jets  $t\bar{t}$  events, due to modifications by R.H. Dalitz, G. Goldstein and K. Sliwa<sup>[81],[82],[83],[84]</sup>. As stressed by K. Sliwa in reference [85], a major advantage of the technique is its lack of dependence on  $\vec{\cancel{E}}_T$ . For a given event, the method determines the most likely mass of the top quark consistent with the hypothesis that two objects of equal mass (the top and antitop quark in this case) were produced with limited transverse energy and subsequently decayed via the dilepton channel. The procedure is based on a geometrical construction and a likelihood technique.

### 5.1 The Initial Problem

In the dilepton channel,  $t\bar{t}$  pairs are produced and subsequently decay via the following process (see section 1.2.1):

$$p\bar{p} \rightarrow t\bar{t} + X \rightarrow W^+bW^-\bar{b} + X \rightarrow l^+\nu bl^-\bar{\nu}\bar{b} + X$$

where the charged leptons ( $l^+$  and  $l^-$ ) are either electrons or muons. To determine the top quark mass, the fitting technique uses the measurable kinematics of the final decay products of the  $t\bar{t}$  system, namely the kinematics of the two charged leptons and the hadronic jets stemming from the  $b$  and  $\bar{b}$  quarks.

The masses of all final decay particles in the dilepton channel are known. The kinematics of the charged leptons can be measured by CDF with great precision (see sections 2.2.1 and 2.2.3). The kinematics of the  $b$  and  $\bar{b}$  quarks can be estimated from jet kinematics that are appropriately corrected for both detector and physics effects (see sections 3.2 and 3.3).

The problem is under-constrained because the three-momenta of the two neutrinos cannot be measured. Although  $\vec{\cancel{E}}_T$  provides some information about the kinematics of the  $\nu\bar{\nu}$  system in the transverse plane it is a poorly measured quantity whose accuracy rapidly deteriorates with increasing jet multiplicity (see appendix B).

## 5.2 The Dalitz-Goldstein Method

The essential features of the Dalitz-Goldstein mass fitting technique are presented here. This method assumes a set of initial constraints and solves for the neutrino kinematics by employing a geometrical interpretation of these constraints. To determine the most likely mass of the top quark consistent with the data, all possible choices of initial constraints are weighted by a likelihood technique.

### 5.2.1 Choice of Constraints

For dilepton events, the Dalitz-Goldstein method treats the four-momenta of the two neutrinos as the eight unknown quantities of the problem. To solve for these unknowns it uses the following eight equations of constraint:

$$(p_{l+} + p_\nu)^2 = M_W^2 \quad (5.1)$$

$$(p_{l-} + p_{\bar{\nu}})^2 = M_W^2 \quad (5.2)$$

$$(p_t - p_{l+} - p_b)^2 = M_\nu^2 = 0 \quad (5.3)$$

$$(p_{\bar{t}} - p_{l-} - p_{\bar{b}})^2 = M_\nu^2 = 0 \quad (5.4)$$

$$(p_t)^2 = M_t^2 \quad (5.5)$$

$$(p_{\bar{t}})^2 = M_t^2 \quad (5.6)$$

$$-P_x^t \sim P_x^{\bar{t}} \quad (5.7)$$

$$-P_y^t \sim P_y^{\bar{t}} \quad (5.8)$$

where  $p_t$ ,  $p_{\bar{t}}$ ,  $p_{l+}$ ,  $p_{l-}$ ,  $p_b$ ,  $p_{\bar{b}}$ ,  $p_\nu$  and  $p_{\bar{\nu}}$  are the four-momenta of the particles involved in the decay;  $M_W$  is the mass of the  $W$  bosons,  $M_\nu$  is the mass of the neutrinos and  $M_t$  is the mass of the top quark;  $P_x^t$  ( $P_x^{\bar{t}}$ ) is the x-component of the transverse momentum of the top (antitop) quark; Similarly,  $P_y^t$  ( $P_y^{\bar{t}}$ ) is the y-component of the transverse momentum of the top (antitop) quark.

Equations 5.1 and 5.2 utilize the known mass of the  $W$  bosons, equations 5.3 and 5.4 make use of the negligible mass of the neutrinos and equations 5.5 and 5.6 reflect the fact that the top and antitop quark masses are equal according to the Standard Model. Equations 5.5 and 5.6 will be applied over a wide range of possible top quark masses,  $M_t$ . Equations 5.7 and 5.8 are classified as "weak" constraints.

These equations will only be exact if the the total transverse momentum from initial state radiation cancels out the total transverse momentum from the intrinsic partons of the  $p\bar{p}$  system, so that the  $t\bar{t}$  system is produced with zero transverse momentum. These constraints will be applied by using a relative likelihood factor that depends on the expected transverse energy of the  $t\bar{t}$  system as determined from Monte Carlo studies (see section 5.2.3 below). It should be noted that while the mean value of the transverse momentum of the  $t\bar{t}$  system is expected to be close to zero at CDF this is not a necessary assumption for the fitting procedure. If the mean value was close to some other value the "weak" constraints could simply be modified accordingly.

### 5.2.2 Geometrical Construction

To apply the Dalitz-Goldstein method to dilepton events, equations 5.1 and 5.3 are rewritten in terms of the top and bottom quark kinematics as:

$$(\vec{P}_t - \vec{P}_b)^2 = (E_t - E_b)^2 - M_W^2 \equiv R_W^2 \quad (5.9)$$

$$(\vec{P}_t - \vec{P}_b - \vec{P}_{l+})^2 = (E_t - E_b - E_{l+})^2 \equiv R_\nu^2 \quad (5.10)$$

where  $\vec{P}_t$ ,  $\vec{P}_b$  and  $\vec{P}_{l+}$  are the three-momenta of the top quark, bottom quark and positively charged lepton, respectively, and  $E_t$ ,  $E_b$  and  $E_{l+}$  are their respective energies.

These equations show that the top quark three-momentum vector,  $\vec{P}_t$ , must simultaneously lie on two different spheres whose radii are  $R_W$  and  $R_\nu$ , and whose centers are separated by the charged lepton three-momentum vector,  $\vec{P}_{l+}$ . It follows that  $\vec{P}_t$  must lie on the intersection of the two spheres, which is a circle whose axis of symmetry is collinear with  $\vec{P}_{l+}$ . Neglecting the lepton mass, it can be shown that the top quark energy,  $E_t$ , is constant on a given circle and increases in the direction of  $\vec{l}$ . The complete set of circles defines the surface of a paraboloid. If the two spheres of radii  $R_W$  and  $R_\nu$  do not intersect then a set of possible top quark four-momenta for the assumed top quark mass cannot be found using the given assignment of jets and leptons to the  $t\bar{t}$  decay products.

The radius of the circle of intersection corresponding to a top quark energy,  $E_t$ , is given by:

$$r^2 = \frac{M_W^2}{|\vec{l}^\mp|}(E_t - E_0) \quad (5.11)$$

where the constant:

$$E_0 \equiv E_b - E_t + \frac{M_W^2}{4E_{l^+}} \quad (5.12)$$

is the lowest possible energy for the top quark, given the measured kinematics of the  $b$  quark and the charged lepton.

The top quark mass will vary on a circle of constant top quark energy,  $E_t$ . By assuming a top quark mass of  $M_t$ , equation 5.5 can be used. ( $M_t$  will be sampled over a wide range of possible values). This will confine the top quark three-momentum vector,  $\vec{P}_t$ , to a conic section of the paraboloid, which is, by definition, an ellipse. The eccentricity of this ellipse and its orientation relative to the paraboloid depend on the assumed value of top quark mass,  $M_t$ , and on the measured four-momenta of the leptons and jets. By using equations 5.2, 5.4 and 5.6, a similar ellipse is created for an antitop quark of mass  $M_t$ .

The exact locations of the top and antitop quark three momentum vectors on their respective ellipses correspond to the two remaining unknown quantities of the problem when a top quark mass of  $M_t$  has been assumed. Equations 5.7 and 5.8 are needed to fully constrain the problem.

### 5.2.3 Likelihood Technique

To utilize the remaining constraints and to determine the most likely mass of the top quark for a given event, a likelihood function is constructed.

The "weak" constraints (equations 5.7 and 5.8) are applied as follows: Both the top and the antitop quark ellipses for a given mass,  $M_t$ , are divided into a fine grid of evenly spaced points. For a given pair of points, one on each ellipse, the transverse momentum of the  $t\bar{t}$  system,  $P_T^{t\bar{t}}$ , is calculated. The analysis assigns the given pair of points a relative likelihood factor,  $P(X_{t\bar{t}})$ , that depends on  $P_T^{t\bar{t}}$ . The likelihood factor's dependence on  $P_{T_{t\bar{t}}}$  is determined from Monte Carlo simulations. To make the likelihood factor independent of  $M_t$  it is calculated as a function of the variable  $X_{t\bar{t}} \equiv P_{T_{t\bar{t}}}/M_t$ . It turns out that the final results of the analysis are quite insensitive to the exact form of  $P(X_{t\bar{t}})$ . In fact, a simple step function that cuts off

above an appropriate value of  $X_{t\bar{t}}$  would suffice<sup>[85]</sup>. Figure 5.1 shows overlapping  $P(X_{t\bar{t}})$  distributions that have been generated by HERWIG<sup>[58]</sup> and ISAJET<sup>[57]</sup> and normalized to the same area. An appropriately normalized step function is also shown.

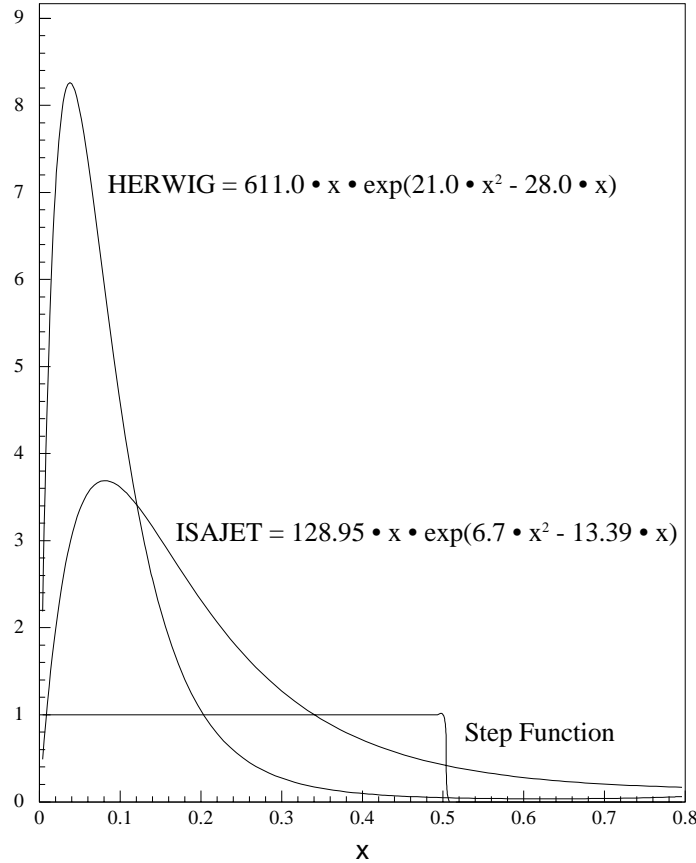


Figure 5.1: Three superimposed versions of the function  $P(X_{t\bar{t}})$ .

While the CDF detector measures the kinematics of the charged leptons and the directions of the  $b$  quarks (in the form of jets) quite well, the  $b$  jet energies can deviate significantly from the energies of their associated  $b$  quarks, due to both detector distortions and physics effects like fragmentation. As mentioned in sections 3.2 and 3.3, correction factors have been developed to improve the average measurement of the jet energies. However, the corrected jet energies still remain uncertain by an estimated  $3 - 10\%$ <sup>[16]</sup>. To account for this residual uncertainty, each measured  $b$  jet energy is smeared in a fine grid over a generous range about the measured jet energy. Since the

jet energy resolution distributions are well approximated by Gaussian distributions the range of smearing is chosen to be  $3\sigma$ , where  $\sigma$  is the width of a Gaussian fit to a given resolution distribution. The value of  $\sigma$  depends on  $M_t$  and is obtained from the DLJSCO correction package (see section 3.3). For each point within the  $3\sigma$  range the analysis assigns a probability,  $G(b)$ , which downgrades smeared  $b$  jet energies that are far from the measured value. This smearing process will generate a family of possible ellipses for both the top and the antitop quark three momentum vectors.

Thus, for each assumed top quark mass,  $M_t$ , the method scans a fine grid in the 4-dimensional parameter space formed by smearing the two measured  $b$  jet energies and dividing the resulting two families of possible ellipses into evenly spaced points. Each point in the grid is assigned a relative likelihood factor of the form  $G(b) \times G(\bar{b}) \times P(X_{t\bar{t}})$ .

Each point in the grid is also assigned a relative likelihood factor,  $P(x_1, x_2)$ , which quantifies the level of agreement between the Bjorken-x values,  $x_1$  and  $x_2$ , calculated at the given point and the Bjorken-x values predicted by theory (i.e. by the structure functions for the event).  $P(x_1, x_2)$  takes into account that for a given top quark mass,  $M_t$ , a  $t\bar{t}$  pair can be produced by either  $q\bar{q}$  or  $gg$  fusion.  $P(x_1, x_2)$  is given by:

$$P(x_1, x_2) = \frac{\sum_{i=q\bar{q}, gg} F_i(x_1) F_i(x_2) \frac{d\sigma}{dt}(\hat{s}, \hat{t})_i}{\sum_{i=q\bar{q}, gg} \frac{d\sigma}{dt}(\hat{s}, \hat{t})_i} \quad (5.13)$$

The sum is from  $i = 1$  to  $2$ ;  $F_1(x_1)$  and  $F_2(x_2)$  are the structure functions;  $\hat{s}$  is the center-of-mass energy and  $\hat{t}$  is the momentum transfer of the  $t\bar{t}$  production subprocess.  $x_1$ ,  $x_2$ ,  $\hat{s}$  and  $\hat{t}$  are calculated from the kinematics of the top quark in the  $p\bar{p}$  lab frame:

$$x_{1,2} = [E_t + E_{\bar{t}} \pm (P_{t_L} + P_{\bar{t}_L})]/2P \quad (5.14)$$

$$\hat{s} = x_1 x_2 s \quad (5.15)$$

$$\hat{t} = M_t^2 - x_1 \sqrt{s} (E_t - P_{t_L}) \quad (5.16)$$

where  $P$  is the proton momentum,  $s$  is the square of the  $p\bar{p}$  system in the center-of-mass frame and  $P_{t_L}$  ( $P_{\bar{t}_L}$ ) is the longitudinal momentum of the top quark (antitop quark) in the lab frame of the  $p\bar{p}$  system.

Finally, each point in the grid is assigned the factors  $P(l^+)$  and  $P(l^-)$  which quantify the level of agreement of the two charged lepton candidate energies as calcu-

lated in the top quark rest frame with the corresponding energies predicted by V-A calculations.

A complete likelihood,  $L_i$ , for each point in the 4-dimensional parameter space is defined as the product of the relative likelihood factors:

$$L_i = G(b) \times G(\bar{b}) \times P(X_{t\bar{t}}) \times P(x_1, x_2) \times P(l^+) \times P(l^-) \quad (5.17)$$

For a given combination of two jets and two leptons and an assumed top quark mass,  $M_t$ , the values of  $L_i$  for each point on the grid are added together and projected onto the top quark mass axis. This procedure is repeated for a wide range of possible top quark masses ( $86 < M_t < 386 \text{ GeV}/c^2$ ) to form a combination likelihood distribution as a function of top quark mass. The peak of this distribution points to the most likely mass for the given jet-lepton combination. The integral of the distribution is defined as the combination likelihood,  $L_{comb.}$ . Its magnitude is directly proportional to how likely the combination is compared to other combinations.

For a given jet-lepton combination, the  $b$  quark and neutrino kinematics are calculated as  $L_i$  weighted averages of the kinematics calculated for each point in the 4-dimensional parameter space.

To make use of the measured  $\vec{\cancel{E}}_T$ , each combination likelihood distribution is multiplied by a relative likelihood factor of the form  $G_{\vec{\cancel{E}}_T} = G_{\vec{\cancel{E}}_T}^x \times G_{\vec{\cancel{E}}_T}^y$ , which downgrades solutions for which the observed  $\vec{\cancel{E}}_T$  is in poor agreement with the  $E_T$  of the  $\nu\bar{\nu}$  system found in the fit.  $G_{\vec{\cancel{E}}_T}^x$  and  $G_{\vec{\cancel{E}}_T}^y$  are calculated from Gaussian distributions whose widths are determined from HERWIG Monte Carlo events. The widths are observed to increase linearly with  $M_t$  and are typically from 20 to 40  $\text{GeV}/c^2$ . Note that  $G_{\vec{\cancel{E}}_T}$  does not alter the shape of the likelihood distributions but it can help to choose one jet-lepton combination over another.

For each event, all jet-lepton combinations are sampled, provided that the jets and leptons pass the standard CDF dilepton event selection cuts. The method chooses the combination with the largest value of  $L_{comb.} \times G_{\vec{\cancel{E}}_T}$ . For the remainder of this dissertation this jet-lepton combination will be referred to as the "best" jet-lepton combination and its associated likelihood distribution will be referred to as the "best" combination likelihood distribution for the given event.



### 5.3 Data Sample

The Dalitz-Goldstein method has been applied to the standard sample of CDF dilepton events from Run 1. When a jet clustering cone size of 0.4 is used the sample consists of 9 events, 2 of which are expected to be background. After application of the cut  $H_T > 170$  GeV (see section 4.7), 1 event is eliminated and 1 of the remaining 8 events is expected to come from background. Unless stated otherwise, the  $H_T$  cut will be implied for all results presented in this dissertation.

The jets were corrected for both detector and physics effects by using the correction packages described in sections 3.2 and 3.3. All jet-lepton combinations were sampled provided that the jets and leptons passed the standard CDF cuts (see chapter 4). For each event, the combination with the largest value of  $L_{comb.} \times G_{\vec{E}_T}$  was chosen. A jet clustering cone size of 0.7 was also sampled. In this case, the jets were required to have uncorrected  $E_T > 12$  GeV. All other cuts remained the same. One event was rejected when using a cone size of 0.7. A jet clustering cone size of 0.4 will be implied for all results presented in this dissertation unless results using a cone size of 0.7 are explicitly mentioned for comparison.

Figure 5.2 shows the combination likelihood distributions for the possible jet-lepton pairings in event 41540\_127085 (event number 127085 of data run 41540) when a jet clustering cone size of 0.4 is used. Only two jets in this event pass the standard cuts. Therefore, this event has only two possible jet-lepton pairings. From the figure it is apparent that only the jet-lepton combination on the right has a solution to the fit. Figure 5.3 shows an event (45047\_104393) with three good jets so that there are six possible jet-lepton combinations. Clearly the combination shown in the second row and second column is the one with largest value of  $L_{comb.} \times G_{\vec{p}_T}$ . Event 63700\_272140 is the event that is rejected by the  $H_T$  cut. Figure 5.4 shows that both of this event's possible likelihood distributions give relatively low masses.

By examining the  $P(X_{t\bar{t}})$  distributions shown in figure 5.1 one might surmise that the likelihood technique is biased toward smaller top quark masses. Events 57621\_45230, 66046\_380045 and 69808\_639398 (which are shown in figures 5.5, 5.6 and 5.7, respectively) help to refute this argument. For all three events, the technique happens to choose the combination likelihood distribution with the largest mean value. These are the histograms in the upper right-hand corners of each figure.

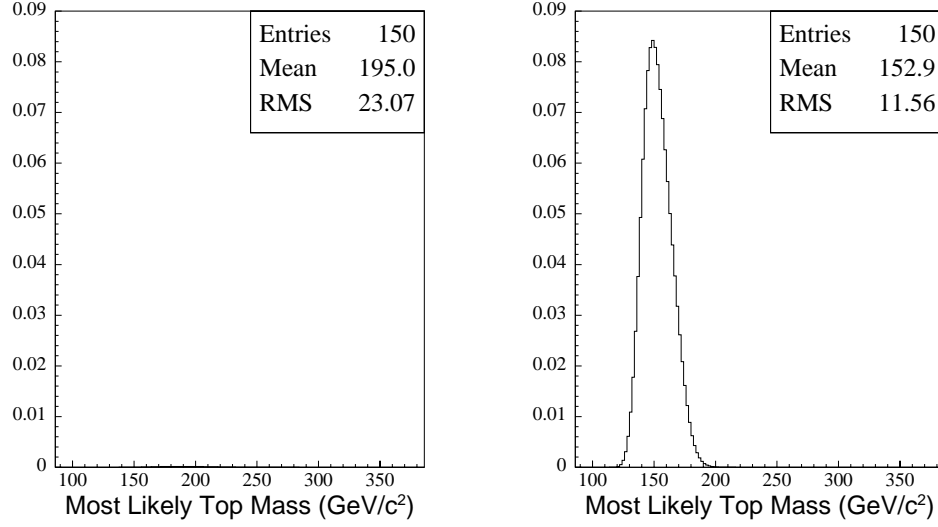


Figure 5.2: Combination likelihood distributions for data event 41540\_127085.

Figure 5.8 shows the combination likelihood distributions for event 67581\_129896 when a jet clustering cone size of 0.4 is applied. Its largest value of  $L_{comb.} \times G_{\vec{p}_T}$  is small. This event is rejected when a jet clustering cone size of 0.7 is used. Event 66046\_380045 (figure 5.6) is another event whose largest  $L_{comb.} \times G_{\vec{p}_T}$  value is relatively low. Because events 66046\_380045 and 67581\_129896 have uncharacteristically large  $|\vec{E}_T|$ , it has been speculated by independent analysis groups that they are not even  $t\bar{t}$  events. For instance, Barnett and Hall<sup>[86]</sup> have classified them as possible events involving the supersymmetric particles called squarks.

For each event the jet-lepton combination with the largest value of  $L_{comb.} \times G_{\vec{p}_T}$  contains the  $b$ -tagged jets. This is notable since the  $b$ -tagged jet is not always one of the two highest  $E_T$  jets. Event 45047\_104393 (figure 5.3) is an example of an event where the jet with the third highest value of  $E_T$  was  $b$ -tagged. The histogram in the second row and second column of Figure 5.3 shows the combination likelihood distribution with the largest value of  $L_{comb.} \times G_{\vec{p}_T}$ . This combination uses the first and third highest  $E_T$  jets. The likelihood distribution for the combination that involves the first and second highest  $E_T$  jets of the event is shown in the upper left-hand corner. The mean value of this distribution is 161.9 GeV/c<sup>2</sup>, which happens to be quite close to that of the best combination likelihood distribution (which is 159.0 GeV/c<sup>2</sup>). However, the value of  $L_{comb.} \times G_{\vec{p}_T}$  for the best combination is significantly larger.

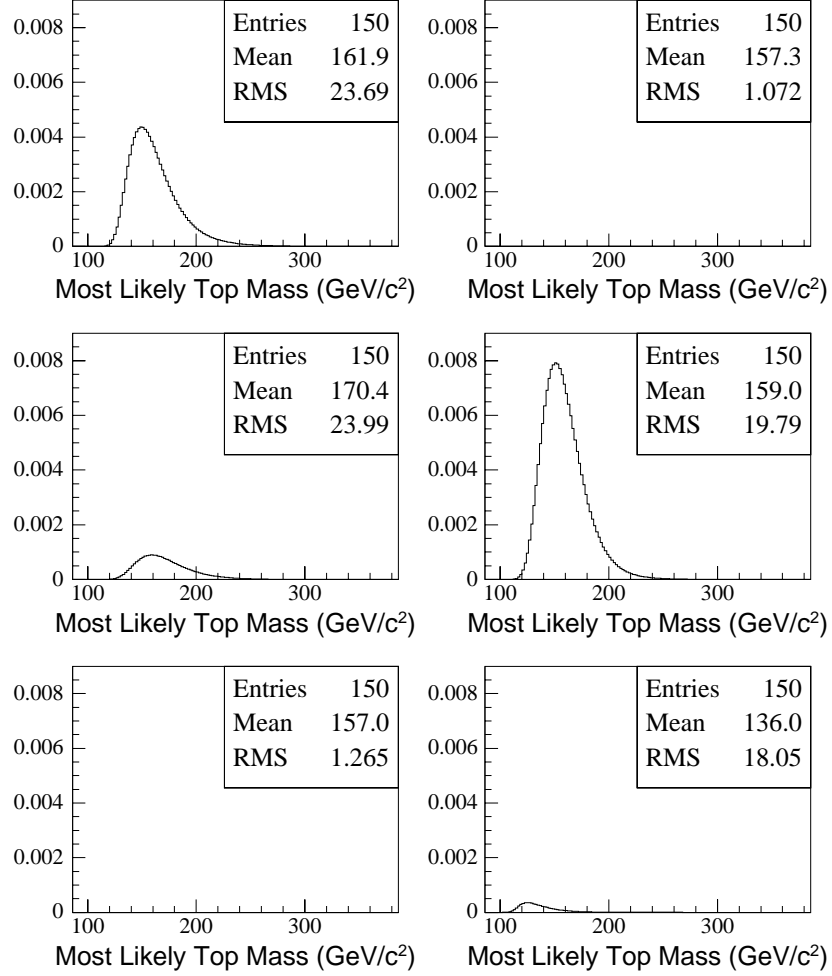


Figure 5.3: Combination likelihood distributions for data event 45047\_104393.

Figure 5.9 shows the best combination likelihood distribution for each of the 9 data events that pass the standard CDF dilepton cuts when a jet clustering cone size of 0.4 is used and no  $H_T$  cut is applied. The results using a cone size of 0.7 are similar and can be found in reference [107].

## 5.4 Joint Likelihood Method

The top quark mass must be estimated by combining information contained in the best combination likelihood distributions for each data event (see figure 5.9). To take advantage of the good signal to background ratio expected for dilepton events (see

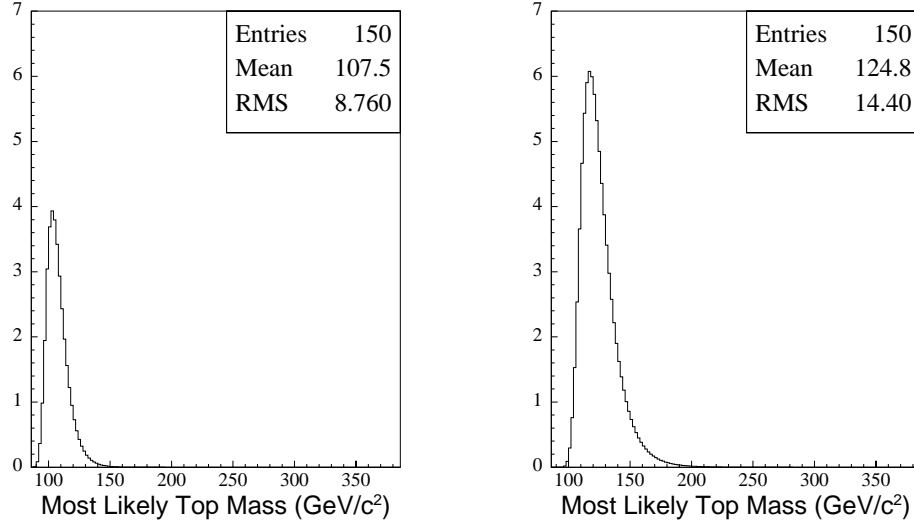


Figure 5.4: Combination likelihood distributions for data event 63700\_272140.

chapter 4) we make the initial assumption that all events in the data sample are from  $t\bar{t}$  production. Statistically, this approach is equivalent to multiplying the best combination likelihood distributions for each event together to form a new likelihood distribution which is defined as the "joint likelihood distribution". Assuming that most of the events are indeed dilepton events, then the mean of the joint likelihood distribution should give a good estimate of the true top quark mass and the R.M.S. of this distribution should be much smaller than that of the individual combination likelihood distributions used to form it.

Due to the choice of binning resolution, the histograms of the best combination likelihood distributions used to construct the joint likelihood distribution can contain zero entries. Since these bins can be multiplied with bins containing non-zero entries then some of the bins of the resulting joint likelihood distribution will falsely contain zero entries. Unwanted zero entry bins in the joint likelihood distribution can also result from the finite spread of the combination likelihood distributions. To avoid these artificial cutoffs, we add a very small constant value to each of the zero entry bins of the best combination likelihood distributions before multiplying them together. The total integrated value of these additive constants is typically less than 0.0001 times as large as the integrated value of the given combination likelihood distribution itself.

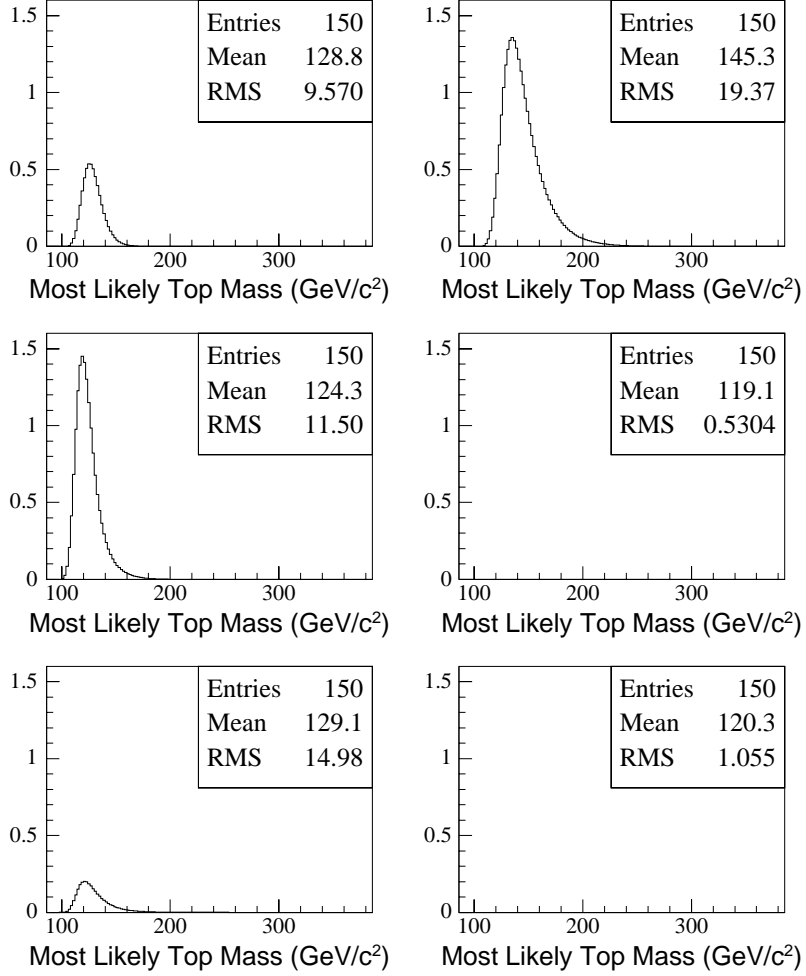


Figure 5.5: Combination likelihood distributions for data event 57621\_45230.

The left-hand plot of Figure 5.10 shows the joint likelihood distribution formed from the 9 data events when a jet clustering cone size of 0.4 is used and no  $H_T$  cut is applied. No additive constants were used to form this distribution. The distribution fits nicely to a Gaussian distribution, which is also shown on the plot. The right-hand plot of Figure 5.10 shows the same joint likelihood distribution when additive constants are applied. The results for the the two plots are almost identical. However, to be conservative, small constant values have been added to the zero entry bins of all combination likelihood distributions used by this analysis.

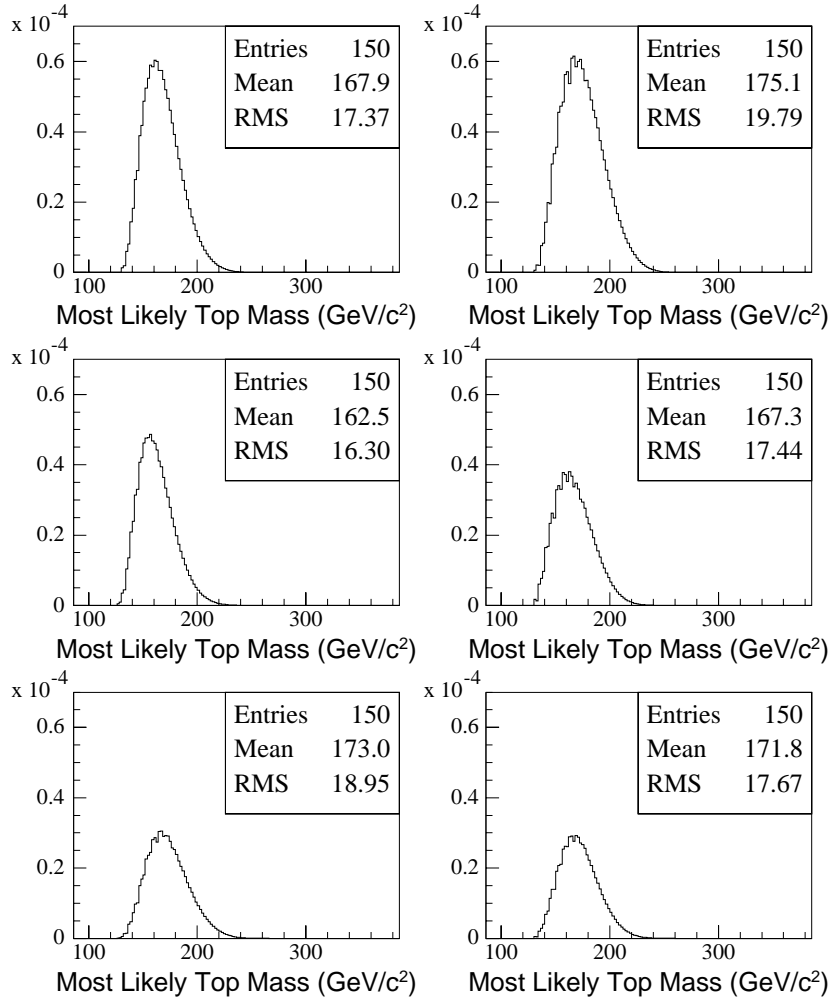


Figure 5.6: Combination likelihood distributions for data event 66046\_380045.

## 5.5 Preliminary Monte Carlo Studies

Before applying the Dalitz-Goldstein method to real data it was necessary to perform several preliminary studies on Monte Carlo events to determine the technique's level of effectiveness in choosing the correct top quark mass. The results of these studies both confirmed the validity of the technique and necessitated the development of some additional procedures to obtain the final mass measurement from data.

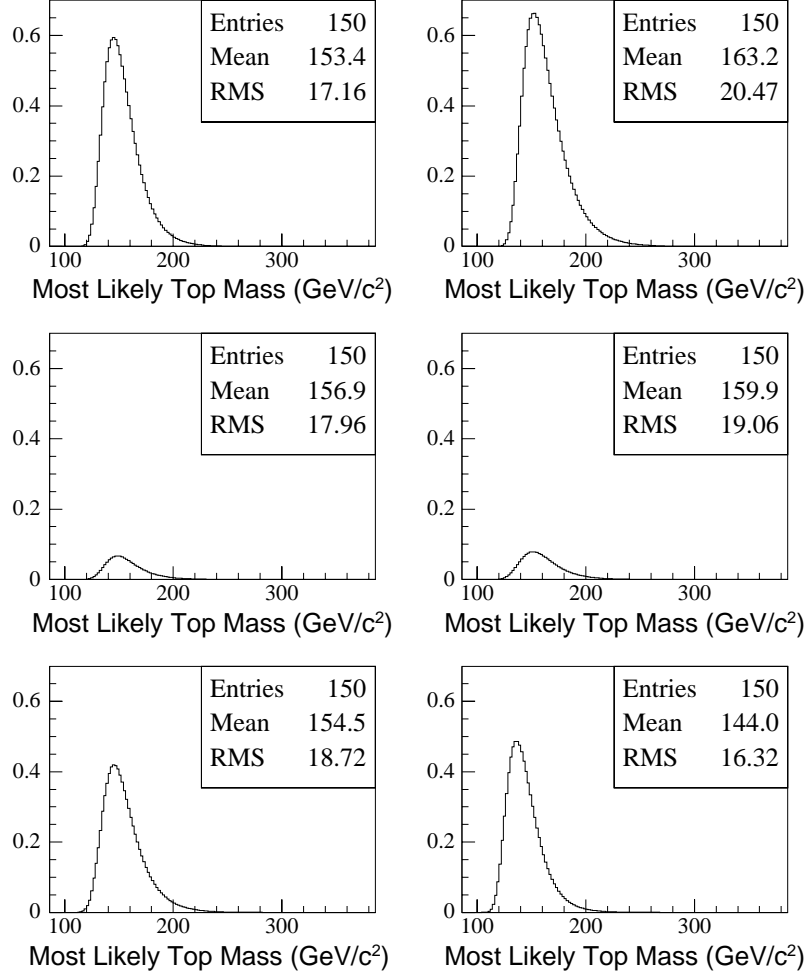


Figure 5.7: Combination likelihood distributions for data event 69808\_639398.

### 5.5.1 Monte Carlo Event Samples

The following studies were performed on standard CDF Monte Carlo  $t\bar{t}$  events generated with PYTHIA V5\_7<sup>[72]</sup> and HERWIG V5\_6<sup>[58]</sup>, followed by full CDF detector simulation using QFL V3\_59<sup>[60],[61]</sup>. Event samples were generated using input top quark masses of  $M_t^{MC} = 130, 140, 150, 160, 170, 180, 190,$  and  $220 \text{ GeV}/c^2$ .

Only events which passed the standard CDF dilepton event selection cuts were used. All jets were corrected using both the QDJSCO and DLJSCO packages (see sections 3.2 and 3.3). For each good event, all jet-lepton combinations were sampled provided the jets and leptons passed the standard CDF cuts. The jet-lepton combi-

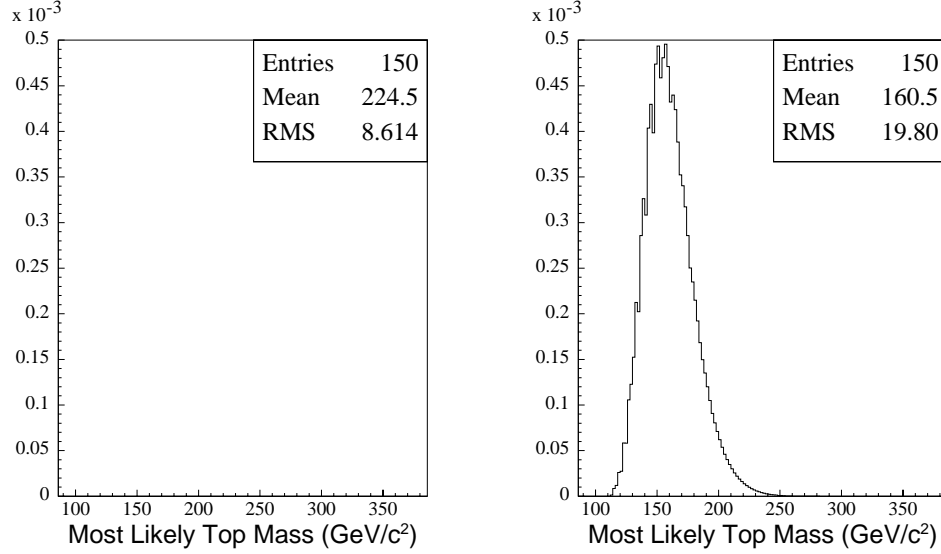


Figure 5.8: Combination likelihood distributions for data event 67581\_129896.

nation with the largest value of  $L_{comb.} \times G_{\tilde{p}_T}$  was chosen for each event. Jet clustering cone sizes of both 0.4 and 0.7 were sampled. For a cone size of 0.7 all cuts remained the same except that the jets were required to have uncorrected  $E_T > 12$  GeV.

### 5.5.2 Relative Likelihood Factors

The importance of each of the relative likelihood factors used to construct the complete likelihood,  $L_i$ , for the points in the 4-dimensional grid was studied by observing mass shifts when different combinations of factors were turned off. It was shown that each of the factors which define  $L_i$  helped to improve the agreement between the top quark mass reconstructed by the method and the top quark mass used to generate the given sample of events. See reference [87] for more details.

### 5.5.3 Studies Using Jet-Parton Matching

Several algorithms were developed and tested to match the  $b$  jets after full detector simulation to their associated partons before fragmentation. Once a suitable algorithm was established it was used to perform several preliminary studies. Both jet clustering cone sizes were employed in these analyses. The results are virtually identical except that use of a cone size of 0.7 yields a slightly higher efficiency for choosing the correct jet-parton matching. The studies mentioned in this section are documented in reference [88].



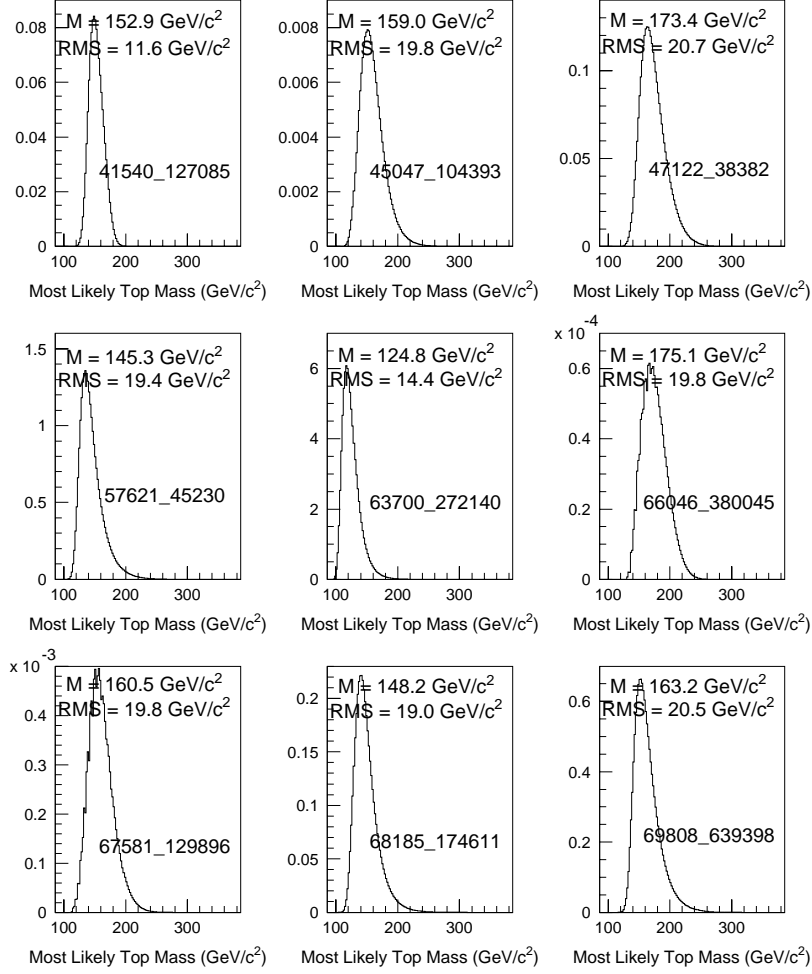


Figure 5.9: Best combination likelihood distributions for each data event.

The effects of automatically assigning the two highest  $E_T$  jets to the  $b$  quarks of a given dilepton  $t\bar{t}$  event were examined. For dilepton events with more than two jets this study showed that the efficiency for correctly matching jets to their associated partons could be increased by approximately 10 - 15% by including the third highest  $E_T$  jets in the analysis.

Another study estimated the effects of both jet energy mismeasurement and jet-parton misassignment when reconstructing the top quark mass. Since jets were the focus of this analysis and since the neutrinos escape detection, the top quark masses were reconstructed by using the  $b$  quark four-momenta after detector simulation and

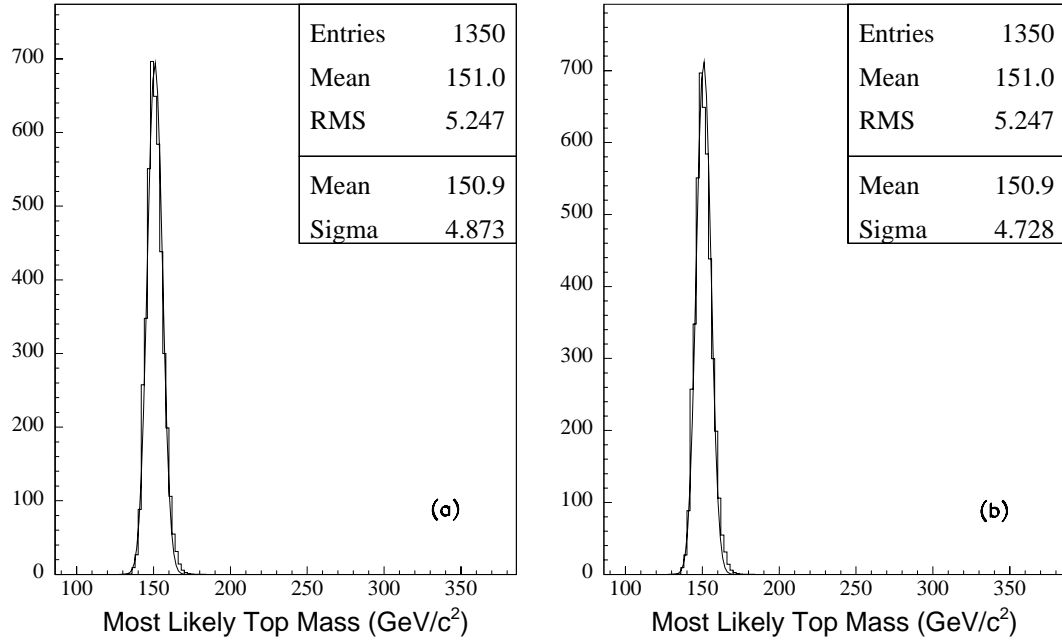


Figure 5.10: Joint likelihood distributions obtained from the data sample with (a) no constant value added to the zero entry bins and (b) a small constant value added to the zero entry bins. Gaussian fits to the distributions are also displayed, along with their mean and sigma values.

the neutrino and charged lepton four-momenta at the generator level. (Note: The results were virtually the same when the charged lepton four-momenta was taken after detector simulation). To double the statistics for a given jet-lepton combination, the mass estimates for the top and antitop quark were always combined. The top quark masses were calculated in three different ways: (1) using the "correct" jet-lepton combinations for the jets that were matched to the  $b$  quarks, (2) using the incorrect jet-lepton combinations for the jets that were matched to the  $b$  quarks (these combinations will be referred to as "flipped") and (3) using jet-lepton combinations for which at least one jet was not even matched to a  $b$  quark (these combinations will be referred to as "wrong").

The left-hand plot of figure 5.11 shows the mean values of top quark mass estimates constructed using the "correct" jet-lepton combinations as a function of generator level top quark mass. The curve shows very good linear correlation and the slope is 0.956. The slope's deviation from 1.0 is due to residual inadequacies in the jet energy corrections. The middle plot of figure 5.11 shows the mean value of reconstructed

top quark mass versus input top quark mass when "flipped" jet-lepton combinations are used. The linear correlation is significantly worse and the slope is 0.687. Finally, the right-hand plot of figure 5.11 shows the mean values of reconstructed top quark mass as a function of input top quark mass when "wrong" jet-lepton combinations are used. The linear correlation is worse than that for the "flipped" combinations and the slope is only 0.268. When the top quark mass estimates using the "correct", "flipped" and "wrong" jet-lepton combinations are combined the mean reconstructed top quark mass tends to be pulled toward a value of 160-180  $\text{GeV}/c^2$ , regardless of the value of the input top quark mass. This last effect is most likely due to the shapes of the jet and lepton momentum spectra at Tevatron collision energies, i.e. to the available phase space.

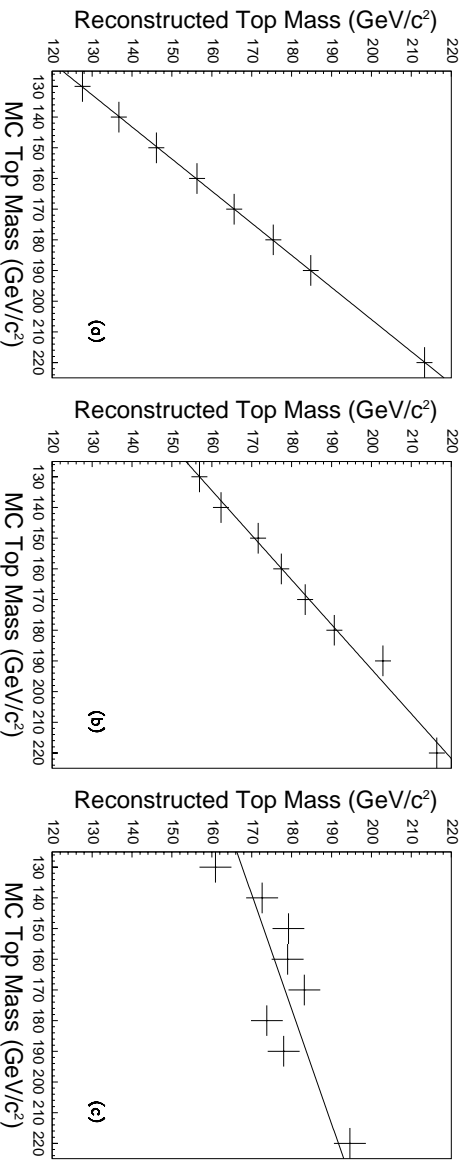


Figure 5.11: Reconstructed top quark mass vs. HERWIG Monte Carlo top quark mass for (a) "correct" jet-lepton combinations, (b) "flipped" jet-lepton combinations and (c) "wrong" jet-lepton combinations, using lepton kinematics taken directly from Monte Carlo.

The results of these studies stress the importance of using the correct jet-parton assignments when reconstructing the top quark mass. Since the jets cannot be matched back to their associated partons when using real data, the top quark mass reconstructed from data must be corrected for mismatching effects. These corrections will be discussed in the next section.

### 5.5.4 Mapping Function

To estimate how well the Dalitz-Goldstein method reconstructs the top quark mass from data, the method was tested on large samples of Monte Carlo  $t\bar{t}$  events. See section 5.5.1 for a description of these samples.

Since approximately 7 of the 9 events in the data sample are expected to be signal (see chapter 4), pseudo-experiments were constructed from all possible combinations of 7 events in a sample of given input top quark mass,  $M_t^{MC}$ . By multiplying best combination likelihood distributions together a joint likelihood distribution was constructed for each pseudo-experiment. The mean mass from each of these joint likelihood distributions was added to a histogram. The mean value,  $M_t^{rec.}$ , of the resulting histogram corresponds to the average mass reconstructed by the pseudo-experiments for the given  $M_t^{MC}$ . The R.M.S value,  $\sigma_t^{rec.}$ , of the histogram gives an estimate of the statistical error due to the reconstruction. This procedure was repeated for several values of  $M_t^{MC}$ . Figure 5.12 shows the histograms of pseudo-experiment masses for an input top quark mass range of  $130 < M_t^{MC} < 220 \text{ GeV}/c^2$ . The R.M.S. values of the histograms become larger with increasing input top quark mass. The histograms are well approximated by Gaussian distributions and these distributions, along with their associated mean and sigma values, are also displayed in the figure.

The  $M_t^{rec.}$  values were plotted as a function of  $M_t^{MC}$  and a linear fit was performed on these points by using the  $M_t^{rec.}$  values as the means and the  $\sigma_t^{rec.}/\sqrt{N/7}$  values as the uncertainties on the means, where N is the number of events in a sample of given  $M_t^{MC}$ . For an explanation of this choice for the uncertainty on the means see appendix C. We refer to the resulting linear parameterization of  $M_t^{rec.}$  vs.  $M_t^{MC}$  as a "mapping function". Its slope quantifies how well the fitter reconstructs the true top quark mass. Using HERWIG Monte Carlo events, the  $H_t$  cut and a jet clustering cone size of 0.4 for an input top quark mass range of  $130 < M_t^{MC} < 220 \text{ GeV}/c^2$ , we derived a mapping function of the form:

$$M_t^{rec.} = 62.308 + M_t^{MC} \times 0.59048 \quad (5.18)$$

where all masses are in units of  $\text{GeV}/c^2$  and the covariance matrix elements are:  $v_{11} = 19.1$ ,  $v_{12} = -0.115$  and  $v_{22} = 0.000709$ . The  $\chi^2$  of the fit is 2.4. The systematic error for choosing a linear parameterization of  $M_t^{rec.}$  vs.  $M_t^{MC}$  will be discussed in

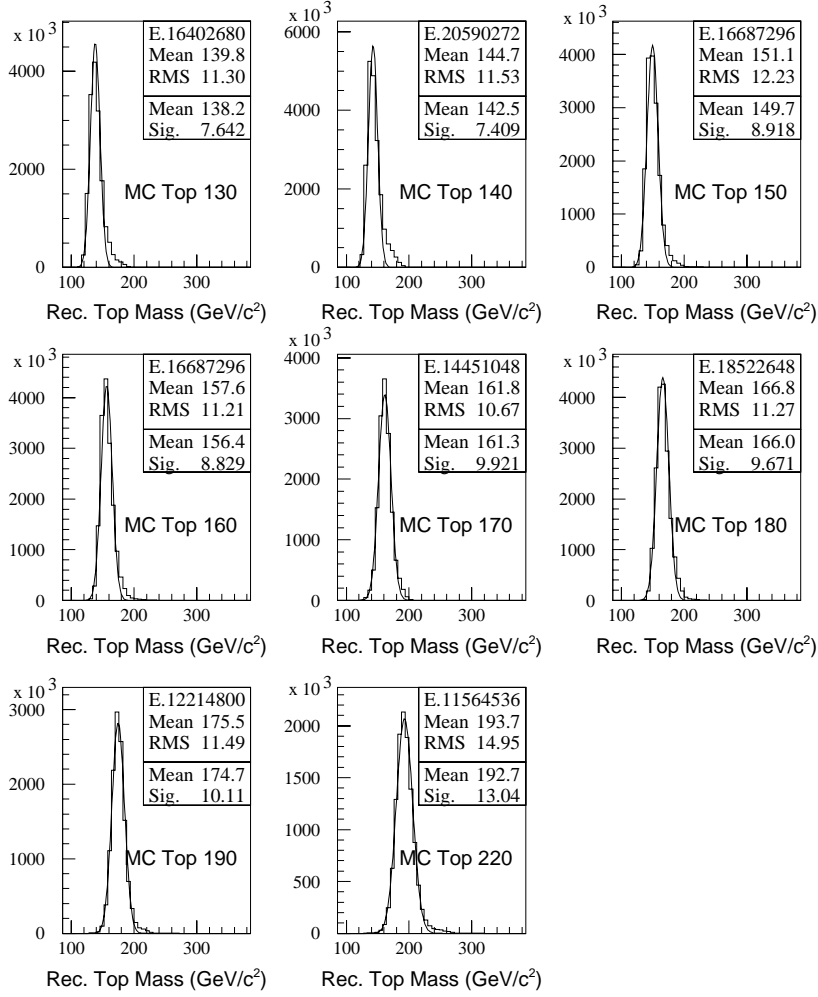


Figure 5.12: Distributions of reconstructed  $M_t$  obtained from pseudo-experiments.

section 5.8.4. A graphical representation of the mapping function with its corridor of errors is shown in figure 5.13. Equation 5.18 shows that the slope of the mapping functions is 0.59048. This deviation from 1.0 is due to a variety of factors including jet-parton mismatching and jet energy uncertainty (see section 5.5.3). Because the correlation between  $M_t^{rec.}$  and  $M_t^{MC}$  is not perfect, the mapping function must be used to correct the top quark mass reconstructed from data.

To test the validity of our mapping function we repeated the procedure described above by using other criteria besides the best likelihood method to choose the best jet-lepton combination from each event of a given pseudo-experiment to form the joint

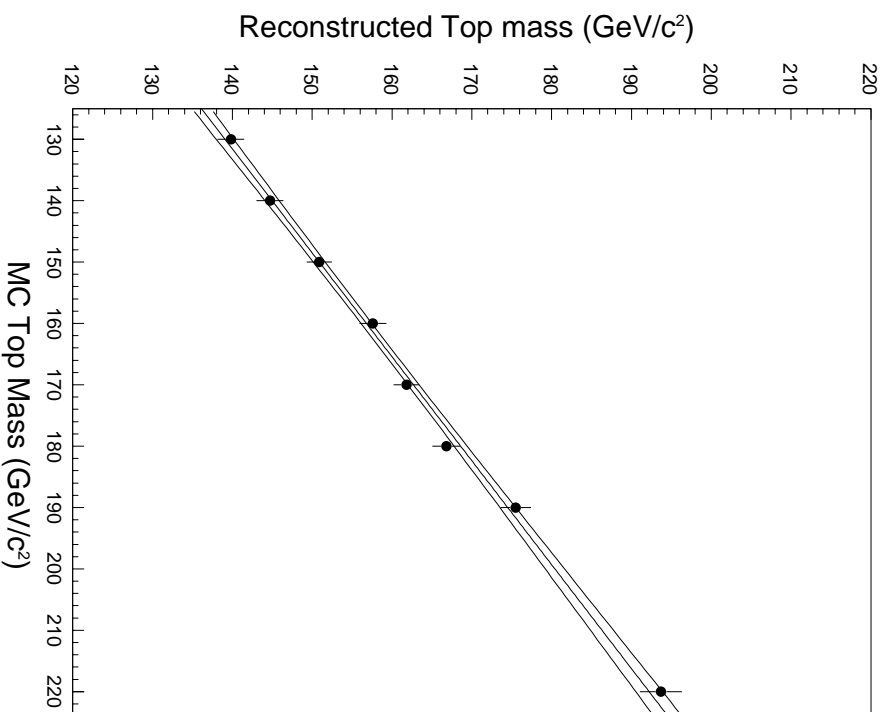


Figure 5.13: The mapping function and its corridor of errors.

likelihood distribution. Three new mapping functions were constructed, depending on three new choices for the best jet-lepton combinations: (i) those for which the two jets used by the fitter were correctly matched to the  $b$  quarks (these will be referred to as "correct" combinations) (ii) those for which the two jets used by the fitter were matched to  $b$  quarks, but not to the right ones (these will be referred to as "flipped" combinations) and (iii) those for which at least one of the two jets used in the fitter were not even matched to a  $b$  quark (these will be referred to as "wrong" combinations). These choices for the jet-lepton combinations are the same as those used in the jet-parton matching study mentioned in section 5.5.3.

Histograms of mean masses, analogous to those shown in figure 5.12, were constructed for the "correct", "flipped", and "wrong" jet-lepton combinations. Like the histograms shown in figure 5.12, these new histograms were also approximately

Gaussian in shape and had R.M.S. values which increased with increasing input top quark mass. In general, the R.M.S. values were smallest for the histograms constructed from "correct" jet-lepton combinations and largest for those constructed from the "wrong combinations. The left-hand plot of Figure 5.14 shows the mapping function derived from "correct" jet-lepton combinations. The slope is 0.752. This slope is not as close to 1.0 as the slope of the left-hand plot of figure 5.11. This is because the top quark masses of the study described in section 5.5.3 were reconstructed using generator level neutrino kinematics, whereas those in this analysis were effectively reconstructed using neutrino kinematics determined by the fitter. The middle plot of Figure 5.14 shows the mapping function derived from "flipped" combinations. As expected, it shows poorer correlation between reconstructed mass and input mass than the mapping function derived from correct combinations, and its slope is only 0.45. The right-hand plot of Figure 5.14 shows the mapping function derived from "wrong" jet-lepton combinations. Not surprisingly, its slope of 0.35 is even smaller than that for the "flipped" combinations.

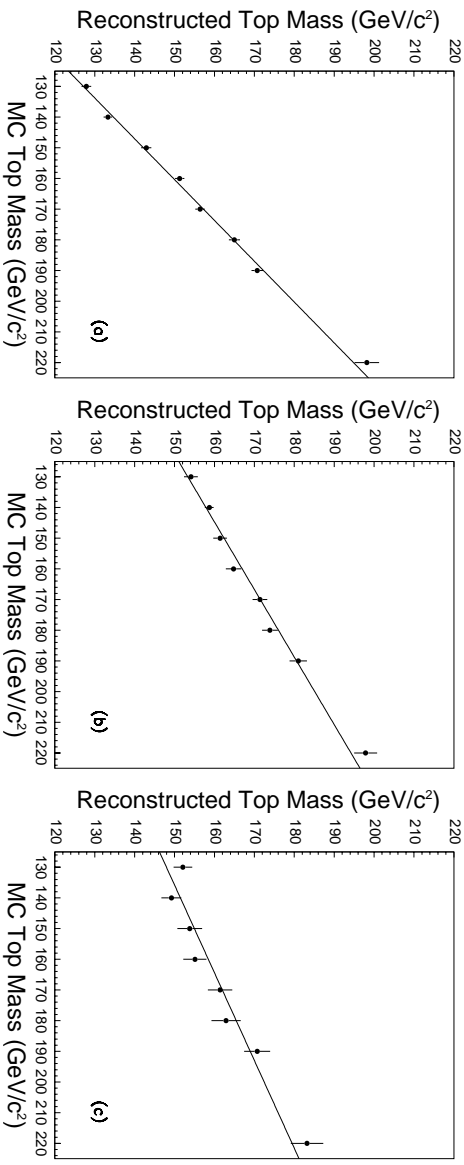


Figure 5.14: Reconstructed top quark mass vs. HERWIG Monte Carlo top quark mass for (a) "correct" jet-lepton combinations, (b) "flipped" jet-lepton combinations and (c) "wrong" jet-lepton combinations, using lepton kinematics determined by the top mass fitter.

The slope of the mapping function used to correct the top quark mass reconstructed from data (i.e. the mapping function derived from best likelihood jet-lepton combinations) is 0.595. This is less than the slope of the mapping function derived

from "correct" jet-lepton combinations since the best likelihood method does not always choose the correct jet-lepton combination. However, it is considerably higher than those of the mapping functions derived from the "flipped" and "wrong" combinations. The best likelihood method chooses the correct jet-lepton combinations approximately 65-70 % of the time.

Using the best likelihood method, a total of eight different mapping functions were derived by varying the choice of Monte Carlo generators (HERWIG or PYTHIA), kinematic cuts ( $H_T$  cut applied or not applied) and jet clustering cone sizes (0.4 or 0.7). A comparison of the reconstructed top quark masses obtained from each mapping function will be presented in section 6.1. Unless otherwise stated, the mapping function derived by using HERWIG events, the  $H_T$  cut and a jet clustering cone size of 0.4 (see equation 5.18) will be used throughout this document since it conforms most closely to CDF off-line analysis standards.

### 5.5.5 Effect of Background Events

As mentioned in section 4.7, we expect  $1.3 \pm 0.3$  ( $2.4 \pm 0.5$ ) of the 9 data events to come from background if the  $H_T$  cut is (is not) applied. Although the expected contribution from background is small, its effect on the joint likelihood distribution needed to be quantified so that the top quark mass reconstructed from data could be appropriately corrected.

For these background studies we used the signal event pseudo-experiments mentioned in section 5.5.4, along with a sample of 98  $W^+W^-$  Monte Carlo events generated by VECBOS<sup>[74]</sup>. To find the shift in reconstructed top quark mass due to background when the  $H_T$  cut is applied, we formed joint likelihood distributions out of 8 events by multiplying each 7 signal event joint likelihood distribution by the best combination likelihood distribution of each event in the  $W^+W^-$  Monte Carlo sample. For a given input top quark mass,  $M_t^{MC}$ , the mean mass obtained from a given 7 signal event joint likelihood distribution was subtracted from the mean mass obtained from each of the 98 possible 8-event joint likelihood distributions for this pseudo-experiment. These 98 mass shifts were calculated for each 7-event pseudo-experiment and plotted on a single histogram. The resulting histogram was fitted nicely to a Gaussian distribution. The mean,  $M_{shift}^{HT}$ , of the Gaussian distribution gives the average mass shift expected for the given top quark mass,  $M_t^{MC}$ , when the



$H_T$  cut is applied. (Note: This shift is a slightly underestimated since  $1.3 \pm 0.3$ , rather than 1.0, background events are expected. However, our choice of systematic error for this procedure should be conservative enough to account for this discrepancy. See section 5.8.7). This procedure was repeated for a wide range of possible top quark mass values:  $130 < M_t^{MC} < 220 \text{ GeV}/c^2$ ). The three plots in Figure 5.15 show the mass shift distributions for  $M_t^{MC} = 130, 160$  and  $220 \text{ GeV}/c^2$  when one background event is expected.

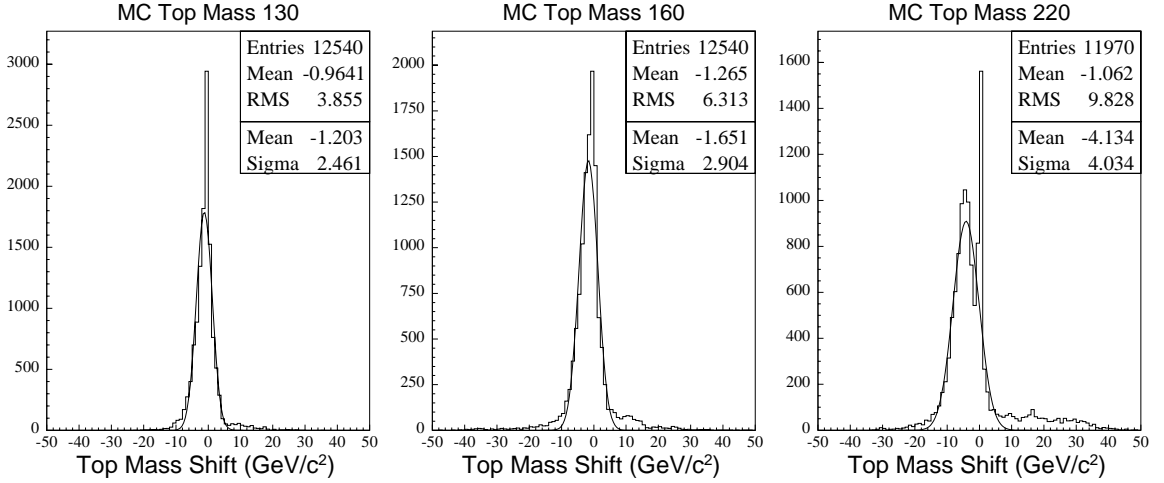


Figure 5.15: Shifts in reconstructed top mass when 1 out of 8 pseudo-experiment events used to form each joint likelihood distribution is a  $W^+W^-$  event. From left to right the plots refer to HERWIG Monte Carlo top quark masses of 130, 160 and 220  $\text{GeV}/c^2$ , respectively. Gaussian fits to these histograms are also shown, along with their means and sigmas.

The  $M_{shift}^{HT}$  values due to background were plotted as a function of  $M_t^{MC}$ . A linear fit was performed on these points to find the parameterization of the mean mass shift as function of generated top quark mass when the  $H_T$  cut is applied. The parameterization in the range  $130 < M_t^{MC} < 220 \text{ GeV}/c^2$ , is:

$$M_{shift}^{HT} = 2.7672 - M_t^{MC} \times 0.02859 \quad (5.19)$$

where all masses are in  $\text{GeV}/c^2$ . This parameterization is plotted in the left-hand plot of figure 5.16. We also repeated this procedure by using the means of the mass shift histograms themselves, rather than the means of the Gaussian fits, when calculating the parameterization. The mass shifts found in this manner tend to be smaller than those obtained by using Gaussian fits. See the right-hand plot of figure 5.16.

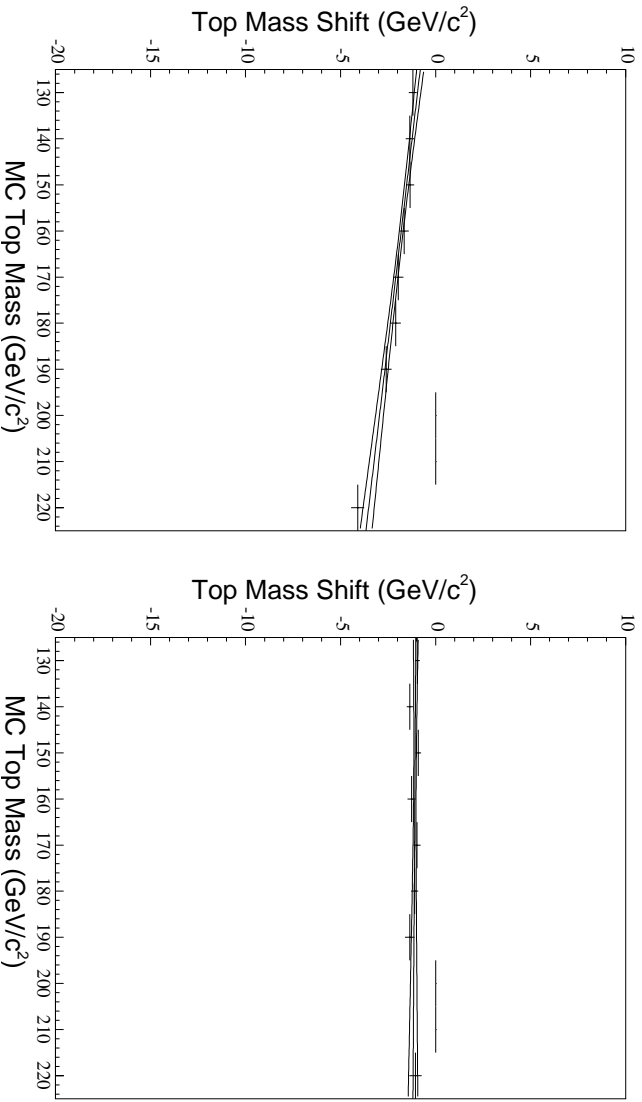


Figure 5.16: Parameterization of the mean mass shifts for Monte Carlo top quark masses of 130, 140, 150, 160, 170, 180, 190 and 220  $\text{GeV}/c^2$ , when 1 out of 8 pseudo-experiment events used to form each joint likelihood distribution is a  $W^+W^-$  event. The left-hand plot uses the means of Gaussian fits to the mass shift distributions.

This procedure was repeated for the case where the  $H_T$  cut is not applied so that the expected number of background events is approximately 2. In this case, each 7 signal event joint likelihood distribution was multiplied by the best combination likelihood distributions from all possible combinations of 2  $W^+W^-$  events from the background sample. The rest of the procedure remained the same. Figure 5.17 shows the mass shift distributions for  $M_t^{MC} = 130, 160$  and  $220 \text{ GeV}/c^2$ . The parameterization of the mean mass shift when the  $H_T$  cut is not applied is:

$$M_{shift}^{no HT} = 3.7331 - M_t^{MC} \times 0.4355 \quad (5.20)$$

where all masses are in  $\text{GeV}/c^2$ . The left-hand plot of Figure 5.18 shows a plot of this parameterization. The right-hand plot of Figure 5.18 shows the parameterization when the means of the mass shift histograms are used instead of the Gaussian means.

In general, the shifts in reconstructed top quark mass due to the  $W^+W^-$  events were found to be quite small and of the order of a few  $\text{GeV}/c^2$ . The shifts were negative which means that the mass measured from data must be shifted upward to

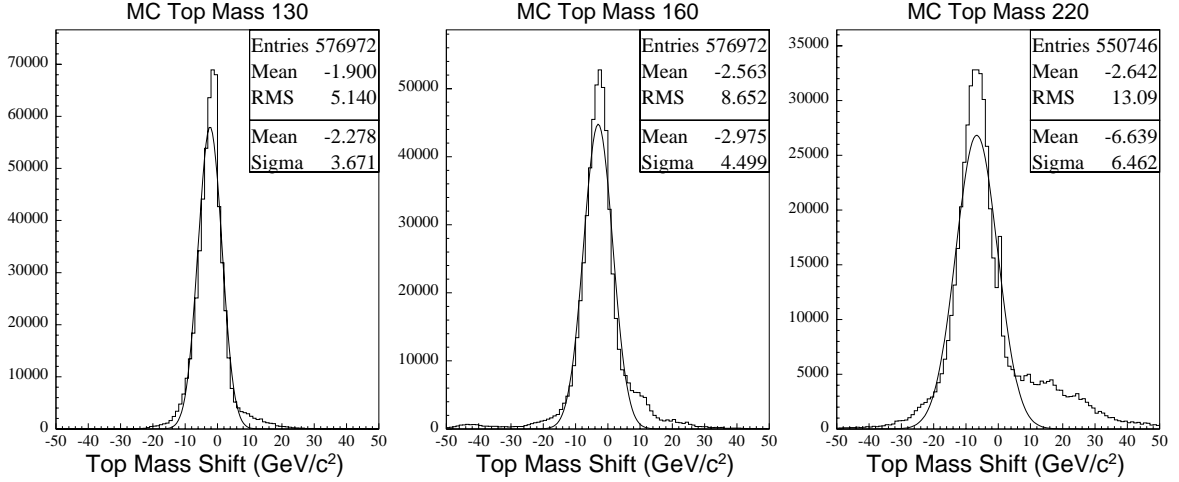


Figure 5.17: Shifts in reconstructed top mass when 2 out of 9 pseudo-experiment events used to form each joint likelihood distribution are  $W^+W^-$  events. From left to right the plots refer to HERWIG Monte Carlo top quark masses of 130, 160 and 220 GeV/c², respectively. Gaussian fits to these histograms are also shown, along with their means and sigmas.

obtain the true top quark mass. In addition to  $W^+W^-$  events, we tried other sources of background, including  $Z^0 + jets$  events and found the resulting mass shifts to be comparable or even smaller. The systematic error on the expected mass shift due to background will be described in section 5.8.7.

## 5.6 Application to Run 1 Data

This section illustrates our measurement of the top quark mass from Run 1 dilepton events, using the Dalitz-Goldstein mass fitting technique and the corrections described in section 5.5. The mapping function applied here was constructed by using HERWIG Monte Carlo events, the  $H_T$  cut and a jet clustering cone size of 0.4.

The best combination likelihood distributions from each of the 8 data events that pass the  $H_T$  cut were multiplied together to form a joint likelihood distribution. Figure 5.19 shows a plot of this distribution. The mean value,  $M_t^{data}$ , of the joint likelihood distribution gives a first estimate of the top quark mass. We measured:

$$M_t^{data} = 153.4 \text{ GeV}/c^2 \quad (5.21)$$

The studies mentioned in section 5.5.5 show that  $M_t^{data}$  must be corrected for background effects. Using our previously calculated parameterization of the background

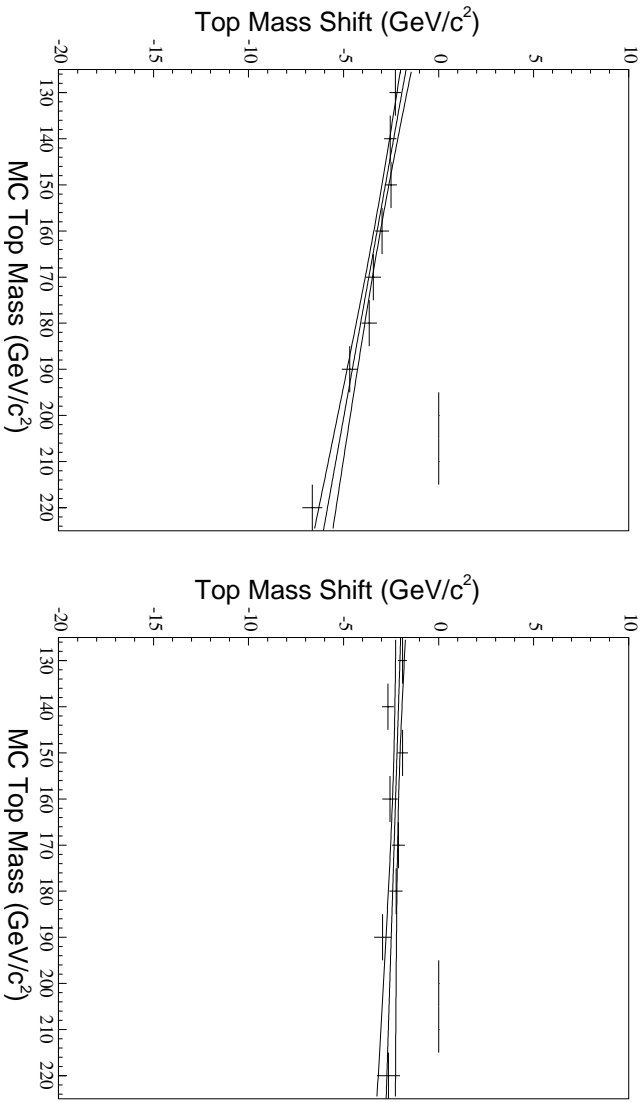


Figure 5.18: Parameterization of the mean mass shifts for MC Monte Carlo top quark masses of 130, 140, 150, 160, 170, 180, 190 and 220  $\text{GeV}/c^2$ , when 2 out of 9 pseudo-experiment events are  $W^+W^-$  events. The left-hand plot uses the means of Gaussian fits to the mass shift distributions.

shift as a function of top quark mass, we find the background corrected top quark mass to have the value:

$$M_t^{bg\ corrected} = 155.1 \text{ GeV}/c^2 \quad (5.22)$$

As shown in section 5.5.4, this mass must still be corrected, via the mapping function, for effects like jet-parton mismatching and jet energy mismeasurement.  $M_t^{bg\ corrected}$  is superimposed as a horizontal line onto the mapping function shown in figure 5.20. The true mass is found by projecting the intersection point of the horizontal line and the mapping function onto the  $M_t^{MC}$  axis. The fully corrected top quark mass is:

$$M_{top} = 157.1 \text{ GeV}/c^2 \quad (5.23)$$

The calculation of the statistical and systematic uncertainties due to our method will be described in the following two sections.

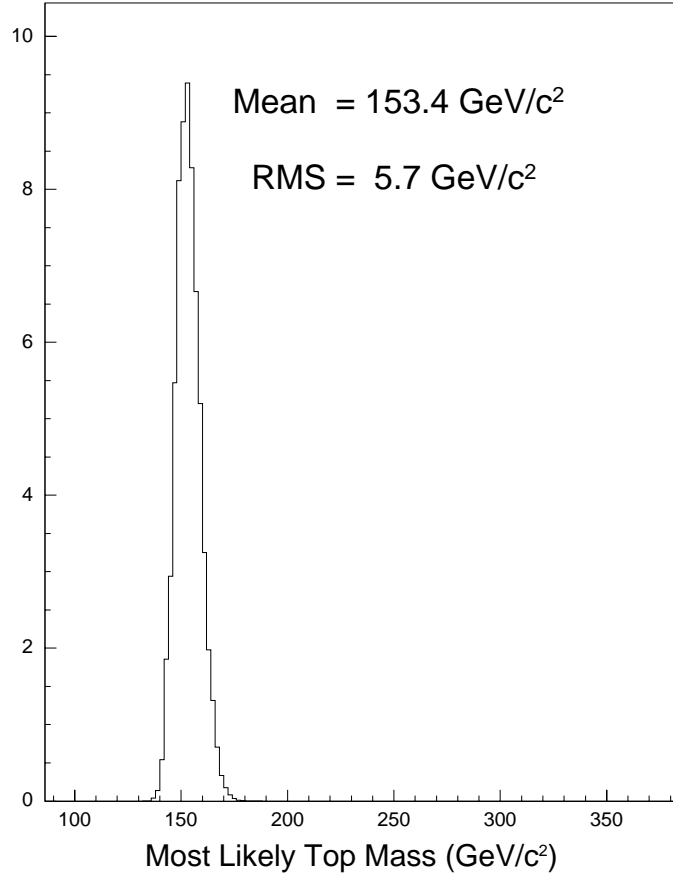


Figure 5.19: Joint Likelihood distribution for Run 1 dilepton data events when the  $H_T$  cut has been applied.

## 5.7 Statistical Errors

The procedure used to determine the statistical uncertainty of the top quark mass reconstructed by our fitting technique will be described in detail in this section. A first estimate of this error is determined solely by the data events. However, it must be corrected for a variety of effects including the low statistics of the data sample itself. Use of HERWIG events, the  $H_T$  cut and a jet clustering cone size of 0.4 will be implied throughout this section.

A first estimate of the statistical error was obtained from the R.M.S. value,  $\sigma_{stat.}^{data}$ , of the joint likelihood distribution constructed from the best combination likelihood distributions of each of the 8 data events that pass the  $H_T$  cut. This estimate is

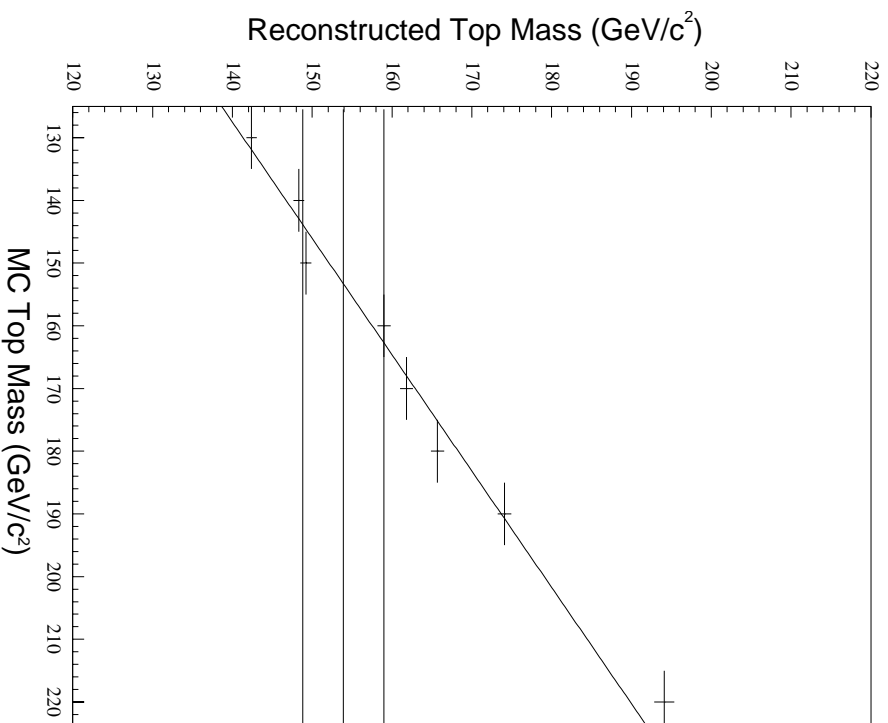


Figure 5.20: The mapping function derived from HERWIG Monte Carlo pseudo-experiments and its intersection with the mean mass of the joint likelihood distribution constructed from data. The  $\pm 1\sigma$  lines of the joint likelihood distribution are also shown.

statistical since it is proportional to  $1/\sqrt{N}$ , where  $N$  is the number of events in the data sample. The statistical error also depends on the mass of the top quark, as was observed by using the signal event pseudo-experiments described in section 5.5.4. For a given input top quark mass,  $M_t^{MC}$ , the R.M.S. of each joint likelihood distribution was plotted on a histogram. The mean of the resulting histogram is a first estimate of the average statistical error of the method for a top quark mass of  $M_t^{MC}$ . Figure 5.21 shows these histograms for generated top quark masses of 140, 150, 160 and 170  $\text{GeV}/c^2$ . From these plots it is evident that the average statistical error increases with increasing top quark mass. Figure 5.22 shows a linear parameterization of the

average statistical error as a function of  $M_t^{MC}$  for top quark masses covering the range:  $130 < M_t^{MC} < 220 \text{ GeV}/c^2$ . The slope is clearly greater than zero. The R.M.S. of the joint likelihood distribution constructed from data is:

$$\sigma_{stat.}^{data} = 5.2 \text{ GeV}/c^2 \quad (5.24)$$

This number is quite close to the average statistical error predicted by the pseudo-experiments for a top quark mass of  $160 \text{ GeV}/c^2$  (see histogram (c) of figure 5.21).

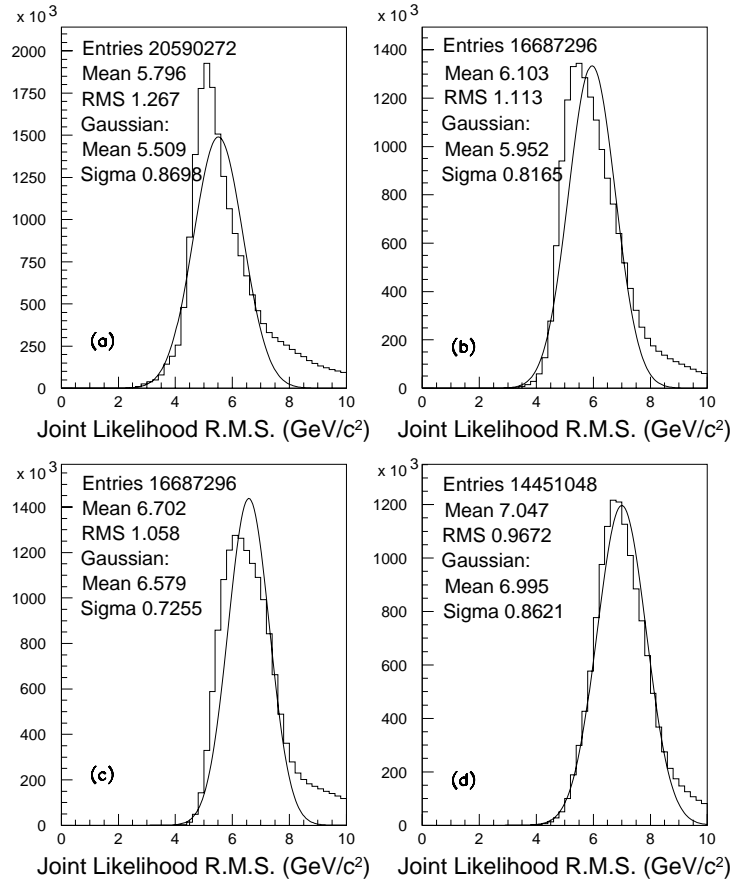


Figure 5.21: R.M.S. values of joint likelihood distributions that were constructed from 7-event pseudo-experiments generated by HERWIG Monte Carlo using top quark masses of (a) 140 (b) 150 (c) 160 and (d) 170  $\text{GeV}/c^2$ . Gaussian fits to these histograms, along with their means and sigmas, are also displayed.

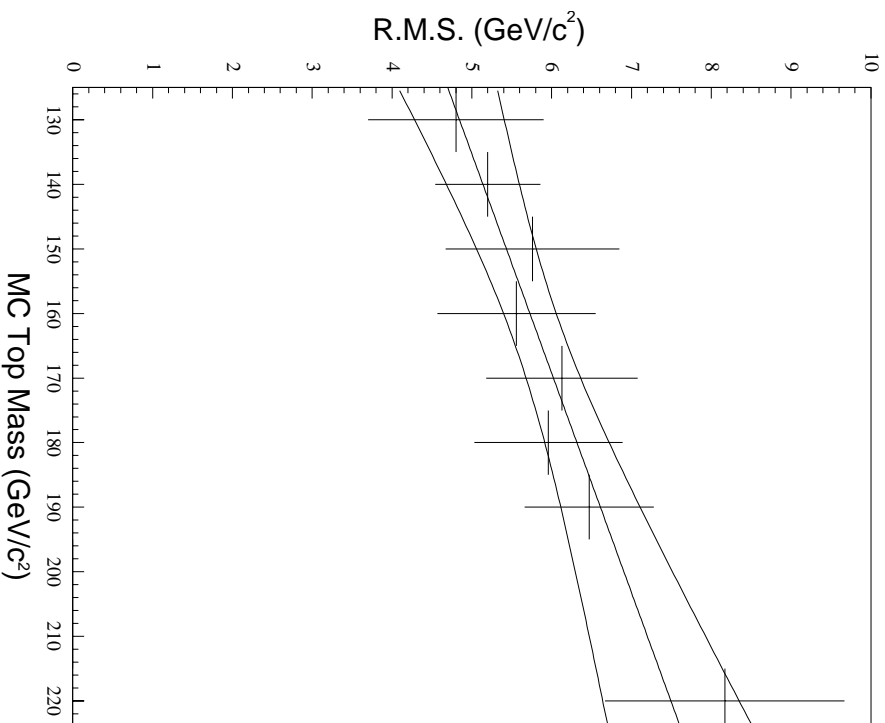


Figure 5.22: Linear parameterization of the mean R.M.S. values of joint likelihood distributions for pseudo-experiments generated by HERWIG Monte Carlo over the top quark mass range:  $130 < M_t^{MC} < 220 \text{ GeV}/c^2$ .

In section 5.5.4 it was shown that the top quark mass reconstructed from data must be corrected, via a mapping function, for a variety of effects including jet-parton mismatching. The statistical error must be corrected by the mapping function for the same reasons. To perform the latter correction we first corrected the top quark mass for the expected shift due to background and superimposed this result as a horizontal line on the mapping function, as outlined in section 5.6. Then we superimposed the statistical error measured from data onto the mapping function by drawing a corridor of errors, of width  $\sigma_{stat}^{data}$ , about the horizontal corrected mass line. The corrected statistical error,  $\sigma_{stat}^{corrected}$ , was found by projecting the width of the corridor of errors



onto the horizontal axis, via the mapping function line. Figure 5.23 illustrates this procedure. The corrected statistical error is:

$$\sigma_{stat.}^{corrected} = 9.6 \text{ GeV}/c^2 \quad (5.25)$$

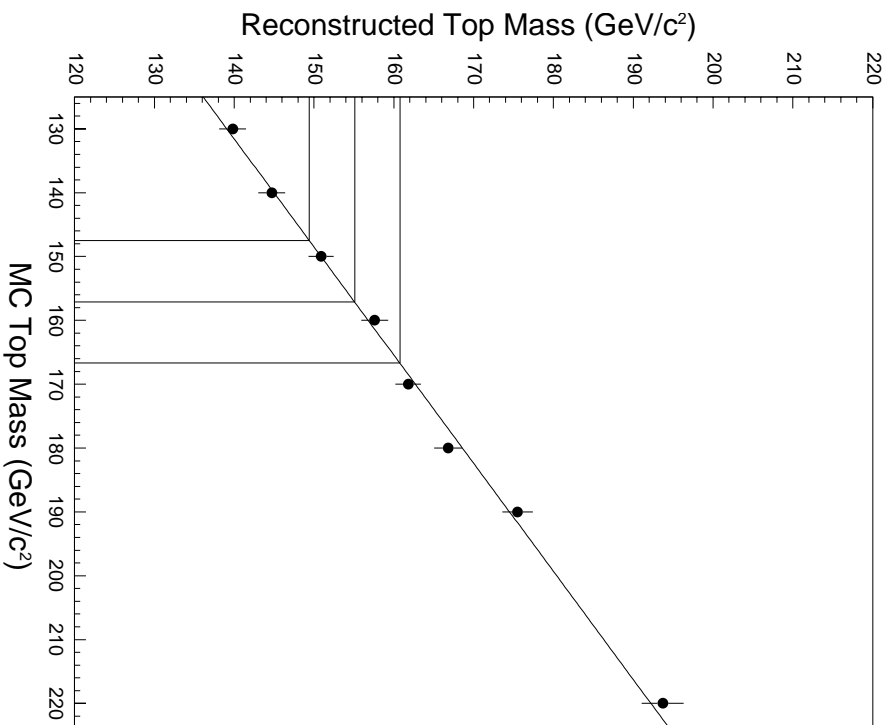


Figure 5.23: Using the mapping function derived from HERWIG Monte Carlo events to correct the statistical error.

To verify that our definition of the statistical error is self-consistent we applied the fitting technique to 8-event pseudo-experiments similar to the 7-event pseudo-experiments described in section 5.5.4. Figure 5.24 shows the results for a generated top quark mass of  $M_t^{MC} = 160 \text{ GeV}/c^2$ . The upper plot is a distribution of the fully reconstructed top quark masses,  $M_t^{fitter}$ , for each pseudo-experiment after the mapping function and background shifts have been applied. The mean of the distribution, being  $159.3 \text{ GeV}/c^2$ , is in close agreement with the generated top quark mass. The

middle plot shows a distribution of pulls defined as  $(M_t^{fitter} - M_t^{MC})/\sigma_{stat.}^{corrected}$ . The mean of the pull distribution is close to zero but the R.M.S. of the distribution is 1.13, indicating that  $\sigma_{stat.}^{corrected}$  underestimates the statistical error. The lower plot of figure 5.24 shows a distribution of the  $\sigma_{stat.}^{corrected}$  values for each pseudo-experiment. When the mean of this plot is multiplied by 1.13 the result is 11.6. This number is very close to 11.8, the R.M.S. of the reconstructed mass distribution shown in the uppermost plot.

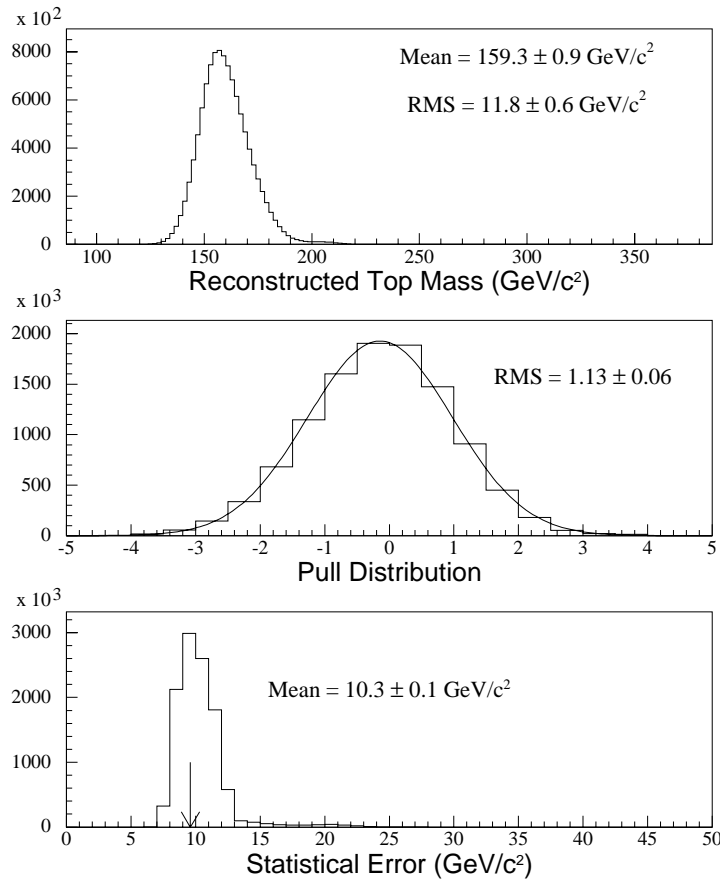


Figure 5.24: Application of the complete mass fitting technique, including mapping function corrections, to a set of 8-event pseudo-experiments generated by HERWIG Monte Carlo using a top quark mass of 160 GeV/c².

To verify that the residual error not accounted for by  $\sigma_{stat.}^{corrected}$  is itself statistical, we created more plots like the ones shown in figure 5.24, but with event sample sizes different from 8. Figures 5.25, 5.26, 5.27 and 5.28 show these plots for event sample

sizes of 4, 7, 10 and 16 events, respectively. Table 5.1 shows a table of the widths of the pull distributions from each figure. It is evident that the width approaches 1.0 as the number of events in the sample increases and that a sample size of 16 events is large enough to essentially eliminate the residual error contribution.

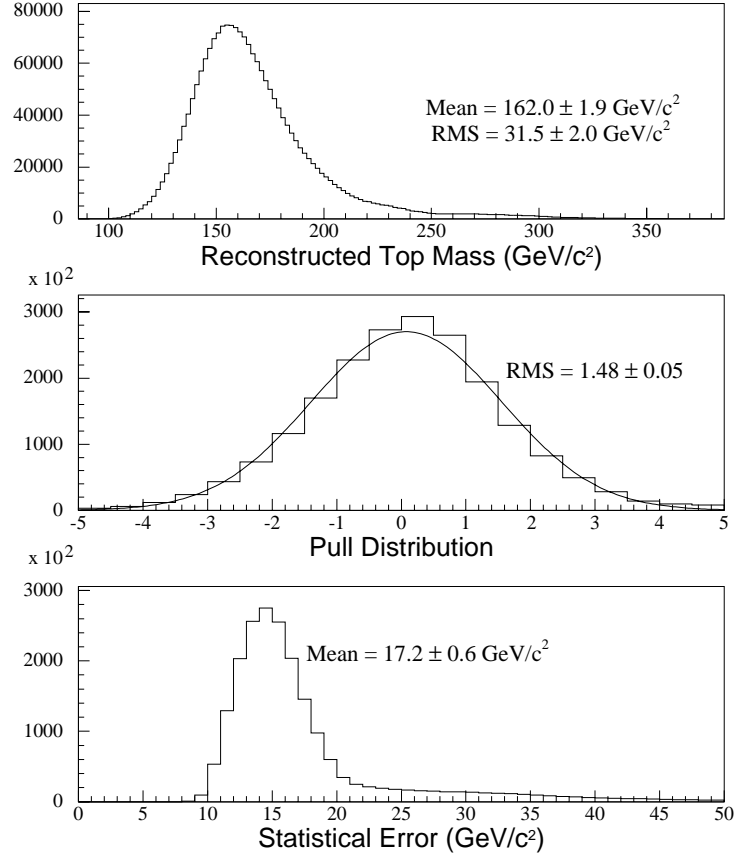


Figure 5.25: Application of the complete mass fitting technique, including mapping function corrections, to a set of 4-event pseudo-experiments generated by HERWIG Monte Carlo using a top quark mass of 160 GeV/c².

A similar residual statistical error effect has been observed by applying other top quark mass fitting techniques, including the "neutrino weighting method", which was recently approved by the CDF Collaboration. (This method will be briefly described in section 6.3.3. See reference [89] for complete details). The proponents of the neutrino weighting method also found a residual statistical error that approaches zero with increasing statistics. To be consistent with their solution to this underestimation

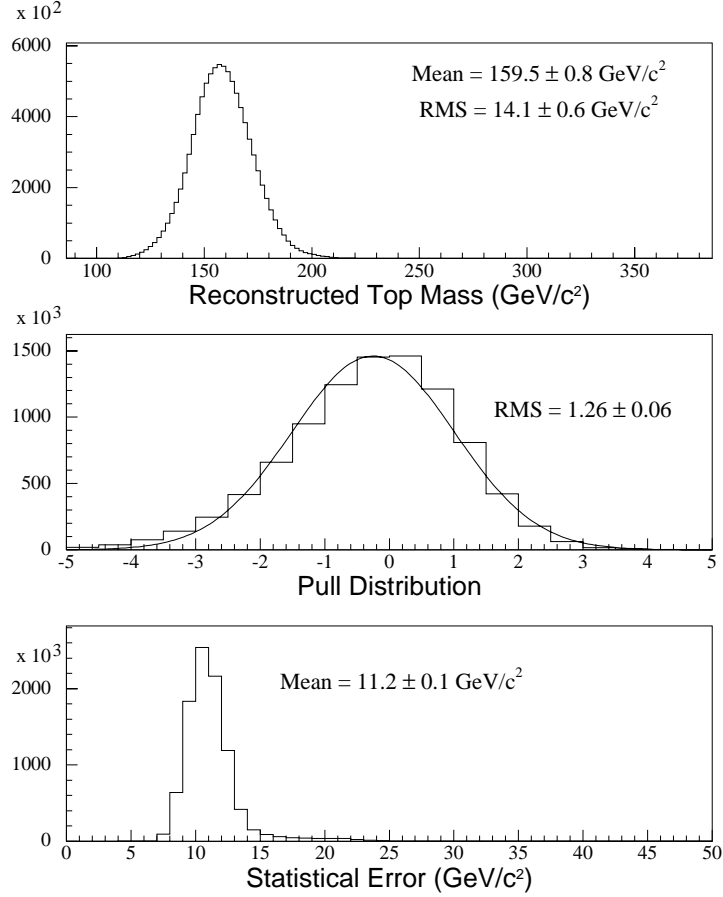


Figure 5.26: Application of the complete mass fitting technique, including mapping function corrections, to a set of 7-event pseudo-experiments generated by HERWIG Monte Carlo using a top quark mass of 160 GeV/c<sup>2</sup>.

problem we simply multiply  $\sigma_{stat.}^{corrected}$  by 1.13, the width of our pull distribution for 8 events. We quote our final statistical error as:

$$\sigma_{stat.} = 10.9 \text{ GeV}/c^2 \quad (5.26)$$

## 5.8 Systematic Errors

This section outlines our calculation of the systematic uncertainty on the top quark mass reconstructed by the fitter. Mass shifts were calculated for a variety of effects like jet energy mismeasurement and initial and final state radiation. In calculating these shifts we tried to follow well established procedures used by previous analyses wherever possible.

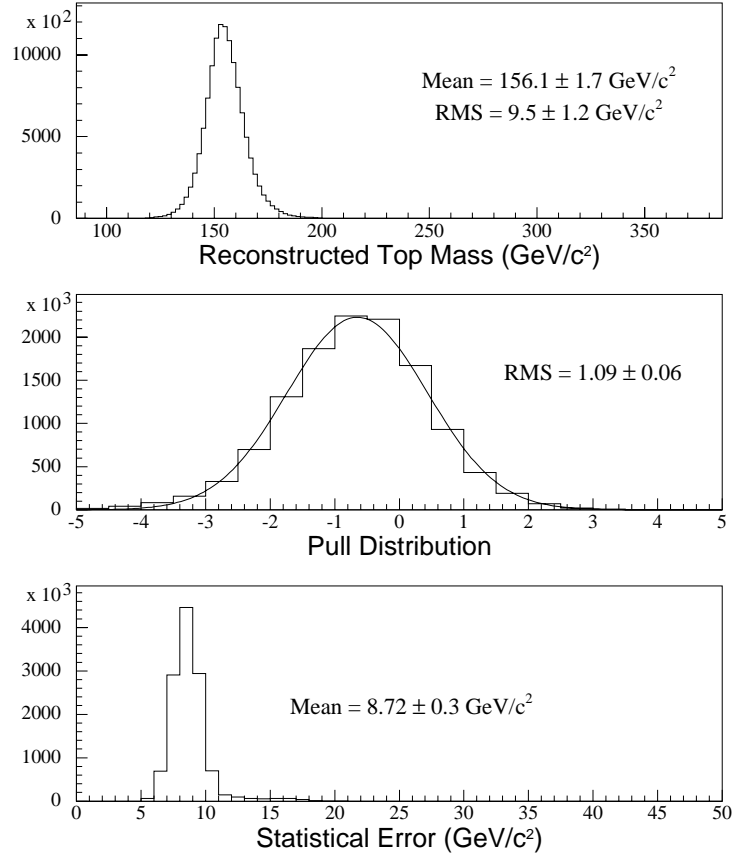


Figure 5.27: Application of the complete mass fitting technique, including mapping function corrections, to a set of 10-event pseudo-experiments generated by HERWIG Monte Carlo using a top quark mass of 160 GeV/c<sup>2</sup>.

### 5.8.1 Jet Energy Scale

The most dominant systematic error arises from the uncertainty in the jet energies measured by the CDF detector. As mentioned in sections 3.2 and 3.3, the jet energies must be corrected for both detector and physics effects. Even after these corrections the jet energies remain uncertain by as much as 10%. According to reference [90], the uncertainty on the corrected  $E_T$  of a jet whose uncorrected  $E_T$  is 40 GeV typically ranges between 3.4 and 5.6%.

To determine the systematic error from jet energy uncertainty, we followed the procedure mentioned in reference [90]. For a given pseudo-experiment of given generated top quark mass,  $M_t^{MC}$ , we calculated six uncertainties for each jet energy due to

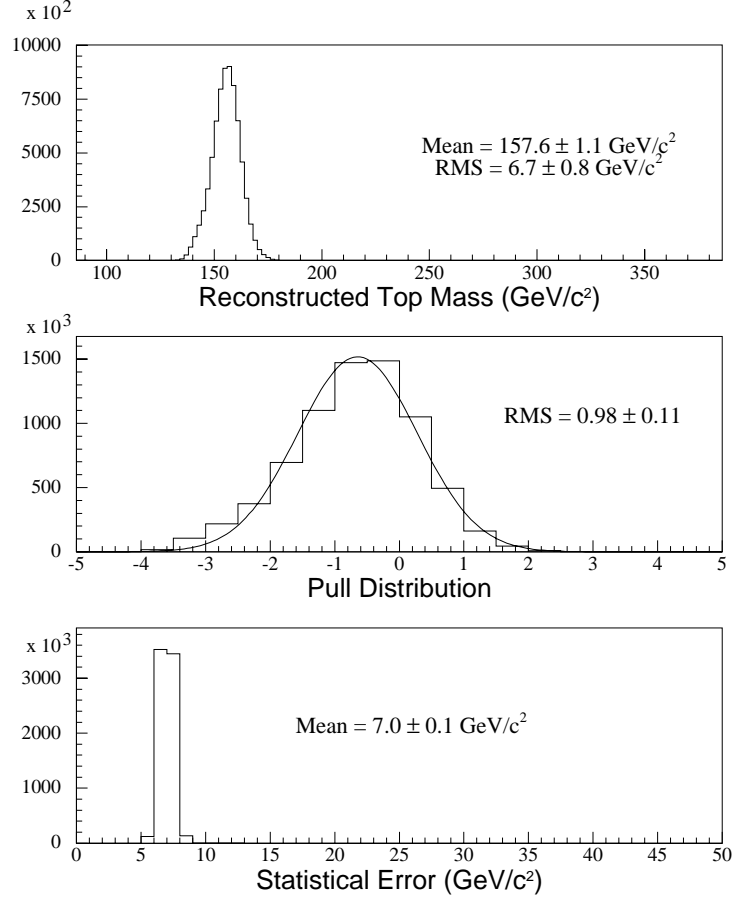


Figure 5.28: Application of the complete mass fitting technique, including mapping function corrections, to a set of 16-event pseudo-experiments generated by HERWIG Monte Carlo using a top quark mass of  $160 \text{ GeV}/c^2$ .

the following six sources: (1) Absolute jet energy scale, (2) relative jet energy scale, (3) calorimeter stability, (4) energy deposited by underlying events and multiple interactions, (5) soft gluons radiated in the  $(\phi, \eta)$  annular region of,  $0.4 < R < 1.0$ , about the jet and (6) energy lost outside of a cone of radius  $R = 1.0$  about the jet. These uncertainties were then added together in quadrature for each jet to determine a total uncertainty on each jet energy in the given pseudo-experiment. The systematic error due to jet energy uncertainty for the given pseudo-experiment was calculated as the shift in reconstructed mass when the total jet uncertainties were either added or subtracted from their respective measured jet energies. This procedure was repeated for several pseudo-experiments in the range:  $130 < M_t^{MC} < \text{GeV}/c^2$ . For a top quark

Number of events in data sample	Width of pull distribution
4	$1.48 \pm 0.05$
7	$1.26 \pm 0.06$
8	$1.13 \pm 0.06$
10	$1.09 \pm 0.06$
16	$0.98 \pm 0.11$

Table 5.1: Variation of pull distribution width with number of data events.

mass of  $160 \text{ GeV}/c^2$  we found the average mass shift due to jet energy uncertainty to be  $\pm_{1.3}^{2.6} \text{ GeV}/c^2$ . We quote this result as our systematic error due to the jet energy scale.

Figure 5.29 shows the average positive and negative mass shifts due to jet energy uncertainty as a function of generated top quark mass. The positive shifts tend to be higher than the negative shifts. This asymmetry arises from two uncorrelated effects. First, the jet energy uncertainties themselves are slightly lower for energy shifts down than for energy shifts up. This effect is shown in table 5.2. The left-hand column shows the measured jet energies taken from a sample of pseudo-experiments generated with  $M_t^{MC} = 160 \text{ GeV}/c^2$ . The middle column shows the corresponding upward uncertainties on each of the jet energies and the right-hand column shows the downward uncertainties. Clearly the upward uncertainties are slightly larger than the downward uncertainties, which will lead to a similar discrepancy between the upward and downward mass shifts.

The second reason for the asymmetry of the mass shifts is that the geometrical construction used by the Dalitz-Goldstein Method (see section 5.2.2) establishes a lower bound for the top quark mass that can be reconstructed by the technique. If jet energies are shifted too low there will no fit. Conversely, the method does not place an upper bound on the top quark mass, so that jet energies can be increased without danger of causing a kinematically disallowed fit.

### 5.8.2 Final and Initial State Radiation

As mentioned in section 1.2.1, high  $E_T$  gluons emitted both prior to the production of the  $t\bar{t}$  pair (initial state radiation) and as decay products of the  $t\bar{t}$  pair (final state radiation) effect the jet multiplicity and the distribution of energy among jets in a

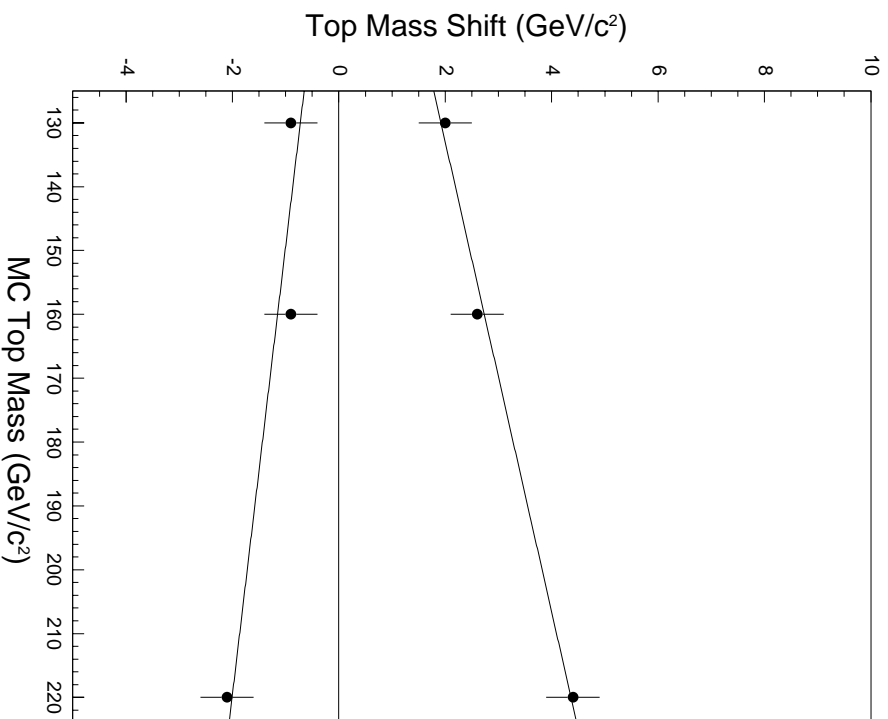


Figure 5.29: Mass shift due to jet energy uncertainty as a function of top mass.

given  $t\bar{t}$  event. To estimate the systematic error due to uncertainty about the correct modeling of initial and final state radiation in  $t\bar{t}$  events, we followed a procedure similar to the one described in reference [90].

For the initial state radiation studies we used PYTHIA V5.7 instead HERWIG V5.6 because initial state radiation cannot be turned off in the latter generator. We used pseudo-experiments with  $M_t^{MC} = 160 \text{ GeV}/c^2$  and measured the reconstructed mass shift,  $M_{shift}^{ISR}$ , when the initial state radiation is turned off (and final state radiation is left on). We also needed to estimate the mass shift when the initial state radiation is increased rather than decreased from its default value. Since the initial state radiation in PYTHIA V5.7 cannot be increased, we assumed that the mass shift resulting from a 100% increase in the default amount of initial state radiation would be equal in magnitude but opposite in direction to the mass shift observed when this



Jet Energy (GeV/c <sup>2</sup> )	Upper Error (GeV/c <sup>2</sup> )	Lower Error (GeV/c <sup>2</sup> )
103.794	7.247	7.432
73.657	2.922	3.072
73.657	2.922	3.072
68.263	2.601	2.720
49.692	3.824	3.893
36.241	1.892	1.943
49.692	3.824	3.893
36.241	1.892	1.943
36.241	1.892	1.943
83.670	4.114	4.285
41.057	2.329	2.389
41.057	2.329	2.389

Table 5.2: Jet energy scale uncertainties for  $M_t = 160$  GeV/c<sup>2</sup>.

radiation is turned off. We made the further assumption (as is done in reference [90]) that no amount of initial state radiation, from zero to twice the default value, is any more likely than any other amount in that range. With these assumptions we were able to calculate the systematic error as the R.M.S. of a flat distribution over a mass shift range of width  $2M_{shift}^{ISR}$ , which is just  $2M_{shift}^{ISR}/\sqrt{12}$ . We quote our systematic error due to uncertainty about the amount of initial state radiation in  $t\bar{t}$  events to be  $0.8 \pm 0.4$  GeV/c<sup>2</sup>.

We performed a similar study to determine the final state radiation contribution to our total systematic error. We used PYTHIA V5\_7 with initial state radiation left on this time. We measured the reconstructed mass shift,  $M_{shift}^{FSR}$ , when final state radiation is turned off and assumed the same mass shift in the opposite direction when the amount of final state radiation is doubled from its default value. Assuming a flat distribution over the range  $2M_{shift}^{FSR}$ , the systemic error was calculated to be  $2M_{shift}^{FSR}/\sqrt{12}$ . We quote our systematic error due to uncertainty about the amount of final state radiation in  $t\bar{t}$  events to be  $0.8 \pm 0.4$  GeV/c<sup>2</sup>, which happens to be equal to our systematic error due to uncertainty in the amount of initial state radiation.

### 5.8.3 Monte Carlo Generators

As mentioned in section 5.6, we used a mapping function derived from HERWIG V5.6 Monte Carlo events to obtain the reconstructed top quark mass that we quote as our final result. To estimate the systematic error for this choice of Monte Carlo generator, we repeated the analysis using a mapping function derived from PYTHIA V5.7 Monte Carlo events and measured the resulting reconstructed mass shifts for various generated top quark masses. We quote the systematic error on our choice of Monte Carlo generator for the input top quark mass range,  $140 < M_t^{MC} < 220$  GeV/c<sup>2</sup>, to be 1.5 GeV/c<sup>2</sup>.

### 5.8.4 Parameterization of Mapping Function

As mentioned in section 5.5.4, the  $\chi^2$  of the linear fit used to construct our mapping function from HERWIG Monte Carlo events that use a jet clustering cone size of 0.4 and that pass the  $H_T$  cut is 2.4. We constructed another mapping function by fitting the scatter plot of  $M_t^{rec.}$  vs.  $M_t^{MC}$  to a second order polynomial function. The  $\chi^2$  of this fit was slightly smaller. However, the final top quark mass reconstructed with this mapping function differed by only 0.2 GeV/c<sup>2</sup> from the mass reconstructed using the linearly parameterized mapping function.

We made a graphical determination of the systematic error for choosing a linearly parameterized mapping function by utilizing a plot of this function with its  $1\sigma$  corridor of errors. See figure 5.13. First we superimposed the background corrected top quark mass found from data onto the mapping function as a horizontal line with  $M_t^{rec.} = 155.1$  GeV/c<sup>2</sup> (recall section 5.6). Then we measured the horizontal distance along this line between the mapping function line and one of its corridor of error lines. This distance was interpreted as the systematic error. We quote our systematic error due to the choice of a linear parameterization for the mapping function to be 2.1 GeV/c<sup>2</sup>.

### 5.8.5 Structure Functions for Event Generation

The MRSD0 structure function parameterizations<sup>[91],[92],[93]</sup> were used when generating the Monte Carlo  $t\bar{t}$  events used for this analysis. We repeated the analysis using PYTHIA V5.7 Monte Carlo  $t\bar{t}$  events that were generated using CTEQ2<sup>[94],[95]</sup> struc-

ture function parameterizations. The resulting change in reconstructed top quark mass was taken as the systematic error. We quote the systematic error due to our choice of structure function parameterizations used for Monte Carlo event generation to be  $1.5 \text{ GeV}/c^2$ .

### 5.8.6 Structure Functions for Fitter

As mentioned in section 5.2.3, the complete likelihood,  $L_i$ , defined by our fitter contains a relative likelihood factor,  $P(x_1, x_2)$ , that quantifies how well the Bjorken- $x$  values calculated for a given kinematical configuration of an event agree with predictions made by the structure functions for the event. Our analysis uses the MRSD0 structure function parameterizations to construct  $P(x_1, x_2)$ . To estimate the systematic error for this choice of structure functions we repeated the analysis using the oldest available version of the Duke-Owens<sup>[96],[97]</sup> structure function parameterizations to calculate  $P(x_1, x_2)$  and then measured the resulting mass shift.

Figure 5.30 shows some combination likelihood distributions calculated from events of varying generated top quark masses. The MRSD0 structure functions were used to construct  $P(x_1, x_2)$  for the distributions shown in the left-hand column. The right-hand column shows the distributions for the same jet-lepton combinations when the Duke-Owens structure functions were used to construct  $P(x_1, x_2)$ . For a given jet-lepton combination, the two distributions differ slightly in shape and integrated value. However, the mean and peak mass values are in very close agreement. This is because the parton distribution functions differ only slightly in the range of Bjorken- $x$  values that are of relevance to  $t\bar{t}$  production. Consequently, the joint likelihood distributions formed from 7 signal events are virtually the same whether MRSD0 or Duke-Owens structure functions are used to calculate  $P(x_1, x_2)$ . We quote the systematic error due to our choice of structure function parameterization for likelihood construction to be  $0.1 \text{ GeV}/c^2$ .

### 5.8.7 Background Sources

Our method for estimating the effect of  $1.3 \pm 0.3$  background events on the top quark mass reconstructed from the 8 data events that pass the  $H_T$  cut was described in section 5.5.5. Although the shifts were calculated using  $W^+W^-$  events, the observed mass shifts due to other background sources like  $Z^0 + jets$  are comparable to or

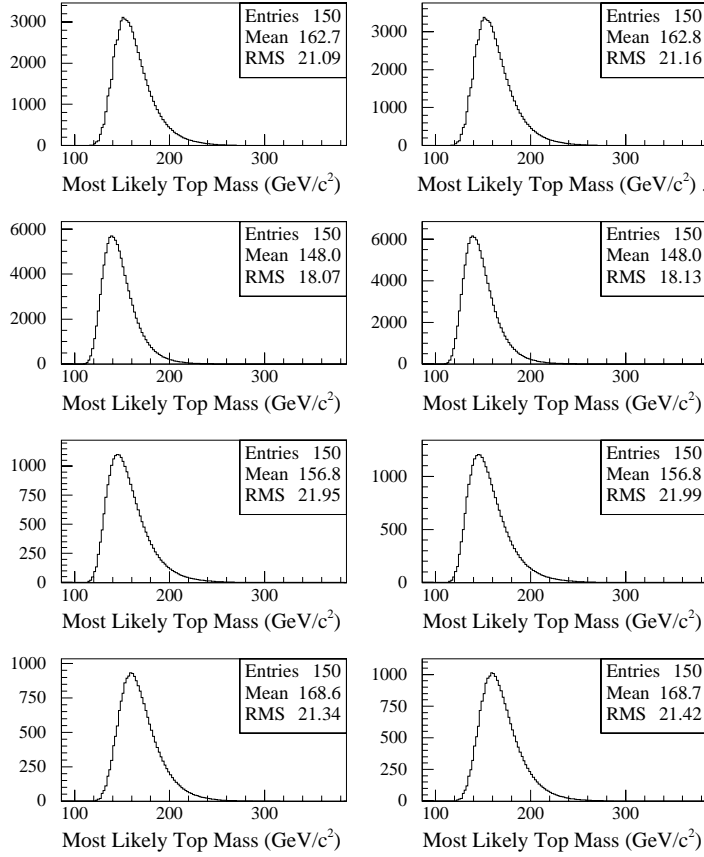


Figure 5.30: Best combination likelihood distributions for pseudo-experiments using two different types of structure functions in the mass fitter. MRSD0 structure functions were used for the distributions in the left-hand column. The right-hand column shows the same pseudo-experiments when Duke-Owens structure functions were used in the fitter.

smaller than the shifts obtained from  $W^+W^-$  events. In section 5.6 it was shown that the expected shift of the reconstructed mass due to background when the  $H_T$  is applied is quite small and is approximately equal to  $1.7 \text{ GeV}/c^2$ . A description of our systematic error for this mass shift is presented here.

Before calculating this systematic error we needed to consider the possibility for the background to fluctuate to more than just one or two events. We used a Poisson distribution of mean 1.4 (the expected number of background events when the  $H_T$  cut is applied) to determine the probability of fluctuations to 1, 2, 3, 4 or 5 background events. The reconstructed mass shifts for 3, 4 and 5 background events were deter-

mined in the same manner as described for 1 and 2 background event fluctuations in section 5.5.5. The probabilities were then multiplied with their respective mass shifts to get the expected contributions to the total mass shift from each of the 5 background fluctuations. The total expected mass shift due to background fluctuations was calculated as the sum of these weighted mass shifts. Table 5.3 shows the expected mass shifts due to background fluctuations. The left-hand column shows the number of background fluctuations, the next column to the right shows the probabilities for these fluctuations, the next column shows the mass shifts resulting from the fluctuations and the right-hand column shows the contributions of each fluctuation to the total expected mass shift. We did not measure the mass shifts for fluctuations greater than 5 events because the probabilities of such fluctuations are negligible. For example, the probability of 6 background events is 0.002579. The total expected mass shift due to background fluctuations is  $1.999 \text{ GeV}/c^2$ .

N	P(N)	Shift ( $\text{GeV}/c^2$ )	Shift*P(N) ( $\text{GeV}/c^2$ )
0	0.2466	0.00	0.000
1	0.3452	1.65	0.569
2	0.2416	2.97	0.717
3	0.1128	4.02	0.453
4	0.0395	4.81	0.190
5	0.0111	6.35	0.070
Total Shift			1.999
Total Error			0.999

Table 5.3: Mass shift due to background fluctuations.

To be conservative, we take the systematic error to be 50% of the total mass shift expected for  $W^+W^-$  background events. Therefore, we quote our systematic error on the reconstructed mass shift expected from background events to be  $1.0 \text{ GeV}/c^2$ . If no  $H_T$  cut is applied this error is larger (approximately  $1.5 \text{ GeV}/c^2$ ) since the expected mass shift due to background is also larger.

### 5.8.8 Parameterization of Background Induced Mass Shift

There is also a small systematic uncertainty due to our choice of a linear fit to parameterize the background induced mass shift plot as a function of generated top quark

mass (see section 5.5.5). To determine this uncertainty we used a graphical method analogous to the one described in section 5.8.4 to estimate the systematic error for using a linear fit in the parameterization of the mapping function. We superimposed, as a horizontal line, the reconstructed mass found from data onto the parameterization of the mean mass shift shown in the left-hand plot of figure 5.16. The systematic error was interpreted as the distance along this horizontal line from the mass shift line to one of its corridor of error lines (the error lines are not shown in figure 5.16). We quote the systematic error for using a linear parameterization of the background induced mass shift to be  $0.4 \text{ GeV}/c^2$ .

### 5.8.9 Top Quark Polarization

In PYTHIA V5\_6 Monte Carlo events the top quarks are generated with an isotropic distribution, while in HERWIG V5\_6 and PYTHIA V5\_7 Monte Carlo events these quarks are polarized. To estimate the systematic uncertainty arising from HERWIG's modeling of the top quark polarization, we repeated our analysis using PYTHIA V5\_6 events instead of HERWIG V5\_6 events and measured the resulting mass shift. We quote the systematic error due to the modeling of top quark polarization to be  $1.0 \text{ GeV}/c^2$ .

### 5.8.10 Total Systematic Error

To find the total systematic error on our mass fitting technique, we assumed that all of the systematic errors quoted in sections 5.8.1 to 5.8.9 are uncorrelated so that they could be added together in quadrature. We quote the total systematic error due to our method to be  $\pm_{3.7}^{4.3} \text{ GeV}/c^2$ . Table 5.4 gives a complete listing of the systematic errors. If no  $H_T$  cut is applied then the systematic error due to background sources increases to  $1.5 \text{ GeV}/c^2$  and the total systematic error becomes  $_{-3.9}^{+4.5} \text{ GeV}/c^2$ .

Systematic Error	Mass Shift (GeV/c <sup>2</sup> )
Jet Energy Scale	+2.6 – 1.3
Final State Radiation	0.8 ± 0.4
Initial State Radiation	0.8 ± 0.4
Monte Carlo Generators	1.5
Mapping Function Parameterization	2.1
Structure Functions (generator)	1.5
Structure Functions (likelihood)	0.1
Background Sources	1.0
Background Mass Shift Parameterization	0.4
Top Quark Polarization	1.0
Total	+4.3 – 3.7

Table 5.4: List of Systematic Errors ( $M_t = 160$  GeV/c<sup>2</sup> and  $H_T$  cut applied).

# Chapter 6

## Conclusions

The final results are summarized, some cross checks of the method are presented and a comparison is made between this top quark mass fitting technique and other fitters whose results have also been accepted by the CDF Collaboration.

### 6.1 Final Results

We have applied the Dalitz-Goldstein mass fitting technique to the Run 1 dilepton event data sample and we have determined the top quark to have a mass of:

$$M_{top} = 157.1 \pm 10.9(stat.) \pm_{3.7}^{4.3}(syst.) GeV/c^2 \quad (6.1)$$

This result was obtained using a mapping function constructed from HERWIG Monte Carlo events that pass the  $H_T$  cut and that use a jet clustering cone size of 0.4. As mentioned in section 5.5.4, the top quark mass was also reconstructed with seven other mapping functions that were each derived from a different combination of Monte Carlo generator (HERWIG or PYTHIA), jet clustering cone size (0.4 or 0.7) and  $H_T$  cut (applied or not applied). The results for all eight mapping functions are presented in table 6.1. The columns labeled as  $\sigma$  represent total errors (i.e. statistical and systematic errors added in quadrature). None of these results differ by more than 8 GeV/c<sup>2</sup>.

### 6.2 Checking the Method

To verify that our mass fitting technique is self-consistent and that our mass reconstruction routines are free of bugs, we performed several cross checks, many of which were suggested by the CDF top group.

#### 6.2.1 Blind Test

The CDF top group conducted a "blind test" to verify that each of the proposed top quark mass fitting methods is self-consistent. The conveners of the group generated HERWIG  $t\bar{t}$  events of a fixed input top quark mass that was known only to them. By



				HERWIG			PYTHIA		
sample	N	$M^{unc}$	$M^{corr}$	$M_t$	stat.	$\sigma$	$M_t$	stat.	$\sigma$
0.4, no HT-cut	9	151.0 $\pm$ 5.2	154.0 $\pm$ 5.2	153.4	12.9	13.6	158.1	12.7	13.4
0.4, HT-cut	8	153.4 $\pm$ 5.7	155.1 $\pm$ 5.7	157.1	12.8	13.5	157.4	13.0	13.7
0.7, no HT-cut	8	153.5 $\pm$ 5.7	156.6 $\pm$ 5.7	157.8	13.1	13.8	159.9	12.9	13.6
0.7, HT-cut	7	156.4 $\pm$ 6.4	158.1 $\pm$ 5.5	157.0	14.4	15.0	160.5	14.2	14.9

Table 6.1: Top quark mass results using different mapping functions.

combining these  $t\bar{t}$  events with  $W^+W^-$  events generated by PYTHIA and ISAJET, a total of 559 eight-event pseudo-experiments were constructed. The number of  $W^+W^-$  events in each pseudo-experiment was binomially distributed with a probability of  $1.3/8.0 = 0.1625$ . All events were required to pass both the standard dilepton event selection cuts and the  $H_T$  cut. Each of the top quark mass fitters was applied to this "blind sample" of pseudo-experiments and each of the resulting reconstructed masses was compared to the input top quark mass.

The input top quark mass was revealed to be 182.0 GeV/c<sup>2</sup>. Figure 6.1 shows a distribution of the top quark masses reconstructed by our method for all of the pseudo-experiments in the blind sample, using a mapping function derived from HERWIG V5\_6  $t\bar{t}$  events with a jet clustering cone size of 0.4 and the  $H_T$  cut applied. The mean of the distribution, being 183.5 GeV/c<sup>2</sup>, is very close to the input top quark mass. Figure 6.2 shows the reconstructed mass distribution when a mapping function derived from PYTHIA V5\_7  $t\bar{t}$  events was used instead. The mean of this distribution is 181.6 GeV/c<sup>2</sup>, which is also close to the input top quark mass. The latter result shows the method's lack of sensitivity to Monte Carlo biases since the blind sample was generated with HERWIG  $t\bar{t}$  events.

Because our top quark mass fitting technique depends on Monte Carlo events (via the mapping function, expected mass shifts due to background, etc.) the results of the blind test serve primarily to confirm that our fitter is self-consistent and free of programming bugs.

### 6.2.2 Application to Lepton+Jets Events

The Run 1 lepton+jets data sample consists of 83 events, 34 of which contain at least one jet tagged by the SECVTX or the SLT  $b$ -tagging algorithms (see section 4.3).

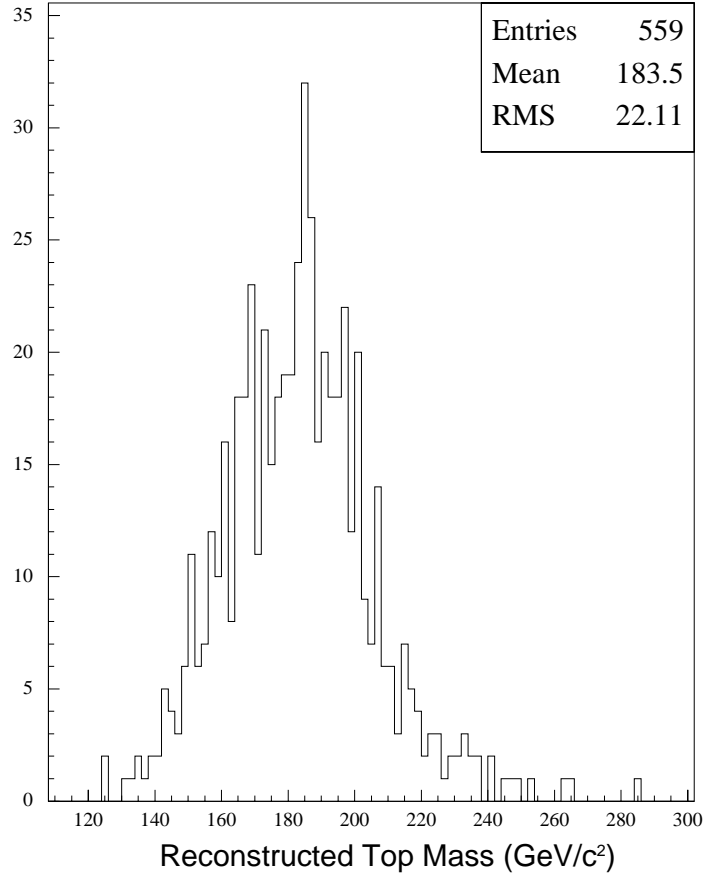


Figure 6.1: Distribution of top quark masses reconstructed from the CDF blind sample using a mapping function derived from HERWIG Monte Carlo events.

Of the 34  $b$ -tagged events, 5 have two jets tagged by the SECVTX algorithm (see references [21] and [90] for more details about the Run 1 lepton+jets data sample). As a further cross check of our mass fitting technique, we applied the Dalitz-Goldstein method for dilepton events to these 5 double-tagged lepton+jets events and compared the results to those obtained by using the standard CDF mass fitter for lepton+jets events called MINUIT<sup>[98],[99]</sup>.

To simulate dilepton events, one of the two untagged jets in each double-tagged event was treated as the second charged lepton while the remaining untagged jet was treated as a neutrino and ignored. Thus, there were two possible jet assignments for the second charged lepton. We tried two different methods for removing this ambiguity: (i) The second charged lepton was assigned to the untagged jet for which

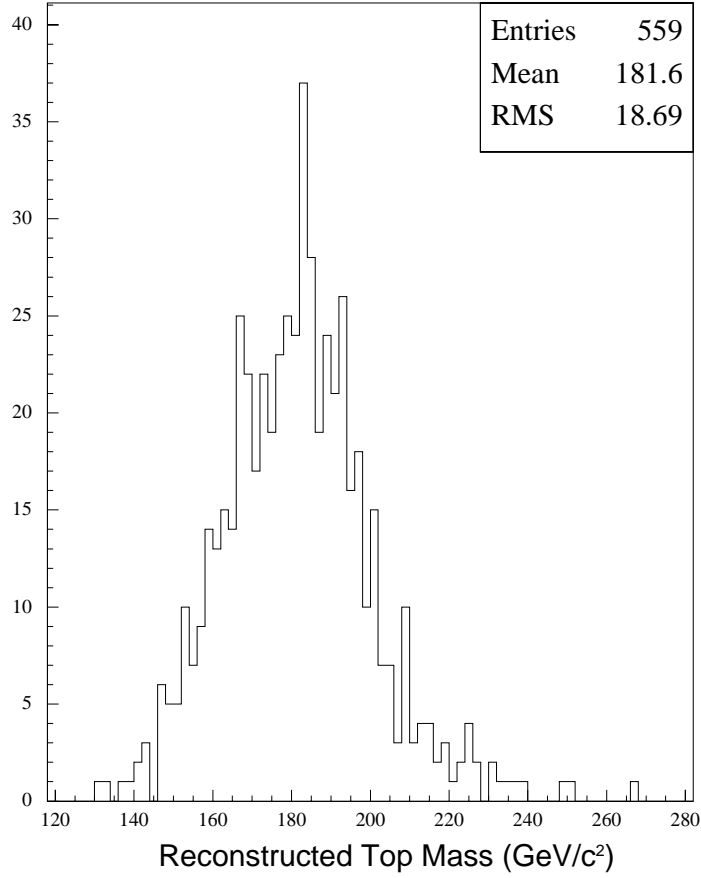


Figure 6.2: Distribution of top quark masses reconstructed from the CDF blind sample using a mapping function derived from PYTHIA Monte Carlo events.

the combination likelihood,  $L_{comb.}$ , is largest or (ii) the second charged lepton was assigned to the untagged jet with the highest  $E_T$ .

Table 6.2 shows reconstructed top quark masses obtained from the double-tagged event sample in three different ways. The left-hand column lists the run and event number of each event. The next column to the right shows the top quark mass reconstructed for each event when using the MINUIT fitter. The next column presents the mass results for the Dalitz-Goldstein method when the second charged lepton is assigned to the untagged jet for which  $L_{comb.}$  is largest and the right-hand column gives the results for the same fitter when the second charged lepton is assigned to the untagged jet with the highest  $E_T$ . The two methods of jet assignment for the second

Run_Event	MINUIT (GeV/c <sup>2</sup> )	Best $L_{comb.}$ (GeV/c <sup>2</sup> )	Highest E <sub>T</sub> jet (GeV/c <sup>2</sup> )
40748_44414	175.4±12	178	182
65581_322592	152.6± 9	150	154
67824_281883	170.2±11	174	174
67971_55023	183.1±12	184	184
68464_547303	150.0±08	158	158

Table 6.2: Results of the fits to the double-tagged lepton+jets events.

charged lepton give very similar results, with a maximum discrepancy of 4 GeV/c<sup>2</sup>. These results differ from the MINUIT results by no more than 8 GeV/c<sup>2</sup>.

Using the joint likelihood method, we multiplied the best combination likelihood distributions of each event together and measured the mean value of the resulting joint likelihood distribution. Assigning the second charged lepton to the untagged jet for which  $L_{comb.}$  is a maximum, we obtained a joint likelihood distribution of mean:

$$M_{top}^{uncorr.} = 173.4 \pm 8.6 \text{ GeV}/c^2 \quad (6.2)$$

Assuming zero background events and applying the mapping function derived from HERWIG  $t\bar{t}$  events that pass the  $H_T$  cut and that use a jet clustering cone size of 0.4, we obtained a top quark mass of:

$$M_{top}^{(i)} = 187 \pm 17 \text{ GeV}/c^2 \quad (6.3)$$

Repeating these steps using the second way of assigning the second charged lepton to an untagged jet, we obtained a final top quark mass result of:

$$M_{top}^{(ii)} = 188 \pm 17 \text{ GeV}/c^2 \quad (6.4)$$

Hence, the results obtained using the two different jet assignments for the second charged lepton differ by only 1 GeV/c<sup>2</sup>. It is important to note that in addition to neglecting background events, these results were obtained by applying a mapping function derived from 7-event pseudo-experiments to a data sample containing only 5 events.

### 6.2.3 Other Cross Checks

We conducted our own version of the blind test for several HERWIG generated top quark masses,  $M_t^{MC}$ , by applying the fitter to 8-event pseudo-experiments. The results for an input top quark mass of 160 GeV/c<sup>2</sup> were already presented in figure 5.24. The results for input top quark masses of 150 and 170 GeV/c<sup>2</sup> are shown in figures 6.3 and 6.4, respectively. In each figure, the upper plot shows a distribution of the fully reconstructed masses,  $M_t^{fitter}$ , for each pseudo-experiment; The middle plot shows a distribution of pulls defined as  $(M_t^{fitter} - M_t^{MC})/\sigma_{stat.}^{corrected}$ , where  $\sigma_{stat.}^{corrected}$  is the statistical error after being corrected by the mapping function (see section 5.7); The lower plot shows a distribution of the  $\sigma_{stat.}^{corrected}$  values for each pseudo-experiment. For all three input top quark masses, the mean value of the  $\sigma_{stat.}^{corrected}$  distribution is smaller than the R.M.S. of the  $M_t^{fitter}$  distribution and the pull distribution has an R.M.S. that is somewhat greater than one. This indicates that  $\sigma_{stat.}^{corrected}$  slightly underestimates the statistical error. It was shown in section 5.7 that this discrepancy results from the smallness of the data sample. Recall that we derived our final statistical error by multiplying the  $\sigma_{stat.}^{corrected}$  found from data by the R.M.S. of the pull distribution found for  $M_t^{MC} = 160$  GeV/c<sup>2</sup>, namely 1.13.

As a final check of our interpretation for the statistical error, we sliced the distribution of  $\sigma_{stat.}^{corrected}$  values for  $M_t^{MC} = 160$  GeV/c<sup>2</sup> (see the lower plot of figure 5.24) into 4 bins. For each collection of events in the 4 bins we calculated a distribution of fully reconstructed masses like the one shown in the upper plot of figure 5.24. The R.M.S. values of these distributions were plotted as a function of the corresponding average value of  $\sigma_{stat.}^{corrected}$  for each bin. This four point scatter plot is shown in figure 6.5. It is clear that the R.M.S values of the fully reconstructed mass distributions increase linearly with increasing  $\sigma_{stat.}^{corrected}$ , as required.

## 6.3 Comparison to Other Methods

A brief description is given of other top quark mass fitting techniques that have recently been accepted by the CDF Collaboration. The distinguishing features of the Dalitz-Goldstein method are then listed for purposes of comparison.

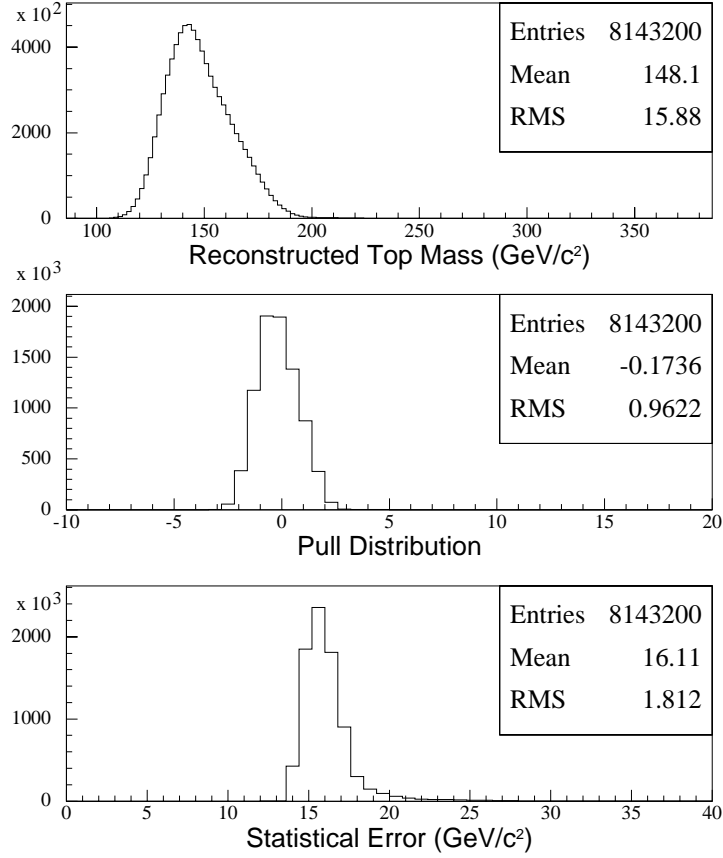


Figure 6.3: Application of the complete mass fitting technique, including mapping function corrections, to a set of 8-event pseudo-experiments generated by HERWIG Monte Carlo using a top quark mass of  $150 \text{ GeV}/c^2$ .

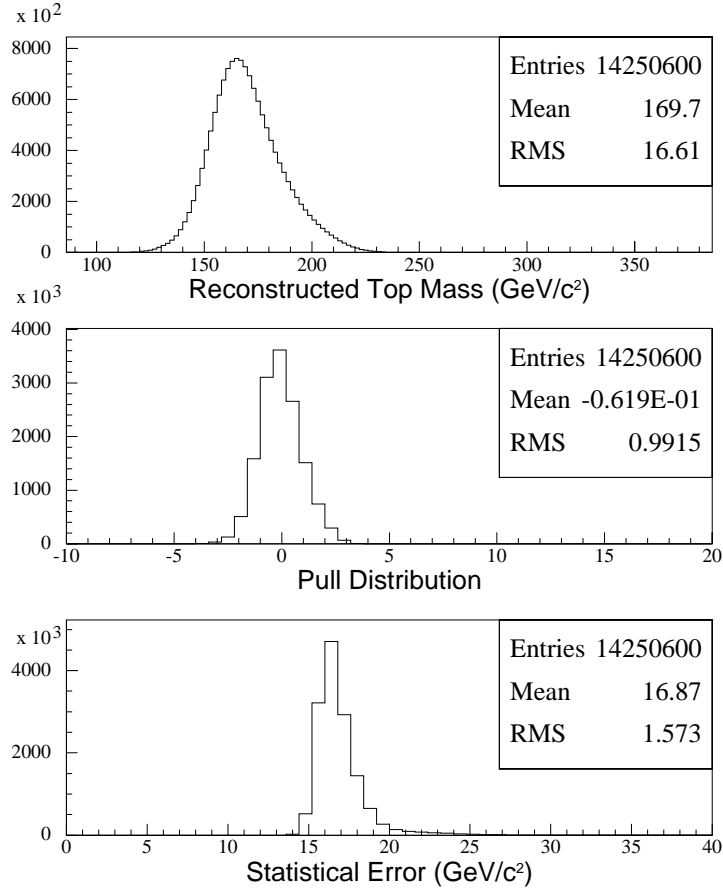


Figure 6.4: Application of the complete mass fitting technique, including mapping function corrections, to a set of 8-event pseudo-experiments generated by HERWIG Monte Carlo using a top quark mass of  $170 \text{ GeV}/c^2$ .

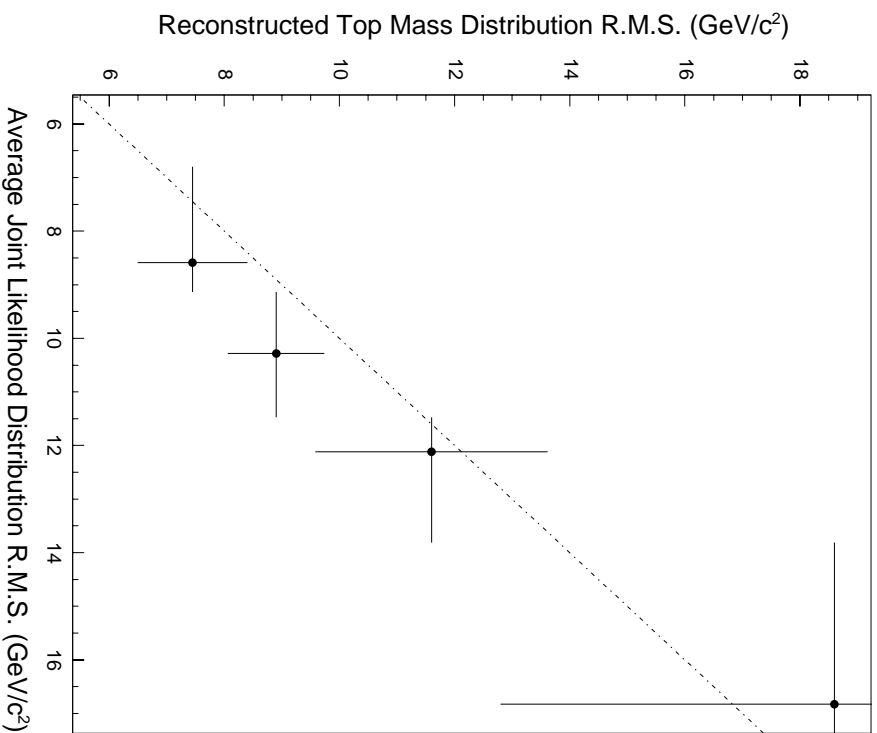


Figure 6.5: Reconstructed top quark mass distribution R.M.S. vs. average joint likelihood distribution R.M.S. for 8-event pseudo-experiments generated by Herwig Monte Carlo using a top quark mass of  $160 \text{ GeV}/c^2$ .

### 6.3.1 Kinematical Distributions

This technique estimates the most likely top quark mass by comparing certain kinematical distributions taken from the data to these same distributions when obtained from Monte Carlo  $t\bar{t}$  and background events.

The kinematical variable chosen to obtain the final result was the jet energy distribution of the two highest  $E_T$  jets in a given event. Distributions (or “templates”) of this kinematical variable were constructed both from Monte Carlo  $t\bar{t}$  events generated over a wide top quark mass range and from expected background events. A likelihood,  $\mathcal{L}_m$ , for each top quark mass,  $m$ , was constructed by comparing the value,  $x_i$ , of the kinematical variable from each data event to both its probability,  $T(x_i)$ ,



in the  $t\bar{t}$  template of mass  $m$  and its probability,  $B(x_i)$ , in the background template.  $\mathcal{L}_m$  has the form:

$$\mathcal{L}_m = P(N_B, n_B) \cdot \prod_i \frac{n_B \cdot B(x_i) + n_t \cdot T(x_i)}{n_B + n_t} \quad (6.5)$$

where the product is over the data events that pass the standard cuts including the  $H_T$  cut,  $N_B$  is the expected number of background events,  $n_B$  is the nearest integer number of background events,  $P(N_B, n_B)$  is the Poisson probability of having  $n_B$  background events when the expected number is  $N_B$  and  $n_t \equiv n_{data} - n_B$  is the nearest integer number of expected top quark events. The negative logarithm of each likelihood was plotted as a function of top quark mass and the resulting points were fit to a third order polynomial. The most likely top quark mass value was determined by finding the value of  $m$  that corresponds to the lowest value of  $-\ln \mathcal{L}_m$  on this curve.

The final result quoted for this fitter is:

$$M_{top} = 159 \pm 23(stat.) \pm 11(syst.) \text{ GeV}/c^2 \quad (6.6)$$

The statistical errors were determined by increasing  $-\ln \mathcal{L}_m$  from its minimum by 0.5 and measuring the resulting negative and positive mass shifts. A detailed description of this analysis can be found in references [100] and [101].

### 6.3.2 Invariant Mass of Charged Lepton and $b$ Quark

This fitter reconstructs the top quark mass by measuring the combined invariant mass of two of its daughter particles, the charged lepton and the  $b$  quark. The method works in the rest frame of the  $W$  boson. In this frame the top quark mass,  $M_t$ , is given by:

$$M_t = M_W^2 + M_b^2 + 2M_W E_b \quad (6.7)$$

where  $M_W$  and  $M_b$  are the known invariant masses of the  $W$  boson and the  $b$  quark, respectively, and  $E_b$  is the energy of the  $b$  quark in the  $W$  boson rest frame.

Continuing to work in the  $W$  boson rest frame and neglecting the lepton and  $b$  quark masses compared to their respective energies, it can be shown that the Lorentz invariant squared mass of the charged lepton and the  $b$  quark is:

$$M_{lb}^2 \cong M_W E_b (1 - \cos \theta_{lb}) \quad (6.8)$$

where  $\theta_{lb}$  is the angle between the charged lepton and the  $b$  quark in this frame. Solving equation 6.8 for  $E_b$  and using this result in equation 6.7, the top quark mass can be expressed as:

$$M_t^2 = M_W^2 + \frac{2M_{lb}}{1 - \cos \theta_{lb}} \quad (6.9)$$

Taking an average of equation 6.9 over all of the dilepton events in the Run 1 data sample one finds:

$$M_t^2 = M_W^2 + \frac{2\langle M_{lb} \rangle}{1 - \langle \cos \theta_{lb} \rangle} \quad (6.10)$$

The average squared invariant mass of the charged lepton and the  $b$  quark,  $\langle M_{lb} \rangle$ , can be measured from data. The average angle between the charged lepton and the  $b$  quark in the  $W$  boson rest frame,  $\langle \cos \theta_{lb} \rangle$ , must be determined by theory or from Monte Carlo studies.

The statistical error on  $M_t$  is determined by straightforward error analysis and has the form:

$$\sigma_{M_t} = \frac{1}{M_t} \frac{\sigma \langle M_{lb}^2 \rangle}{1 - \langle \cos \theta_{lb} \rangle} \quad (6.11)$$

where  $\sigma \langle M_{lb}^2 \rangle$  is the statistical uncertainty on  $\langle M_{lb}^2 \rangle$ . The uncertainty on  $\langle \cos \theta_{lb} \rangle$  is regarded as systematic and is not used in the derivation of equation 6.11.

The top quark mass reconstructed by this fitter is:

$$M_{top} = 163 \pm 20.2(stat.) \pm 5.9(syst.) GeV/c^2 \quad (6.12)$$

Note that the systematic error has improved since this result was published in reference [22]. This fitting technique is described in detail in references [102] and [103].

### 6.3.3 Neutrino Weighting Method

This method is similar to a mass fitter called the "Neutrino Weighting Technique" that was developed by the D0 collaboration (see references [104] and [105]). Essentially, the method constrains the dilepton events by using Monte Carlo predicted

neutrino pseudorapidity values and finds the most likely mass for each event by using a weighting function that downgrades solutions for which the predicted neutrino-system transverse energy is far from the measured missing transverse energy.

To solve for the unknowns of the fit (i.e. the three-momenta of the two neutrinos), the method starts with a set of constraint equations that are very similar to those used by the Dalitz-Goldstein method (see section 5.2.1). However, instead of using constraints that take advantage of the predicted  $E_T$  of the  $t\bar{t}$  system (see equations 5.7 and 5.8), the neutrino weighting method uses the expected pseudorapidity values of the two neutrinos,  $(\eta_1, \eta_2)$ , to fully constrain the fit.

The components of the predicted transverse energy of the two-neutrino system,  $(\vec{\cancel{E}}_{Tx}^p, \vec{\cancel{E}}_{Ty}^p)$ , are calculated from the complete set of constraints. For a given event and a given assumed top quark mass,  $M_t$ , there are 8 possible solutions for the two-neutrino transverse energy. This is because there are 2 possible longitudinal components for each of the 2 neutrino three-momenta and there are 2 possible ways of assigning the two highest  $E_T$  jets to the two charged leptons of a candidate dilepton event. (This method only uses the two highest  $E_T$  jets but merges low energy jets and muons back into these jets when appropriate). Each predicted transverse energy solution is compared to the measured missing transverse energy,  $(\vec{\cancel{E}}_{Tx}^m, \vec{\cancel{E}}_{Ty}^m)$ , by assigning the solution a relative weight of the form:

$$P(\eta_1, \eta_2, M_t) = e^{-(\vec{\cancel{E}}_{Tx}^p - \vec{\cancel{E}}_{Tx}^m)^2 / 2\sigma^2} \cdot e^{-(\vec{\cancel{E}}_{Ty}^p - \vec{\cancel{E}}_{Ty}^m)^2 / 2\sigma^2} \quad (6.13)$$

where  $\sigma$  is the uncertainty on the "unclustered" transverse energy, that is, on the total residual transverse energy lying outside the cones used by the jet clustering algorithm to form jets. Based on minimum bias data events and Monte Carlo studies  $\sigma$  has been assigned a value of 4.0 GeV. Now, in terms of the unclustered transverse energy the components of the missing transverse energy may be defined as:

$$\vec{\cancel{E}}_{Ti}^m = E_T(n.c.)_i + E_T(leptons)_i + E_T(jets)_i \quad (6.14)$$

where  $i = x$  or  $y$ ,  $E_T(n.c.)_i$  is the  $i$  component of the unclustered transverse energy,  $E_T(leptons)_i$  is the sum of the  $i$  components of the lepton transverse energies and  $E_T(jets)_i$  is the sum of the  $i$  components of the corrected jet transverse energies. The

justification for equating  $\sigma$  only with the resolution of the unclustered  $E_T$  contribution to the total missing transverse energy will be explained shortly.

For a given  $M_t$ , the weight,  $P(\eta_1, \eta_2, M_t)$ , is scanned over all possible values of neutrino pseudorapidity by dividing HERWIG Monte Carlo generated distributions of both  $\eta_1$  and  $\eta_2$  into ten equal area bins and computing the weight for the resulting  $10 \times 10$  possible  $(\eta_1, \eta_2)$  bin combinations. Each of these weights is then added together to obtain a new weight for the given mass:

$$P(M_t) = \sum_{\eta_1, \eta_2} P(\eta_1, \eta_2, M_t) \quad (6.15)$$

The effects of jet and lepton energy mismeasurement are accounted for by varying the jet and lepton energies many times within the limits of their expected resolution and calculating  $P(\eta_1, \eta_2, M_t)$  for each variation. By repeating these scanning procedures for all 8 possible solutions,  $(\vec{\cancel{E}}_{Tx}^p, \vec{\cancel{E}}_{Ty}^p)$ , and by adding all resulting values of  $P(\eta_1, \eta_2, M_t)$  together, an overall event weight for a top quark mass of  $M_t$  is obtained:

$$P_{ev}(M_t) = \sum_{\eta_1, \eta_2, \Delta E, \vec{\cancel{E}}_T^p} P(\eta_1, \eta_2, M_t) \quad (6.16)$$

In the above equation,  $\Delta E$  represents the summation over jet and lepton energy resolutions and  $\vec{\cancel{E}}_T^p$  represents the summation over the 8 solutions of  $(\vec{\cancel{E}}_{Tx}^p, \vec{\cancel{E}}_{Ty}^p)$ . It is because this scanning process involves the sampling of  $\vec{\cancel{E}}_T^m$  over the full range of jet and lepton energy resolutions that only the resolution of the unclustered  $E_T$  is assigned to  $\sigma$  in equation 6.13.

$P_{ev}(M_t)$  is evaluated in 2.5 GeV/c<sup>2</sup> steps over a wide range of possible top quark mass values ( $90 < M_t < 290$  GeV/c<sup>2</sup>). The resulting  $P_{ev}(M_t)$  values are added to a histogram to create an event probability distribution as a function of  $M_t$ . The top quark mass estimate,  $M_{ev}$ , for a given event will generally lie near the value of  $M_t$  for which  $P_{ev}(M_t)$  is a maximum (see reference [89] for complete details about the extraction of  $M_{ev}$ ).

To obtain the final top quark mass, the individual masses,  $M_{ev}$ , found from each data event were fit to templates of Monte Carlo  $t\bar{t}$  events and background events by using a likelihood function,  $\mathcal{L}_m$ , almost identical to the one used by the "kinematical distributions" mass fitting technique (see equation 6.5). The distribution of  $-\ln \mathcal{L}_m$

values were plotted as a function of mass and fit to a curve. The final result was interpreted as the mass corresponding to the minimum point,  $(-\ln\mathcal{L}_m)_{min}$ , in the fitted curve.

A first estimate of the statistical error was obtained by measuring the positive and negative mass shifts that result from moving to the two points on the curve where  $-\ln\mathcal{L}_m = 0.5(-\ln\mathcal{L}_m)_{min}$ . Pull distributions obtained from Monte Carlo events indicated that this estimate was lower than the true statistical error by approximately 10%. In a study similar to the one mentioned in section 5.7 it was confirmed that this underestimation problem would be improved with a larger data sample. Therefore, it was deemed appropriate to obtain the final statistical error by multiplying the initial estimate by a factor of 1.1.

Using CDF Run 1 dilepton events, the neutrino weighting method measures a top quark mass of:

$$M_{top} = 167.4 \pm 10.3(stat.) \pm 4.8(syst.) GeV/c^2 \quad (6.17)$$

This analysis is fully documented in reference [89]. Because of its much improved statistical and systematic errors, the top quark mass reconstructed by the neutrino weighting method recently superseded the combined reconstructed mass of the kinematical distribution fitter and the  $\langle M_{tb}^2 \rangle$  fitter as the official top quark mass measured by the CDF collaboration in the dilepton channel.

#### 6.3.4 Modified MINUIT Fitter

This mass fitting technique was developed for dilepton events by appropriately modifying the MINUIT mass fitter, which was originally designed for application to lepton+jets  $t\bar{t}$  events (see references [98], [99] and [90]).

To constrain the dilepton events, the modified MINUIT fitter uses a set of constraint equations that are almost identical to those used by the neutrino weighting method. However, instead of sampling the full range of possible neutrino pseudorapidity values, with probabilities determined by Monte Carlo events, this method samples the full range of possible neutrino azimuthal angles  $(\phi_{\nu_1}, \phi_{\nu_2})$ . Since  $\phi_{\nu_1}$  and  $\phi_{\nu_2}$  are expected to be distributed uniformly between 0 and  $2\pi$ , Monte Carlo information is not needed at this level of the procedure.

For a given event and a given choice of angles  $(\phi_{\nu_1}, \phi_{\nu_2})$ , the three-momenta of the neutrinos are calculated by using the measured components of the missing transverse energy. There are 8 possible solutions for a given choice of  $(\phi_{\nu_1}, \phi_{\nu_2})$  since each neutrino three-momentum has 2 possible longitudinal components and there are 2 possible ways to pair the two highest  $E_T$  jets with the two lepton candidates. A top quark mass,  $M_t$ , is reconstructed for each of the 8 solutions by minimizing the following  $\chi^2$  quantity:

$$\begin{aligned} \chi^2 = & \sum_{l,j} \frac{(P_T - \tilde{P}_T)^2}{\sigma^2(P_T)} + \sum_{i=x,y} \frac{(E_i^u - \tilde{E}_i^u)^2}{\sigma^2(E_i^u)} + \\ & \frac{(M_W - M_{l_1, \nu_1})^2}{\sigma^2(M_W)} + \frac{(M_W - M_{l_2, \nu_2})^2}{\sigma^2(M_W)} + \frac{(M_t - \tilde{M}_t)^2}{\sigma^2(M_t)} + \frac{(M_{\bar{t}} - \tilde{M}_{\bar{t}})^2}{\sigma^2(M_t)} \end{aligned} \quad (6.18)$$

The first sum in equation 6.18 is over the two lepton candidates and all jets in the central region of the detector ( $|\eta| \leq 2.4$ ) with uncorrected  $E_T > 8$  GeV. In this sum,  $P_T$  represents the transverse momentum measured by the detector (after standard corrections have been applied),  $\tilde{P}_T$  represents the transverse momentum output by the minimization procedure and  $\sigma(P_T)$  represents the resolution of  $P_T$  measurement. The second sum is over the transverse components of the energy excluded by the jet clustering algorithm (using a cone size of 0.4), where  $E_i^u$  is the measured energy,  $\tilde{E}_i^u$  is the energy output by the minimization procedure and  $\sigma(E_i^u)$  is the resolution of  $E_i^u$  measurement. In the remaining four terms of the equation,  $M_W$  is the known mass of the  $W$  boson;  $\sigma(M_W)$  and  $\sigma(M_t)$  are the known natural widths of the  $W$  boson and the top quark, respectively;  $M_{l_1, \nu_1}$  and  $M_{l_2, \nu_2}$  are the invariant masses of the charged leptons and neutrinos for a given neutrino three-momenta solution; and  $\tilde{M}_t$  and  $\tilde{M}_{\bar{t}}$  are the top quark and antitop quark masses for a given neutrino three-momenta solution and a given choice of jet-lepton pairings.

For a given event, this minimization procedure is repeated over the entire range of possible neutrino azimuthal angles by dividing the  $(\phi_{\nu_1}, \phi_{\nu_2})$  plane into a grid of  $12 \times 12$  points. Of the 8 possible solutions for each point in the grid, the one with lowest  $\chi^2$  value is retained so that the fitter yields a total of 144 possible top quark masses,  $M_{i,j}^{top}$ , and associated  $\chi^2$  values,  $\chi^2_{i,j min}$ , where  $i, j = 1..12$ . Each of the 144 solutions is assigned a weight of the form:

$$w_{i,j} = \frac{\exp(-\chi^2_{i,j}/2)}{\sum_{i=1}^{12} \sum_{j=1}^{12} \exp(-\chi^2_{i,j}/2)} \quad (6.19)$$

The weights are plotted as a function of  $M_{i,j}^{top}_{min}$  to obtain a probability density distribution over the range of possible top quark masses for the given event.

Templates were constructed from Monte Carlo  $t\bar{t}$  event samples by adding together the probability density distributions of each event of a given generated top quark mass. Templates were also constructed for the expected background events. The final top quark mass was reconstructed by comparing the probability density distributions from the Run 1 data sample to the template distributions, via a likelihood function very similar in construction to that used by the kinematical distributions fitter and the neutrino weighting method. The top quark mass reconstructed by the modified MINUIT fitter is:

$$M_t = 170.7^{+10.6}_{-10.0}(stat.) \pm 4.6(syst.) \text{ GeV}/c^2 \quad (6.20)$$

See reference [106] for a more complete description of this method, including the error analysis.

### 6.3.5 Distinguishing Features of the Dalitz-Goldstein Method

Being approximately 10 GeV/ $c^2$  smaller than the mass reconstructed by the neutrino weighting method and approximately 13 GeV/ $c^2$  smaller than the mass obtained by the modified MINUIT fitter, the top quark mass reconstructed by the Dalitz-Goldstein method in the dilepton channel is closer to the results obtained by the kinematical distributions fitter and the  $\langle M_{lb}^2 \rangle$  method. However, the statistical and systematic errors obtained by using the Dalitz-Goldstein method are quite consistent with those quoted by both the neutrino weighting method and the modified MINUIT fitter. Moreover, the mass results for all three techniques agree within the limits of their errors.

The main features that distinguish the Dalitz-Goldstein method from the four top quark mass fitters described in this section are the following: (i) It does not require any *a priori* knowledge about an event's missing transverse energy (a quantity that is poorly measured by the CDF detector), (ii) it constrains a given dilepton event by using the most likely transverse momentum of the  $t\bar{t}$  system (as determined by

Monte Carlo studies), (iii) it samples all possible jet-lepton combinations, rather than merging jets or using only the two highest  $E_T$  jets of a given event, (iv) it includes structure function information in the construction of its event likelihood functions and (v) it utilizes information about the shapes of the likelihood distributions obtained for each event. See reference [107] for additional documentation about our analysis of the CDF Run 1 dilepton event sample.



# Appendix A

## CDF Coordinate System

The CDF detector has both azimuthal and forward-backward symmetry with respect to the  $p\bar{p}$  beam line. It is customarily described in terms of a right-handed coordinate system whose origin is at the center of the detector and whose  $z$ -axis is collinear with the beam line. The positive  $z$ -axis is taken to point in the direction of the proton beam and the positive  $x$ -axis points directly away from the center of the Tevatron so that the positive  $y$ -axis points directly up. The radial distance  $r$ , the azimuthal angle  $\phi$  and the polar angle  $\theta$  are defined in the usual way relative to a right-handed coordinate system. The detector covers the full azimuthal angular range and it covers a polar angular range of  $2^\circ \leq \theta \leq 178^\circ$ . Figure 2.2 in section 2.2 illustrates the relation of the  $x$ ,  $y$ ,  $z$ ,  $\phi$  and  $\theta$  coordinates to the CDF detector.

The particle density from collisions at hadron colliders has been found to be approximately constant in the full range of  $\phi$  and over a certain range of rapidity<sup>[35]</sup>, where rapidity is defined as:

$$y = \frac{1}{2} \ln \left( \frac{1 + \beta \cos \theta}{1 - \beta \cos \theta} \right)$$

The particles of interest to CDF have very small mass ( $\beta \approx 1$ ). In this limit the rapidity is commonly referred to as the pseudorapidity, which may be expressed compactly as:

$$\eta = -\ln \left( \tan \frac{\theta}{2} \right)$$

The CDF detector geometry was designed so that particle position could be described most easily in terms of the two coordinates  $(\phi, \eta)$ . The detector covers the pseudorapidity range  $|\eta| < 4.2$ . The figure on the next page illustrates the  $\eta$  segmentation of the CDF calorimeter towers (see also figure 2.5 in section 2.2).

Collectively, the event vertices measured by the Run 1 CDF detector have been observed to fit a Gaussian distribution with a mean value close to  $z = 0$  and a

standard deviation from the mean of  $\sigma = 30$  cm. Because of this significant deviation a distinction is made between detector coordinates and event coordinates. The detector coordinates of a particle are measured by using the center of the detector ( $z = 0$ ) as the origin while the particle's event coordinates are determined by taking the event vertex as the origin. For this analysis, detector coordinates will be implied unless event coordinates are explicitly specified by using a subscript (e.g.  $\eta_{\text{evt}}$ ).

# Appendix B

## CDF Kinematic Variables

The event polar angle (see Appendix A) enters in the definitions of some kinematical quantities that are frequently used in the analysis of CDF data. The "transverse momentum" of a particle is defined as:

$$P_T = P \sin \theta_{\text{evt}}$$

where  $P$  is the particle momentum measured in the Central Tracking Chamber (see section 2.2.1). Similarly, the "transverse energy" of a particle is defined as:

$$E_T = E \sin \theta_{\text{evt}}$$

where  $E$  is the particle energy measured in the calorimeter (see section 2.2.2).

Another important kinematic quantity that is defined in terms of the CDF calorimeter energy is the "missing transverse energy" of an event. It is given by:

$$\vec{\cancel{E}}_T = - \sum_i E_i \hat{n}_i$$

where  $E_i$  is the energy of the  $i_{th}$  calorimeter tower,  $\hat{n}_i$  is a unit vector perpendicular to the beam line that points to the  $i_{th}$  tower, and the sum is over all towers in the region  $|\eta| < 3.6$  with energy greater than a location-dependent threshold (100 MeV in the CEM, CHA and WHA; 300 MeV in the PEM; 500 MeV in the PHA and FEM; 800 MeV in the FHA). The restriction on pseudorapidity is necessary because some of the forward hadron calorimetry is distorted by final focusing quadrupole magnets employed by the Tevatron (the numbers listed here pertain to Run 1). Since the  $p\bar{p}$  collisions at CDF are presumed to be produced with approximately zero transverse energy,  $\vec{\cancel{E}}_T$  gives an estimate of the combined transverse energy of all post-collision particles that go undetected. For dilepton events  $\vec{\cancel{E}}_T$  is used as an estimate of the combined transverse energy of the neutrino and antineutrino stemming from  $W^\pm$

boson decay. Unfortunately, due both to initial state radiation contributions (see section 1.2.1) and to the intrinsic momenta of the  $p\bar{p}$  systems's constituent partons the  $p\bar{p}$  system does not always possess approximately zero transverse momentum. Therefore,  $\vec{\cancel{E}}_T$  is not a precise measurement of the neutrino kinematics. Moreover, since jets with  $|\eta| > 3.6$  do not contribute to  $\vec{\cancel{E}}_T$  its accuracy is greatly compromised for events with many jets.

In the search for dilepton events the missing transverse energy must be corrected for two reasons. First,  $\vec{\cancel{E}}_T$  is constructed using uncorrected jet energies. Therefore, It must be recalculated using jet energies that have been corrected for the effects described in section 3.2. Second, since minimum ionizing particles do not lose much of their energy in the calorimeters their  $E_T$  contribution to the construction of  $\vec{\cancel{E}}_T$  is underestimated. Therefore,  $\vec{\cancel{E}}_T$  must be corrected for muons. For a given muon this is accomplished by adding to  $\vec{\cancel{E}}_T$  the muon's calorimeter  $E_T$  and subtracting from  $\vec{\cancel{E}}_T$  the muon's true  $P_T$ , i.e. the  $P_T$  of the muon's CTC track (see sections 2.2.1 and 2.2.3).

# Appendix C

## Uncertainty on the Mean

This appendix gives a detailed explanation for the choice of uncertainties on the mean reconstructed masses used to construct the mapping function described in section 5.5.4.

One begins with a sample of  $N$  dilepton Monte Carlo events generated for a given input top quark mass,  $M_t^{MC}$ . For each event one measures a random variable defined as the mean value of the best combination likelihood distribution constructed for the given event. From these  $N$  measurements one builds a parent distribution as a function of top quark mass. Let  $M_N$  be the mean of the parent distribution and let  $\sigma_N$  be the R.M.S. of the distribution so that the error on  $M_N$  is  $\sigma_N/\sqrt{N}$  (assuming that the distribution is fairly Gaussian).

Then one chooses random samples of 7 events from the  $N$  events used to create the parent distribution. These samples need not be exclusive in that a given event can appear in several different samples. The mean value of each 7-event sample is determined by the joint likelihood method and added to a single histogram. It can be shown (for example, see reference [108]) that if the parent distribution is normally distributed then the histogram of mean values will also be normally distributed. Even if the parent distribution is not normally distributed the histogram will be more normally distributed than the parent distribution. The mean,  $M_{rec.}$ , of the histogram of mean values will be approximately equal to the mean,  $M_N$ , of the parent distribution. However, the R.M.S. of the histogram,  $\sigma_{rec.}$ , will be much smaller than that of the parent distribution,  $\sigma_N$ , and will be given approximately by:  $\sigma_{rec.} = \sigma_N/\sqrt{7}$ . Therefore, the mean obtained from the histogram of mean values is more accurate than the mean obtained from the parent distribution.

The error on  $M_{rec.}$  will be the same as the error on  $M_N$ . Hence, it will be given by  $\sigma_N/\sqrt{N}$ . But,  $\sigma_N$  can be obtained from the measured R.M.S. of the histogram of mean values. The R.M.S. of  $M_N$  is:  $\sigma_N = \sigma_{rec.} \times \sqrt{7}$ . Hence, the error on  $M_{rec.}$  is  $\sigma_t^{rec.}/\sqrt{N/7}$ . This is the value used in section 5.5.4.

# Bibliography

- [1] A spatial separation of  $\approx 18$  cm between interacting particles is implied in the comparison of all force strengths in this paragraph.
- [2] Particle Data Group, R.M. Barnett *et al.*, *Review of Particle Physics*, Physical Review D. **54**, 287 (1996).
- [3] The latest experimental results of neutrino mass measurement can be found at the Internet URL address:  
<http://www.hep.anl.gov/ndk/hypertext/nuindustry.html>.
- [4] Particle Data Group, R.M. Barnett *et al.*, *Review of Particle Physics*, Physical Review D. **54**, 303 (1996).
- [5] Particle Data Group, R.M. Barnett *et al.*, *Review of Particle Physics*, Physical Review D. **54**, 94 (1996).
- [6] Particle wave functions can be defined in terms of left-handed and right-handed components. Handedness is closely associated with a quantum number called helicity, which is defined as the component of a particle's spin in the direction of its motion. A particle is said to have positive (negative) helicity if its spin is parallel (antiparallel) to its direction of motion. In the limit of very high particle energies, it can be shown that right-(left-)handedness is equivalent to positive (negative) helicity.
- [7] F. Halzen and A.D. Martin *Quarks and Leptons: An Introductory Course in Modern Particle Physics*, John Wiley & Sons Inc., New York (1984).
- [8] L.B. Okun, *Leptons and Quarks*, North Holland Physics Publishing, New York (1984).
- [9] P.D.B. Collins, A.D. Martin and E.J. Squires, *Particle Physics and Cosmology*, John Wiley & Sons Inc., New York (1989).
- [10] B.R. Martin and G. Shaw, *Particle Physics*, John Wiley & Sons Inc., West Sussex, England (1992).
- [11] B. De Wit and J. Smith, *Field Theory In Particle Physics*, Elsevier Science Publishing Company Inc., New York (1986).
- [12] W. Bartel *et al.*, *A Measurement of the Electroweak Induced Charge Asymmetry in  $e^+e^- \rightarrow b\bar{b}$* , Phys. Lett. B **146**, 437 (1984).
- [13] F. Abe *et al.*, *Lower Limit on the Top Mass from Events with Two Leptons in  $p\bar{p}$  Collisions at  $\sqrt{s} = 1.8$  TeV*, Phys. Rev. Lett. **68**, 447 (1992).
- [14] F. Abe *et al.*, *Limit on the Top Quark Mass from Proton-Antiproton Collisions at  $\sqrt{s} = 1.8$  TeV*, Phys. Rev. Lett. **45**, 3921 (1992).
- [15] S. Abachi *et al.*, *Search for the Top Quark in  $p\bar{p}$  Collisions at  $\sqrt{s} = 1.8$  TeV*, Phys. Rev. Lett. **72**, 2138 (1994).
- [16] F. Abe *et al.*, *Evidence for Top Quark Production in  $p\bar{p}$  Collisions at  $\sqrt{s} = 1.8$  TeV*, Phys. Rev. D **50**, 2966 (1994).

- [17] F. Abe *et al.*, *Kinematic Evidence for Top Quark Pair Production*, Phys. Rev. D. **51**, 4623 (1994).
- [18] S. Abachi *et al.*, *Search for High Mass Top Quark Production in  $p\bar{p}$  Collisions at  $\sqrt{s} = 1.8$  TeV*, Phys. Rev. Lett. **74**, 2422 (1995).
- [19] F. Abe *et al.*, *Observation of Top Quark Production in  $p\bar{p}$  Collisions with the Collider Detector at Fermilab*, Phys. Rev. Lett. **74**, 2626, (1995).
- [20] S. Abachi *et al.*, *Observation of the Top Quark*, Phys. Rev. Lett. **74**, 2632 (1995).
- [21] F. Abe *et al.*, *Measurement of the Top Quark Mass*, Phys. Rev. Lett. **80**, 2767 (1997).
- [22] F. Abe *et al.*, *Measurement of the Top Quark Mass and  $t\bar{t}$  Production Cross Section from Dilepton Events at the Collider Detector at Fermilab*, Phys. Rev. Lett. **80**, 2779 (1997).
- [23] F. Abe *et al.*, *Measurement of the Top Quark Mass with the Collider Detector at Fermilab*, Fermilab Report No. Fermilab-Pub-98/ 319-E (1999).
- [24] F. Abe *et al.*, *First Observation of the All-Hadronic Decay of  $t\bar{t}$  Pairs*, Phys. Rev. Lett. **79**, 1992 (1997).
- [25] F. Abe *et al.*, *Measurement of the  $t\bar{t}$  Production Cross Section in  $p\bar{p}$  Collisions at  $\sqrt{s} = 1.8$  TeV*, Phys. Rev. Lett. **80**, 2773 (1998).
- [26] S. Abachi *et al.*, *Direct Measurement of the Top Quark Mass*, Phys. Rev. Lett. **79**, 1197 (1997).
- [27] S. Abachi *et al.*, *Measurement of the Top Quark Pair Production Cross Section in  $p\bar{p}$  Collisions*, Phys. Rev. Lett. **79**, 1203 (1997).
- [28] B. Abbott *et al.*, *Measurement of the Top Quark Mass using Dilepton Events*, Phys. Rev. Lett. **80**, 2063 (1998).
- [29] B. Abbott *et al.*, *Direct Measurement of the Top Quark Mass at D0*, Fermilab Report No. Fermilab-Pub-98/031-E (1998).
- [30] B. Abbott *et al.*, *Measurement of the Top Quark Mass in the Dilepton Channel*, Fermilab Report No. Fermilab-Pub-98/261-E (1998).
- [31] B. Abbott *et al.*, *Measurement of the Top Pair Production Cross Section in  $p\bar{p}$  Collisions using Multijet Final States*, Fermilab Report No. Fermilab-Pub-98/130-E (1998).
- [32] Internet URL address: <http://www-cdf.fnal.gov/upgrades/upgrades.html>
- [33] Internet URL address: <http://www-fermi3.fnal.gov>.
- [34] F. Abe *et al.*, *The CDF detector: An Overview*, Nucl. Instrum. Methods **A271**, 387 (1988).
- [35] D.H. Perkins, *Introduction to High Energy Physics*, Addison-Wesley Publishing Co. Inc., Reading, MA (1987).
- [36] R.C. Fernow, *Introduction to Experimental Particle Physics*, Cambridge University Press, Cambridge, England (1986).

- [37] D. Amidei *et al.*, *The Silicon Vertex Detector of the Collider Detector at Fermilab*, Nucl. Instrum. Methods **A350**, 73 (1994).
- [38] P. Azzi *et al.*, *SVX', The New CDF Silicon Vertex Detector*, Nucl. Instrum. Methods **A360**, 137 (1995).
- [39] M. Binkley *et al.*, *The CDF Vertex Time Projection Chamber System*, Nucl. Instrum. Methods **A268**, 75 (1988).
- [40] F. Bedeschi *et al.*, *Design and Construction of the CDF Central Tracking Chamber*, Nucl. Instrum. Methods **A268**, 50 (1988).
- [41] L. Balka *et al.*, *The CDF Central Electromagnetic Calorimeter*, Nucl. Instrum. Methods **A267**, 272 (1988).
- [42] S. Bertolucci *et al.*, *The CDF Central and Endwall Hadron Calorimeter*, Nucl. Instrum. Methods **A267**, 301 (1988).
- [43] Y. Fukui *et al.*, *CDF End Plug Electromagnetic Calorimeter Using Conductive Plastic Proportional Tubes*, Nucl. Instrum. Methods **A267**, 280 (1988).
- [44] S. Cihangir *et al.*, *The CDF Forward/Backward Hadron Calorimeter*, Nucl. Instrum. Methods **A267**, 249 (1988).
- [45] G. Ascoli *et al.*, *CDF Central Muon Detector*, Nucl. Instrum. Methods **A268**, 33 (1988).
- [46] M. Kruse, Ph.D. thesis: *Observation of Top Quark Pair Production in the Dilepton Decay Channel from Proton-Antiproton Collisions at  $\sqrt{s} = 1.8$  TeV*, Purdue University (1996); cdf note 4632.
- [47] D. Amidei *et al.*, *A Two Level Fastbus Based Trigger System for CDF*, Nucl. Instrum. Methods **A269**, 51 (1988).
- [48] E. Barsotti *et al.*, *Fastbus Data Acquisition for CDF*, Nucl. Instrum. Methods **A269**, 82 (1988).
- [49] G.W. Foster *et al.*, *A Fast Hardware Track Finder for the Central Tracking Chamber*, Nucl. Instrum. Methods **A269**, 93 (1988).
- [50] G. Ascoli *et al.*, *CDF Central Muon Level-1 Trigger Electronics*, Nucl. Instrum. Methods **A269**, 63 (1988).
- [51] F. Abe *et al.*, *Topology of Three-Jet Events in  $p\bar{p}$  Collisions at  $\sqrt{s} = 1.8$  TeV*, Phys. Rev. D **45**, 1448 (1992).
- [52] F. Abe *et al.*, *Jet Fragmentation Properties in  $p\bar{p}$  Collisions at  $\sqrt{s} = 1.8$  teV*, Phys. Rev. Lett. **65**, 968 (1990).
- [53] F. Abe *et al.*, *Study of Four-Jet Events and Evidence for Double Parton Interactions in  $p\bar{p}$  Collisions at  $\sqrt{s} = 1.8$  TeV*, Phys. Rev. D **47**, 4857 (1993).
- [54] F. Abe *et al.*, *Comparison of Jet Production in  $p\bar{p}$  Collisions at  $\sqrt{s} = 546$  and 1800 GeV*, Phys. Rev. Lett. **70**, 1376 (1993).
- [55] L. Keeble and B. Flaugh, *New Jet Correction Function QDJSCO 2.0*, CDF note 1513 (1991).



- [56] A. Caner *et al.*, *Jet Corrections for Top Mass Fitting*, CDF note 2469 (1994).
- [57] F.E. Paige and S.D. Protopopescu, ISAJET Monte Carlo Generator, BNL Technical Report No. 38774 (1986).
- [58] G. Marchesini and B.R. Webber, HERWIG Monte Carlo Version 5.6: *Monte Carlo Simulation of General Hard Processes without Coherent QCD Radiation*, Nucl. Phys. B **310**, 461 (1988).
- [59] S. Aota *et al.*, *B-Jet Energy Correction for Top Mass Determination (II) - as a function of Top Mass -*, CDF note 3189 (1995).
- [60] M. Shapiro *et al.*, *A User's Guide to QFL*, CDF note 1810 (1992).
- [61] A. Caner *et al.*, *CDFSIM and QFL Simulation of the CDF Detector*, CDF note 2177 (1993).
- [62] G.T. Watts, Ph.D. thesis: *Evidence for Top Quark Production in  $p\bar{p}$  collisions at  $s = 1.8$  TeV*, University of Rochester (1994).
- [63] D. Buskulic *et al.*, *A Precise Measurement of  $\sigma_{Z \rightarrow b\bar{b}}/\sigma_{Z \rightarrow \text{hadrons}}$* , Phys. Lett. B **313**, 535 (1993).
- [64] S. Dell-Agnello, Ph.D. thesis: *Search for the Top Quark Using Secondary Vertexing Tags in  $W + \text{jets}$  Events in  $p\bar{p}$  Collisions at  $\sqrt{s} = 1.8$  TeV*, University of Pisa, (1994).
- [65] W. Yao *et al.*, *A Seed Vertexing b-Tag Algorithm for Top*, CDF note 2716 (1994).
- [66] W. Yao *et al.*, *Top Search in Lepton+Jets With SECVTX*, CDF note 2989 (1995).
- [67] C. Campagnari *et al.*, *Low  $P_T$  Electron Identification*, CDF note 2161 (1993).
- [68] C. Campagnari *et al.*, *Muon Identification in the Lepton+Jets+Muon Tag Analysis*, CDF note 2098 (1993).
- [69] M. Hohlmann, Ph.D. thesis: *Observation of Top Quark Pairs in the Dilepton Decay Channel using Electrons, Muons and Taus*, University of Chicago (1997); cdf note 4280.
- [70] M. Kruse *et al.*, *Top Acceptance in the Dilepton Channel for Run 1*, CDF note 3300 (1996).
- [71] These numbers were supplied by Mark Kruse and are similar to the numbers obtained from the HERWIG Monte Carlo events that were used to construct the mass dependence plots of CDF note 3300.
- [72] PYTHIA Monte Carlo Version 5.7, H.-U. Bengtsson and T. Sjöstrand, Computer Physics Commun.**46**, 43 (1987).
- [73] M. Kruse and J. Konigsberg, *Top Dilepton Analysis - Update to  $110 \text{ pb}^{-1}$* , CDF note 3482 (1997).
- [74] F.A. Berends *et al.*, VECBOS Monte Carlo generator: *On the Production of a  $W$  and Jets at Hadron Colliders*, Nucl. Phys. B **357**, 32 (1991).
- [75] J. Benlloch *et al.*, *On Transforming Partons into Jets: HERPRT, a New Interface Between ME MC and Fragmentation Models*, CDF note 1823 (1992).

- [76] L. Song *et al.*, *Study of Top Dilepton Background from  $b\bar{b}$  Sources*, CDF note 2106 (1993).
- [77] P. Avery *et al.*, *QQ: A Monte Carlo Generator*, CLEO software note CSN-212 (1985).
- [78] J. Lewis and P. Avery, *CLEOMC: The CDF Interface to the CLEO Monte Carlo (QQ)*, CDF note 2724 (1994).
- [79] M. Kruse, *Misreconstructed Z's as a Background in the Top Dilepton Channel*, CDF note 4148 (1997).
- [80] R.H. Dalitz and G. Goldstein, *Decay and Polarization Properties of the Top Quark*, Phys. Rev. D **45**, 1531 (1992).
- [81] R.H. Dalitz, G. Goldstein and K. Sliwa, *On Observing Top Quark Production at the Tevatron*, CDF note 1750 (1992).
- [82] R.H. Dalitz, G. Goldstein and K. Sliwa, *Search for  $t\bar{t}$  Events in the "Semileptonic" Mode*, CDF note 1751 (1992).
- [83] K. Sliwa, *Search for  $t\bar{t}$  Events in the Lepton and Four Jets Final State*, CDF note 1993 (1993).
- [84] R.H. Dalitz, G. Goldstein and K. Sliwa, *Observing Top Quark Production at the Fermilab Tevatron*, Phys. Rev. D **47**, 967 (1993).
- [85] K. Sliwa, *A Non-Black-Box Approach to Kinematical Fitting and Its Application to a Top Quark Search*, CDF note 3057, (1995).
- [86] R. Barnett and L. Hall, *Squarks in Tevatron Dilepton Events*, hep-ph/9609313.
- [87] J. Antos, K. Karr, K. Sliwa and M. Timko, *Kinematical Analysis of  $t\bar{t}$  Candidates in Di-lepton Events*, CDF note 3104 (1995).
- [88] K. Karr and K. Sliwa, *A Study of the Efficiency for Assigning Leading Transverse Energy Jets to the  $b$  and  $\bar{b}$  Quarks Used in the Mass Fitting of Dilepton  $t\bar{t}$  Events*, CDF note 3525 (1996).
- [89] W. Yao, L. Galtieri and J. Lys, *Improved Measurement of Top Quark Mass in the Dilepton Channel using a Neutrino Weighting Method*, CDF note 4394 (1998).
- [90] S. Aota *et al.*, *Measurement of the Top Quark Mass in the Lepton+Jets Channel*, CDF note 4199 (1997).
- [91] A.D. Martin, R.G. Roberts and W.J. Stirling, *Parton Distributions of the Proton*, Phys. Rev. D **50**, 6734 (1994).
- [92] A.D. Martin, R.G. Roberts and W.J. Stirling, *Pinning Down the Gluon in the Proton*, Phys. Lett. B **354**, 155 (1995).
- [93] A.D. Martin, R.G. Roberts, M.G. Ryskin and W.J. Stirling, *Consistent Treatment of the Charm Evolution in Deep Inelastic Scattering*, Eur. Phys. Jour. C **2**, 287 (1998).
- [94] H. Lai *et al.*, *Global QCD Analysis and the CTEQ Parton Distributions*, Phys. Rev. D **51**, 4763 (1995).

- [95] J. Botts *et al.*, *CTEQ Parton Distributions and Flavor Dependence of Sea Quarks*, Phys. Lett. B **304**, 159 (1993).
- [96] D. Duke and J. Owens,  *$Q^2$ -Dependent Parameterizations of Parton Distribution Functions*, Phys. Rev D **30**, 49 (1984).
- [97] A. Devoto *et al.*, *Direct Analysis of Scaling Violations in Large- $Q^2$  Deep-Inelastic Neutrino and Muon Scattering*, Phys. Rev. D **27**, 508 (1983).
- [98] B. Harral, *Kinematic Fit Method for Top Candidates*, CDF note 2200 (1993).
- [99] B. Harral, S. Kim, M. Shaw and S. Vejcik, *An Analysis-Control-Driven Mass Fitter for Top Decays*, CDF note 2904 (1994).
- [100] M. Contreras, J. Konigsberg, C. Grosso-Pilcher and G. Sullivan, *A Measurement of the Top Mass in Dilepton Events Using Kinematical Distributions*, CDF note 3298 (1997).
- [101] M. Contreras, J. Konigsberg, C. Grosso-Pilcher and G. Sullivan, *Updated Top Mass from Jet Energies in Dilepton Events*, CDF note 4022 (1997).
- [102] J. Antos, G.P. Yeh and P. Yeh, *Measurement of the Top Quark Mass in Dilepton Channel Using Invariant Mass of Lepton and  $b$  jet*, CDF note 3700 (1996).
- [103] J. Antos, G.P. Yeh and P. Yeh, *An Update of  $\langle M_{bb}^2 \rangle$  Analysis for Top Quark Mass in Dilepton Channel*, CDF note 4145 (1997).
- [104] The D0 Collaboration, *Measurement of the Top Quark Mass Using Dilepton Events*, FERMILAB\_PUB-97/172-E.
- [105] E.W. Varnes, Ph.D. thesis: *Measurement of the Top Quark Mass*, University of California at Berkeley, (1997). Internet URL address: [http://www-d0.fnal.gov/publications\\_talks/thesis/thesis.html](http://www-d0.fnal.gov/publications_talks/thesis/thesis.html).
- [106] G.V. Velez, *A Determination of the Top Mass from the Dilepton Events Using the Modified Lepton+Jets MINUIT Fitter*, CDF note 4607 (1998).
- [107] K. Karr and K. Sliwa, *Kinematical Analysis of the  $t\bar{t}$  Candidate Events in the Di-lepton Channel*, CDF note 4393 (1998).
- [108] B.C. Erricker, *Advanced General Statistics*, The English Universities Press Ltd., London (1971).